



Pilot sites data and integration analysis D4.1

HOCLOOP

Due date of deliverable: 31/03/2023
Actual submission date: 30/03/2023
Resubmission after revision of conformance with GA article 17: 23/06/2023
Start date of project: 01/10/2022
Dissemination level: Public

Research for a better future



Funded by the European Union. Views and opinions expressed are however those of the author(s) only and do not necessarily reflect those of the European Union or CINEA. Neither the European Union nor the granting authority can be held responsible for them.

Prepared by	Reviewed Internally by	Reviewed Externally by	Approved by
Mrityunjay Singh Christine Souque Domenico Liota Daniele Fiasci Ben Laenen Virginie Harcouët-Menou	Ben Laenen Virginie Harcouët-Menou Mario Silva	Jouni Juntunen	Mario Silva

Technical References

Project Acronym	HOCLOOP
Project Title	A circular by design environmentally friendly geothermal energy solution based on a horizontal closed loop - HOCLOOP
Project Coordinator	IFE
Project Duration	42 months

Deliverable No.	D4.1
Dissemination level 1	PU
Work Package	WP4
Task	4.1
Lead beneficiary	"VITO"
Contributing beneficiary(ies)	IFPEN, TUDA, UNIBA, UNIFI
Prepared by /Author(s)	Ben Laenen (VITO), Virginie Harcouët-Menou (VITO), Mrityunjay Singh (TUDA), Christine Souque (IFPEN), Domenico Liota (UNIBA), Daniele Fiasci (UNIFI)
Reviewed by	Jouni Juntunen (VAASA)
Approved by/Coordinator	Mario Silva (IFE)
Due date of deliverable	31/03/2023
Actual submission date	30/03/2023

¹PU = Public

PP = Restricted to other programme participants (including the Commission Services)

RE = Restricted to a group specified by the consortium (including the Commission Services)

CO = Confidential, only for members of the consortium (including the Commission Services)

Document history

V	Date	Author(s) /Reviewer(s) (Beneficiary)	Description
0.1	07/03/2023	Ben Laenen (VITO), Virginie Harcouët-Menou (VITO), Mrityunjay Singh (TUDA), Christine Souque (IFPEN), Domenico Liota (UNIBA), Daniele Fiasci (UNIFI)	First Draft
0.2	17/03/2023	Virginie Harcouët-Menou (VITO), Ben Laenen (VITO)	First internal revision
0.3	23/03/2023	Mario Silva (IFE)	Second Internal



			Pilot sites data and integration analysis
0.4	23/03/2023	Mario Silva (IFE)	Second draft Distributed
0.5	27/03/2023	Jouni Juntunen (VAASA)	Reviewer Comments
1.0	29/03/2023	Mario Silva (IFE)	Comments Addressed, Final version
2.0	30/03/2023	Mario Silva (IFE)	Document uploaded
2.1	23/06/2023	Mario Silva (IFE)	Revision of conformance with GA article 17. Final version.

Disclaimer

This document is partly based on the EC's official documents and profound knowledge of guidelines and ways of working in Horizon Europe. While guidelines on administration and reporting are as much as possible the same as the official documents, adjustments have been made with logical build-up and readability in mind. However, no legal responsibility can be taken for the contents in this document. If in doubt with an issue, please consult the official documents, or ask IFE, who will ask for an official EC response if necessary.

List of Abbreviations

COP: Coefficient of Performance
DHS: Dual Heat String
DOI: Digital Object Identifiers
EC: European Commission
ORC: Organic Rankine Cycle
URS: User Requirement Specifications
UTS: Underground Thermal Storage

Table of Contents

1. Introduction	7
2. Objectives	7
3. Methodology	7
4. Results.....	8
4.1 Description of the HOCLOOP solution	8
4.2 Case study: Balmatt, Mol (Belgium)	9
General description of the pilot site:	9
Geological conditions	10
Past/Current/future above ground energy system	35
Description and Schematic overview on different integration options of the HOCLOOP	37
Technical challenges	40
Economic aspects	41

Summary table.....	41
4.3 Case study Darmstadt, Germany	43
General description of the pilot site	43
Geological conditions	43
Past/Current/future above ground energy system	52
Description and Schematic overview on different integration options of the HOCLOOP concept	53
Technical challenges	54
Economic aspects.....	54
Summary table.....	55
4.4 Case study Parisian basin, France (IFPEN).....	55
General description of the pilot site	55
Geological conditions	56
Past/Current/future above ground energy system	64
Description and Schematic overview on different integration options of the HOCLOOP concept	66
Economic aspects.....	66
Summary table.....	67
4.5 Case study Italy	68
Geological conditions.....	69
Past/Current/future above ground energy system	81
Summary table.....	86
5. Conclusions	87
5.1 Challenges.....	87
5.2 Recommendations	88
6. References	88
Annex 1: Case study: Template	94
General description of the pilot site	94
Geological conditions	94
Past/Current/future above ground energy system	94
Description and Schematic overview on different integration options of the HOCLOOP concept	95
Technical challenges	95
Economic aspects.....	95
Summary table.....	95

Executive Summary Deliverable

Scope of the deliverable

The objective of deliverable 4.1 is to facilitate the future integration of the HOCLOOP innovation at the pilot sites. The pilot sites have been selected to cover a wide range in underground and surface conditions. They also cover a wide range of development stages: from green field exploration to functional geothermal plants. Consequently, the degree of uncertainty in the data varies from one site to another.

Based on the specific geological settings and surface energy systems of the pilot sites, a schematic overview is made on different integration options of the HOCLOOP concept. Deliverable 4.1 is the first step towards the final detailed design and the integration of the HOCLOOP technology at the pilot sites.

Deliverable 4.1 captures the technology user's requirement specifications for each of the pilot sites. These specifications will be used to develop the functional design specification, to capture designs, concepts, and process flow information as inputs for the other tasks. This process will lead to the determination of the types of data required to assess the applicability of the HOCLOOP concept, concerning aspects such as underground characteristics, current and planned local energy system, expected electricity and thermal energy flows.

Main conclusions

Challenges

Limited data availability, either of the subsurface properties or of the surface demand, is one of the challenges faced while collecting information on the different pilot sites. In addition, the degree of uncertainty in the data varies largely from one site to another.

The Balmatt site has the largest dataset as result of three deep boreholes that have been drilled at this location and the knowledge that has been acquired over the last years of its development. For this site, all necessary data about the underground is available for simulation of thermal power and temperatures.

At the Darmstadt site, wells have been drilled recently and further characterization of the reservoir is ongoing. Therefore, some data is not yet available, for example the thermal properties will be determined by the enhanced thermal response test that will be performed in the coming months. The geological model at this location will also be finalized in the coming months and the groundwater model will be updated. Petrophysical parameters for units without sufficient sample coverage (Permian basalts) will be measured.

In the Paris basin case, thermal conductivity of the rock is the data useful for the closed-loop technology assessment accompanied by the biggest deal of uncertainty. Such data was never directly determined. The values proposed in this report result from modelling exercises. In the absence of data, no calibration on existing data was performed.

Furthermore, for the two pilot sites where geothermal plants are in place (Balmatt case in Belgium) or under the last phase of development (Darmstadt case in Germany), a description of the plant, peripherals and district heating grid as it is currently or as it will be constructed is available. This is not the case for the Italian case, which does not consider an actual geothermal plant but different potential integration options. At Balmatt, the main future challenges are the optimal integration of the HOCLOOP technology with the existing geothermal loop, the control of both sources for combined heat and power delivery, and the impact of the HOCLOOP solution on the stress conditions within the targeted limestones.

Recommendations

For the modelling exercise that will be performed in T4.2, if site data is not available, literature data presented in this deliverable can be used. This deliverable highlights the site-specific data that is still missing at the start of the project and that should be acquired to enable the realistic design of the HOCLOOP concept. The summary table that is presented for the different sites should be updated during the course of the project when additional data becomes available.

Limitations

The data presented in this deliverable is based on current knowledge and available data. At some sites, reservoir properties are still uncertain, and some literature data or data derived from models are proposed. The integration options that are proposed for the different pilot sites should be considered as preliminary ideas, that can evolve during the project, based on the results of T4.2 for example where the performance of the HOCLOOP system at the different sites will be assessed. For the Italian and French cases, the description of the integration options consists of a theoretical exercise inspired from existing geothermal developments in the targeted regions.

1. Introduction

The objective of this deliverable is to facilitate the future integration of the HOCLOOP innovation at the pilot sites. In a first chapter, general information is given about the HOCLOOP concept (description of innovation, the status of development, surface integration options). Afterwards, for each of the pilot site, the local geology, and the current or future above ground energy system are described as well as the technical issues to be studied to ensure the safe implementation of the concept. The collected information will enable to gain knowledge about the businesses' attitudes and procedures at the different locations.

The pilot sites have been selected to cover a wide range of underground, surface conditions, and development stages (from green field exploration to fully functional geothermal plants including district heating). Consequently, the degree of uncertainty in the data varies from one site to another. For the two pilot sites, where geothermal plants are in place (Balmatt case in Belgium) or under the last phase of development (Darmstadt case in Germany), a description of the plant, peripherals and district heating grid as it is currently or as it will be constructed is summarized. For the Italian and French cases, which do not consider actual geothermal plants, the description consists of a theoretical exercise inspired from existing geothermal developments in the targeted regions.

Based on the specific geological setting and surface energy system of the case studies, a first schematic overview is made on different integration options of the HOCLOOP concept in the current or future energy system. For each potential pilot site, the user requirement specifications (URS) have been captured throughout the document and the main points are grouped in the conclusions. The URS will be used to develop the functional design specification, to capture designs, concepts, and process flow information as inputs for the other tasks. This will lead to the determination of the types of data required, concerning aspects such as underground characteristics, current and planned local energy system, expected electricity and thermal energy flows.

2. Objectives

The deliverable contributes towards the following work package objective:

O 4.1 Gathering and processing of data about the underground characteristics and above ground energy system at the different selected pilot sites.

The document contributes to this objective as it acts as a step towards the final detailed design and the integration of the HOCLOOP technology at the pilot sites.

3. Methodology

As a first step, a template to collect the URS was defined. The template is added in Annex 1. Next, dedicated workshops have been organized for each pilot site with the full consortium, to collect pilot sites data and information related to the local geology, as well as current/future above ground energy system. Possible integration options of the HOCLOOP concept in the different energy systems have been discussed and the most relevant ones are summarized in this deliverable.

Based on the data collected, the URS has been prepared for each pilot site. It will be used to develop the functional design specification, to capture designs, concepts, and process flow information as inputs for the next tasks (T4.2, T4.3, T4.4, T4.5) and for work packages (WP3, WP5, WP6). The type of data

required, concerning aspects such as underground characteristics, current and planned local energy system, expected electricity and thermal energy flows to enable the optimal integration of the HOCLOOP at the different pilot sites are then summarized in synthetic tables for each pilot.

4. Results

4.1 Description of the HOCLOOP solution

Figure 1, presents a schematic of the HOCLOOP solution. The solution is based on establishing a vertical well down to a suitable depth below the surface of the earth, where the temperature and the heat conductivity of the formation are suitable for proper heat exchange between the formation and the fluid in the well. To maximize the heat exchange, a long horizontal length of the well is established. The well is completed with a Dual Heat String (DHS), i.e., a double wall vacuum insulated string, to the target depth of the well. The geothermal heat is extracted by direct heat conduction between the formation rock and the fluid in the well. The circulation fluid is heated from the formation as it is pumped down the annulus between the DHS to the bottom of the well. The circulation fluid is heated due to the heat conductivity of the formation on its way to the bottom of the well. The circulation fluid is returned to the earth surface through the centre channel of the DHS. The heat loss of the fluid returning to the surface is held at a minimum level due to the vacuum insulation of the DHS. The thermal energy from the hot fluid from the well can be used both for district heating as well as for electricity production at the surface. The fluid is then pumped back into the well for renewed heating in a closed loop, as indicated in the figure.

For optimum performance the original temperature as well as the heat conductivity of the formation rock should be possibly high. The original formation temperature is here assumed to be in the order of 150°C, but can be lower or higher, depending on the surface application. A high-performance DHS design will be based on the case studies presented below. For the applications considered here, the total well depth is assumed to be up to 8 km. The prototype DHS is currently in development, the preliminary design data for the well and the DHS are as follows:

- Vertical well section inner diameter: 220 mm or larger, depend on the well design
- Horizontal well section inner diameter: 175 mm or larger, depend on the well design
- DHS outer diameter: 140 mm, or larger, depend on the well design
- DHS inner diameter: 85 mm, or smaller, depend on the well design
- DHS insulation performance: 0.01 W/(m K), or larger, depend on the design

At the earth surface, the HOCLOOP solution is foreseen to be integrated in a district heating, or similar energy supply plant. In this case, the surface arrangement would include a heat exchanger to the plant. If the temperature for the return fluid is regulated to be above 90 degrees, an Organic Rankine Cycle (ORC) can be connected for the generation of additional electricity from the energy supply plant.

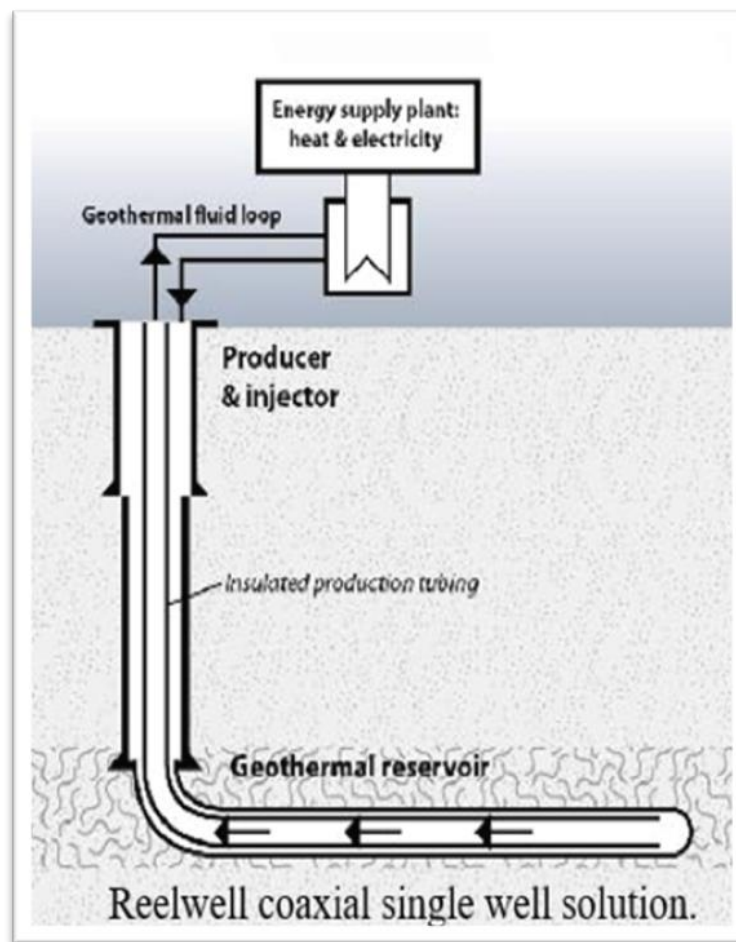


Figure 1: Schematic of the HOCLOOP solution for horizontal closed loop geothermal energy extraction.

4.2 Case study: Balmatt, Mol (Belgium)

General description of the pilot site:

In November 2019, VITO started a geothermal exploration and development project in the northern part of Belgium (province of Antwerp). The project resulted in the construction of the Balmatt geothermal plant in Mol. The plant targets a fractured limestone reservoir of Lower Carboniferous age at a depth of 3200 to 3400 m. It is the first deep geothermal plant in the Campine area. The plant was in operation from April 2021 until 16th of November 2022, though production was not continuous and at lower flow rates than anticipated. This happened because of issues with induced seismicity. Understanding the impact of the geothermal operations on the stress state of the limestones and the seismic risk is currently the main research topic at the Balmatt geothermal site.

The well field consists of three deep geothermal wells: one vertical production well (depth 3610 m) and two deviated wells (well 2 with a depth 4341 m and well 3 with a depth of 4905 m). Well 2 is equipped and used as an injection well and well 3 currently as a monitoring well in the context of research on induced seismicity. The geothermal installations at Balmatt consist in a loop to extract heat from the geothermal fluid, a connection to a nearby district heating network, an ORC and adiabatic coolers. A diagram of the installations is given in Figure 11.

The district heating network is delivering heat to the offices and research buildings of VITO and the nuclear research institute SCK-CEN, and to a nearby residential area. The priority use of the geothermal energy is for heating. The ORC allows for electricity production during periods with lower heat demand in the district heating network. Within the project, VITO wants to further investigate using the third well (currently used for monitoring) for the HOCLOOP solution. All necessary data of the underground is available for simulation of the thermal power and temperatures. The main challenges are the optimal integration of the HOCLOOP technology with the existing geothermal loop, the control of both sources for combined heat and power delivery, and the impact of the HOCLOOP solution on the stress conditions within the targeted limestones.

Geological conditions

Used data

Wells

Table 1 gives an overview of the wells that were used in the evaluation. The three wells were drilled in the context of the Balmatt geothermal project.

Table 1: Wells used to for the Balmatt case study. Coordinates are in Lambert 1972, depth in meters below surface.

Id	Well	X (m)	Y (m)	Z m (TAW)	Total depth (m)
MOL-GT-1	MOL-GT-01-(S1)	201783	212961	25.0	3610
MOL-GT-2	MOL-GT-02	201791	212962	25.0	3715.15
MOL-GT-3	MOL-GT-03(-S1)	201768	212960	25.0	4234.61

Seismic data

The following seismic data covers the Balmatt geothermal site:

- 2010 2D Herentals-Mol-Dessel: regional 2D seismic survey covering the Balmatt site and connecting the site with an offset wells in Poederlee and with existing seismic surveys towards the west-northwest. The survey was used to build the geological model of the Balmatt geothermal site.
- DGE-ROLLOUT: 2D seismic survey over MOL-GT-01, extending the geological model of the Balmatt geothermal site towards the east.

Models and datasets

The following geological models and datasets were consulted:

- The 3D Geological Model of Flanders ([Geologisch 3D-model G3Dv3 | DOV \(vlaanderen.be\)](#))
- ‘*Compilatie en Duiding van Warmtedata in de Diepe Ondergrond van Vlaanderen en Opmaak van een Warmtefluxkaart*’: A compilation of temperature data of the Flemish subsurface commissioned by the Flemish Planning Office for the Environment (VPO) (Broothaers et al., 2020)
- [DOV Verkenner \(vlaanderen.be\)](#): Lithological data and data from cores/cutting available through the database of the Flemish Subsurface
- In-house dynamic model of the Balmatt geothermal site (VITO).

Geological setting

Regional geology

The Balmatt geothermal site in Mol is located within the Campine Basin. The Belgian Campine Basin covers a part of the provinces of Antwerpen and Limburg (Langenaeker 2000; Laenen et al. 2004). It is part of the north-western European Carboniferous basin (NWEBCB). To the West and South, the basin is bounded by the early Palaeozoic subcrop of the Caledonian London-Brabant Massif (Langenaeker 2000). The northern border of the basin is formed by the Krefeld high and IJmuiden ridge. Eastward the basin extends into Dutch Limburg, where the NE-SW striking Variscan Anticlinal fault/Oranje fault system forms the boundary with the German Carboniferous Wurm Basin (Figure 2).

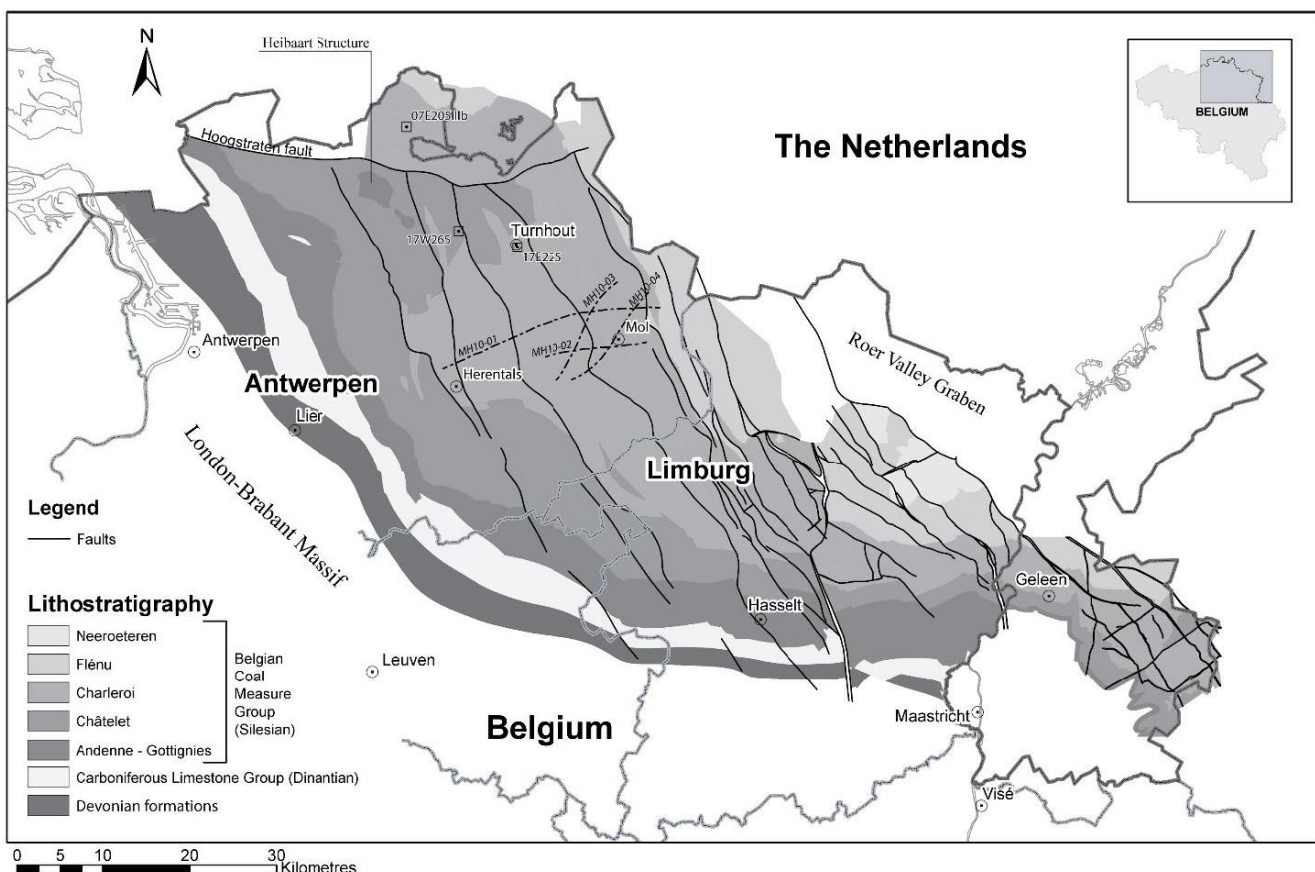


Figure 2: Pre-Permian subcrop map of the Campine Basin in northern Belgium (compiled after Langenaeker 2000, and Patijn and Kimpe 1961)

Devonian sediments are present above an angular unconformity at the top of the Caledonian basement. The Devonian strata are covered by Lower Carboniferous dolostones and limestones. In the western part of the basin, the carbonates are karstified. The transition from the Lower to the Upper Carboniferous is marked by a shift from a carbonate to a siliciclastic depositional setting that is characteristic for the Upper Carboniferous paralic coal basin of northwestern Europe. In the north-eastern part of the Campine Basin, the Westphalian rocks are disconformably covered by sediments of late Palaeozoic

and early Mesozoic age (Permian, Triassic, and Jurassic strata). The Palaeozoic and Mesozoic successions are disconformably covered by a 300 to 1000 m thick sequence Upper Cretaceous chalk and predominantly clastic Cenozoic deposits.

The area is transected by a predominant set of (N)NW - (S)SE striking normal faults, which locally display a shear component. Most of these faults already existed during the Early Carboniferous. Most faults were reactivated during the Jurassic, and some are still active today. A tectonic inversion of these reactivated faults during the Late Cretaceous and Early Cenozoic was followed by the subsidence of the Roer Valley Graben in the late Oligocene (Langenaeker, 2000). The resulting pattern is one of a series of elongated, NW-SE striking fault blocks that are generally tilted towards the north/ northeast.

A full description of the depositional history of the Campine Basin is given in Langenaeker (2000) and Kombrink (2008). A recent discussion on the structural setting of the basin is given in Broothaers et al. (2019) and Broothaers et al. (2021).

Local geology

Data and observations from wells MOL-GT-01, MOL-GT-02 and MOL-GT-03 and two seismic surveys are available for an overview of the local geology. A map of the top of the Lower Carboniferous Limestone Group is shown in Figure 3. A geological cross section is shown in Figure 4. The geological summary of the wells is included in the appendix (A).

Table 2 summarizes the lithostratigraphy of well MOL-GT-03. Well MOL-GT-03 has the most extensive section of the 3 wells as it was drilled through the entire carbonate sequence and entered the underlying Devonian sandstones. The true stratigraphic thickness of the Lower Carboniferous is 795 m. The formation tops were picked based on the wireline Gamma Ray (GR). During drilling real-time LWD-GR was used for correlation in all sections.

The stratigraphic scheme utilized in this report follows the Lithostratigraphic scale of Belgium, Geologica Belgica, Vol. 4 (2001), Nr. 1-2 with additional references from the National Stratigraphic Commission Belgium ([Home | National Commission for Stratigraphy Belgium \(naturalsciences.be\)](#)). In addition, the 2 papers on Belgian pre-Tertiary stratigraphy by B. Laenen (2002 & 2003) were used as reference.

A brief description of the different lithostratigraphic units is given in the sections below.

Table 2: Lithostratigraphy of well MOL-GT-03 (depths are for Formation tops)

Age	Lithostratigraphy MOL-GT-03(-S1) Group / Formation / Member (DOV Code)	Actual		Thickness mTVD
		mBGL	m/TAW	
Cenozoic	Mol Fm (MI)	0	+25	25
		25	0	10
		35	-10	100
		135	-110	17
		152	-127	29
	Kasterlee Fm (KI)	181	-156	10
		191	-166	22
	Rupel Gp	Boeretang Mb	213.0	18.5
		Putte Mb	231.5	52.0
		Terhagen Mb	283.5	19.5
		Belsele-Waas Mb	303.0	10.0

Age	Lithostratigraphy MOL-GT-03(-S1)			Actual		Thickness mTVD
				mBGL	m/TAW	
Cretaceous	Tongeren Gp	Zelzate Fm (Zz)	Ruisbroek Mb	313.0	-288.0	14.0
	Maldegem Fm (Ma)	Maldegem Fm (Ma)	Zomergem Mb	327.0	-302.0	2.0
			Onderdale Mb	329.0	-304.0	11.0
			Asse Mb	340.0	-315.0	11.5
			Wemmel Mb	351.5	-326.5	7.5
	Zenne Gp	Lede Fm (Ld)		359.0	-334.0	13.5
		Brussel Fm (Br)		372.5	-347.5	11.5
	Ieper Gp	Tielt Fm (Tt)	Egem Mb	384.0	-359.0	9.5
			Kortemark Mb	393.5	-368.5	7.0
		Kortrijk Fm (Ko)	Aalbeke Mb	400.5	-375.5	9.0
			Mons-en-Pévèle Mb	409.5	-384.5	37.0
			Orchies Mb	446.5	-421.5	34.0
Late Carboniferous	Landen Gp	Hannut Fm (Hn)	Grandglise Mb	480.5	-455.4	31.5
			Halen Mb	512.0	-486.9	55.5
			Waterschei Mb	567.5	-542.4	30.0
		Heers fm (Hs)	Gelinden Mb	597.5	-572.3	10.5
			Orp Mb	608.0	-582.8	3.0
	Chalk Gp	Houthem Fm (Ho)		611.0	-585.8	25.0
		Maastricht Fm (MMa)		636.0	-610.8	74.9
		Gulpen Fm (MGu)		711.0	-685.7	145.9
		Vaals Fm (MVA)		857.0	-831.6	40.5
		Charleroi Fm (PCh)		897.5	-872.1	692.9
Early Carboniferous	Belgian Coal Measures Gp	Châtelet Fm (PCa)	Floriffoux Mb	1615.5	-1565.0	423.6
			Ransart Mb	2117.2	-1989.0	205.1
		Andenne Fm (PAn)		2381.0	-2194.0	853.9
		Chokier Fm (PCo)		3548.0	-3047.9	11.3
		Souveré Fm (PSO)		3563.7	-3059.2	57.3
	Lower Carboniferous Limestone Gp (PK)	Goeree Fm (PGO)		3643.0	-3116.6	50.2
		Loenhout Fm (Plo)		3712.5	-3166.8	459.1
		Velp Fm (PVI) to Steentje Turnhout Fm (PSt)		4290.0	-3625.8	260.2
		Vesdre Fm (PVe)		4569.0	-3886.0	80.8
		Pont d'Arcole Fm (PPo)		4654.0	-3966.8	17.7
Devonian	Bosscheveld Fm (PBo)		4672.5	-3984.5	72.5	
	Condroz Gp (PC)	Evieux Fm (PEv)		4747.5	-4057.0	> 153.7
	Total Depth		4905.0	-4210.7		

The Cenozoic sediments have a thickness of about 610 m. They mainly consist of unconsolidated sands, silt layers and clay.

Below, almost 300 m of chalk and marl are encountered. These sediments belong the Chalk Group. The uppermost unit, the Houthem Formation, is of early Tertiary age (Early and Middle Danian). The

underlying units belong to the Late Cretaceous. The base of the Cretaceous is at a depth of about 900 m. It consists of an angular unconformity separating the Upper Carboniferous from the Cretaceous formations.

The Late Carboniferous consists of the Charleroi, Châtelet, Andenne and Chokier formations (Belgian Coal Measures Group). The coal measures consist mostly of carbonaceous, siliciclastic deposits. The facies evolves from open marine at the base over lower and upper delta plain to alluvial at the top. The age ranges from Namurian to Westphalian.

The upper part of the Late Carboniferous sequence is coal bearing. The Charleroi Formation is characterized by a rhythmic alternation of siltstone, claystone, sandstone and coal without clear sedimentological pattern. The Châtelet Formation is characterized by three sedimentological cycles that start with a coarsening upward sequence and end with an alternation of sandstone and siltstone beds. Marine claystone beds occur at the base of each sequence. The base of the Châtelet Formation is formed by an organic claystone that corresponds to a marine incursion known as the Sarnsbank marine band. The base of this bed forms the boundary between the Westphalian and the Namurian.

The Andenne Formation consists of claystone, siltstone and sandstone grading into each other. Ten coarsening upwards sequences can be recognized. They start with dark grey to black marine claystone and grade into silt- and sandstone. The sandstone beds often are whitish and tend to be well cemented. Traces of coal occur throughout, but locally some higher percentages were observed in the top part of some of the sequences.

The top of the Chokier Formation is marked by a gradual, but distinct increase in gamma-ray readings. Gamma ray readings in the Chokier Formation are generally above 150 API. The Spectral Gamma Ray log reveals that the increase in gamma ray is due to the increase in concentration of uranium.

Based on correlation with wells Merksplas, Poederlee and Halen, the top of the Souvré Formation is picked at a distinct drop in the gamma-ray log. Generally, gamma ray readings in the Souvré Formation are highly variable between 90 and 220 API. The Spectral Gamma Ray readings show high uranium concentrations of 20-30 ppm in the upper part. In the lower part, the uranium concentrations drop as the formation is becoming more calcareous with depth.

The Souvré Formation comprises mainly dark grey to dark brownish grey, moderately hard to hard, fissile, micro-micaceous, locally micro-pyritic claystone. The claystone is slightly to locally moderately calcareous, and locally siliceous. Lumps of pyrite are present. It forms the transition between the siliciclastic deposits of the Belgian Coal Measures Group and carbonate deposits of the Lower Carboniferous Limestone Group.

The top of the Carboniferous Limestone Group (top Goeree Formation) is at a depth varying between 3000 and 3600 m below surface (Figure 1, Figure 2). In MOL-GT-03, the first compact limestone bed is encountered at a depth of 3084 m (TVD) below surface. The bed marks the top of the Goeree Formation. Below, a 795 m thick (true stratigraphic thickness based on MOL-GT-03) sequence that predominantly consists of limestones and dolostones occurs. A lithological description of the Carboniferous Limestone Group, which is the target at the Balmatt geothermal site, is given in the next section.

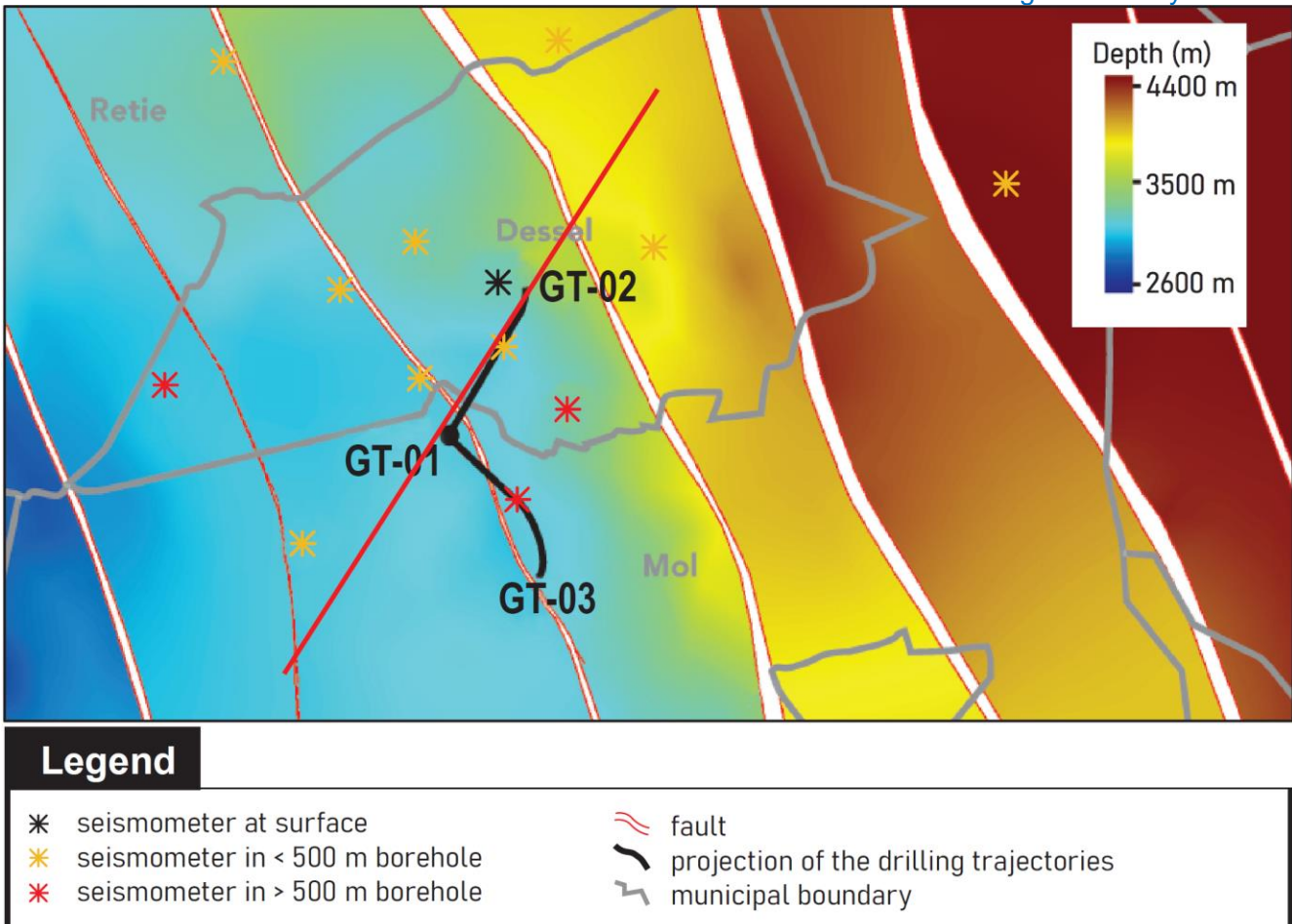


Figure 3: Depth map of the top of the Lower Carboniferous Limestone Group around the Balmatt geothermal site.

Below the carbonate sequence rests on the Bosscheveld Formation. The top of this formation is picked at the top of a ~3m thick limestone bed. A 1.5m thick claystone bed with high Uranium content marks the base of the formation. The Bosscheveld Formation comprises interbeds of dark grey to black claystone, and off white to light grey, brittle to hard, slightly dolomitic limestone. The carbonate content decreases with depth.

Sandstone of the Evieux Formation (Condroz Group) are present below the Bosscheveld Formation. The top of the formation was picked at the base of a high gamma ray peak (from Spectral Gamma Ray mainly uranium) marking the base of the overlying Bosscheveld Formation.

The Evieux formation comprises interbeds of white to beige to light greenish grey sandstone. Below 4840 m (MD) also brownish red, firm to hard, fine to medium, locally pyritic, locally silty and argillaceous sandstone grading to siltstone, and claystone occur. The claystone is dark grey to black, moderately hard, fissile, and locally pyritic.

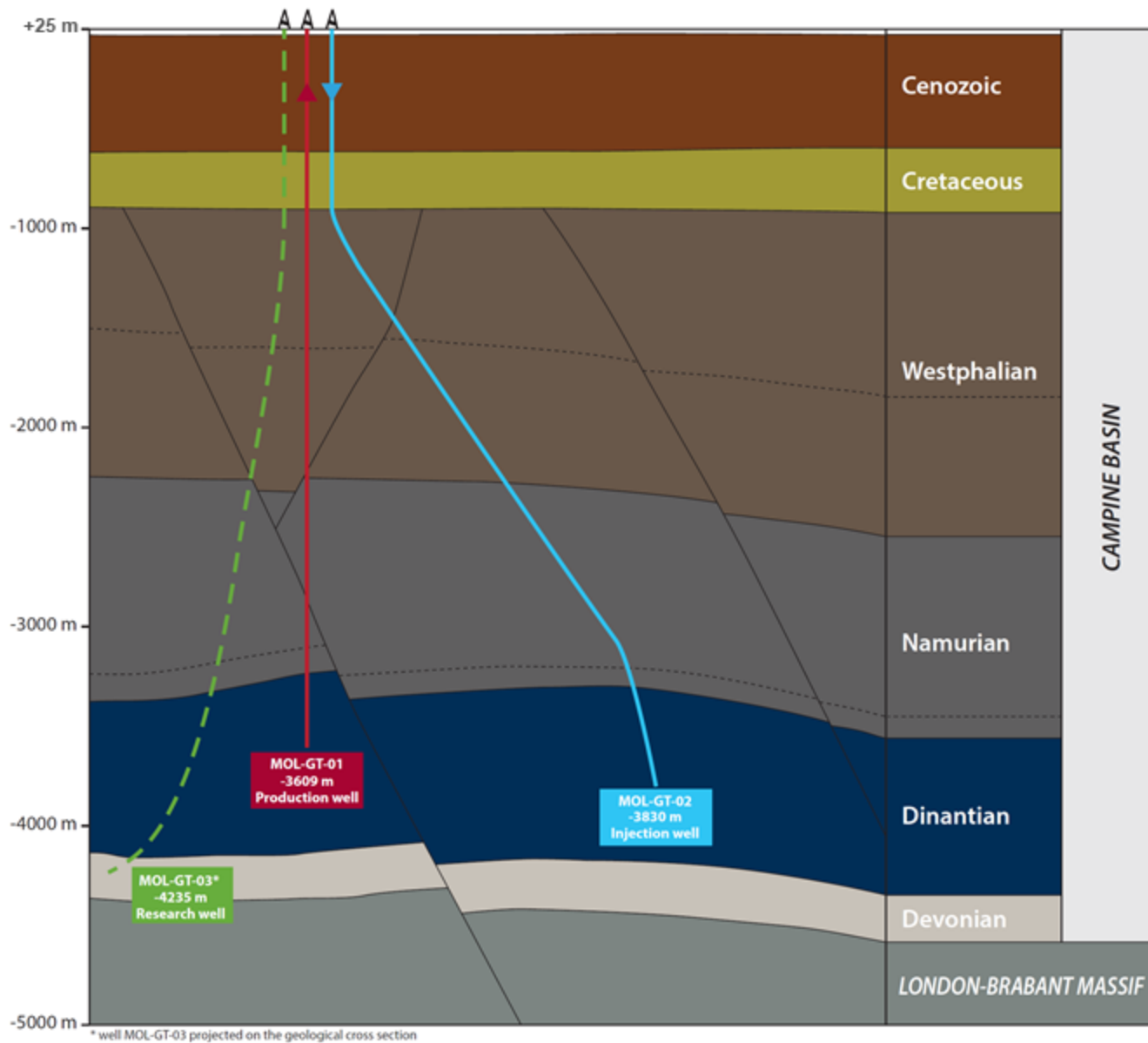


Figure 4: Geological cross section between wells MOL-GT-01 and MOL-GT-02 (Balmatt geothermal site). The trajectory of the cross section is shown as a red line in Figure 3.

Several NNW – SSE striking major faults, as well as smaller WNW – ESE striking f are encountered at and close to the Balmatt site, intersecting the Dinantian carbonates, i.e., the Dessel fault, Beringen Fault and Retie Fault. These are normal faults, with dips ~60° to the (E)NE (Figure 2). Production well MOL-GT-01 targets the normal fault zone of the Beringen Fault, whereas the injection well MOL-GT-02 targets a reservoir section which was originally presumed to be not influenced by a fault.

Description of the geothermal target

Depth and thickness

The geothermal target is Lower Carboniferous Limestone Group. The top of the target is situated at a depth that varies from about 2700 to 4000 m. In the three wells, the top of the limestones was reached at 3054 to 3298 m below ground level (Table 3). MOL-GT-03 drilled the entire Lower Carboniferous.

The thickness of the sequence corrected for deviation and dip of the strata measures 830 m. This includes the transitional beds of the Souvré Formation at the top of the sequence, and of the Bosscheveld Formation at the bottom of the sequence. The sequence of limestone and dolomite is 760 m thick.

Table 3: Depth of the tops and thickness of the Lower Carboniferous formations encountered in the wells Mol-GT-02 and MOL-GT-03. For MOL-GT-03 see Table 2.

Formation	depth top (mBGL)	mTAW	Thickness (mTVD)
MOL-GT-01-S1			
Souvré Fm (PSo)	3109.5	-3082.8	65.9
Goeree Fm (PGo)	3175.5	-3148.8	59.1
Loenhout to Velp Fm (PLo)	3227.5	-3200.7	> 382.2
TD	3610.0	-3582.9	
MOL-GT-02			
Souvré Fm (PSo)	3723.0	-3211.6	61.1
Goeree Fm (PGo)	3787.5	-3272.7	49.1
Loenhout to Velp Fm (PLo)	3839.0	-3321.8	> 483.4
TD	4341.0	-3805.2	

Lithology

The target for the Balmatt geothermal project is limestones and dolostones of the Carboniferous Limestone Group. It is one of the potential geothermal reservoirs identified in the Campine basin (Berckmans & Vandenberghe, 1998). In the Campine area, the upper part of the sequence is formed by stacked shallow marine and reefal limestones that were deposited on a carbonate platform. The sequence can be several hundreds of meters thick. It can be subdivided in at least 3 major depositional cycles that are separated from each other by emersion horizons and/or erosional surfaces. The limestones rest conformably on a sequence of aggrading lime- and dolostones (Figure 3).

The limestones and dolostones were deposited during the Early Carboniferous. Since then, these rocks were subjected to diagenetic and tectonic processes that have strongly influenced their porosity and permeability. This has resulted in a generally compact rock mass that is locally transected by highly permeable veins and fault zones.

At the project site, the Lower Carboniferous Limestone Group is subdivided in the Goeree, Loenhout, Velp to Steentje-Turnhout, Vesdre, Pont d'Arcole and Bosscheveld formations based on log correlation and cuttings description. The transition from the Souvré to the Goeree Formation is transitional. The top of Goeree Formation was put at the point where Gamma Ray readings fall to a level that is significantly lower than in the overlying beds and that coincides with a significant increase in limestone in the cuttings. The overall sonic velocity values also increase compared to the overlying Souvré Formation.

The description of the lithology of the different formations is based on the description of the cuttings by the mud loggers. These descriptions do not allow to understand the texture of the carbonate deposits in terms of the Dunham classification. Instead, they were generally described on basis of their crystallinity.

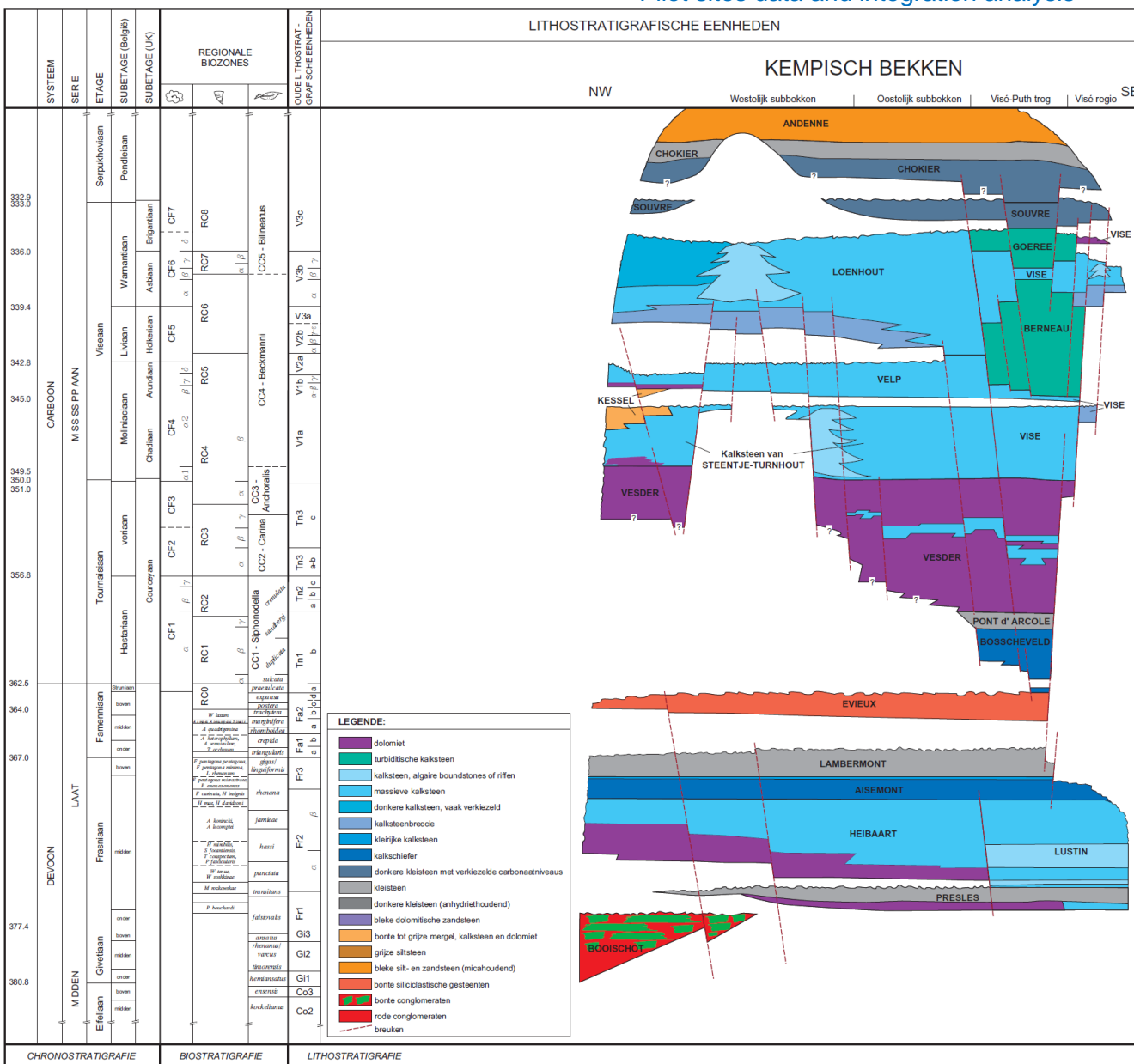


Figure 5: Lithostratigraphy of the Lower Carboniferous Limestone Group and older formations in the Campine Basin and adjacent areas. The Balmatt project is situated in the easternmost part of western sub-basin (Laenen, 2003)

Goeree Formation

The Goeree Formation consists of limestone beds interbedded with mostly thin claystone beds. The limestones beds are typically centi- to decimeters thick, light to medium grey in color, moderately hard, and have a micro-crystalline texture. The claystones are dark grey, hard, calcareous, siliceous and contain pyrite.

Loenhout Formation

The top of the formation is taken at the start of a longer interval with low Gamma Ray readings of about 20 API on average. The sequence is described as "micro to fine crystalline" predominantly off white to light grey limestone.

Thin claystone beds occur throughout, but are more frequent from 3823 to 3960 m and from 4068 to 4103 m. The latter interval reveals high concentrations of uranium on the Spectral GR-log. The claystone is described as: dark grey to black, platy, moderately hard to hard, micro-micaceous.

Traces of calcite were recorded through the entire Loenhout Formation. Chert was observed between 3730 to 3810 m.

Velp Formation to Steentje-Turnhout Formation

The top of the Velp Formation and/or Steentje-Turnhout Formation was picked at the base of a small gamma-ray peak. Based on the cuttings, it is impossible to make a distinction between the Velp and Steentje-Turnhout Formation

The top of this sequence roughly coincides with a change in color of the limestone from light gray to dark grey. The limestone is moderately hard to hard, and micro to fine crystalline in texture. Locally, thin calcareous claystone beds occur. They are hard and splintery and contain some pyrite. Thin calcite veins are present, as well as traces of chert.

Vesdre Formation

The top of the Vesdre formation is recognized by slightly higher density readings and higher sonic velocities, indicating a more dolomitic lithology. The higher dolomite content is confirmed by calicimetry.

The formation consists of dark grey, to locally off-white dolomitic limestone and dolomite. Locally very thin streaks of dark grey to black claystones are present. Thin beds of anhydrite and/or anhydritic dolomite are inferred from locally very high density readings.

Pont d'Arcole Formation

The Pont d'Arcole Formation consists of an 18 m thick claystone dominated sequence. The claystone is dark grey to black and contains pyrite. Thin interbeds of light to dark grey limestone are present.

Thermal properties (e.g., heat capacity, thermal conductivity, heat generation)

Heat production

The heat production of the limestones and the overlying formations were calculated from massic activities of ^{238}U , ^{228}Th , and ^{40}K in cutting samples measured using gamma-spectroscopy (Pauwels et al., 2019). The limestones have a heat production of about 0.7 nW/kg or less (Table 4). At an average density of 2700 kg/m³, this corresponds to a heat production of about 2 $\mu\text{W}/\text{m}^3$ or less. Uranium is typically contributing for 90% or more to the heat production. The highest values correspond to shaly or dark grey limestone beds.

The heat production calculated for the sample of the Goeree formation is higher than for the underlying Loenhout Formation. The higher heat generation of this sample is due to a high activity of ^{238}U . The sample has a higher clay content than the samples of the Loenhout Formation and contain 3% of pyrite. The latter is indicative for reducing conditions in the sediment. Such conditions improve the preservation of organic matter.

The sample of the Souvré Formation has a heat production of 2.4 nW/kg (about 6.3 $\mu\text{W}/\text{m}^3$). The high heat production is due to the high activity of ^{238}U and of ^{232}Th . The contribution of uranium can be linked to the organic matter content of the sample, the contribution of thorium the clay content of 38%.

The sample of the Chockier Formation has a heat production of 1.1 nW/kg (about 2.9 $\mu\text{W}/\text{m}^3$). 30% of the heat production comes from the decay of ^{232}Th . The high thorium concentration is related to the high clay content (50%) of the sample.

Table 4: Heat generation of the Lower Carboniferous limestones and the overlying formations based on massic activities of ^{238}U , ^{228}Th , and ^{40}K measured using gamma-spectroscopy. Uncertainty is given as expanded uncertainty ($k=2$).

Formation	Depth	HG rock ($\mu\text{W}/\text{kg}$)	Contribution ^{238}U
Chockier Fm.	3100	1.10E-03 \pm 5.15E-04	68.8%
Souvré Fm.	3130	2.37E-03 \pm 1.17E-03	86.7%
Goeree Fm.	3200	1.12E-03 \pm 3.51E-04	95.3%
Loenhout Fm.	3235	3.92E-04 \pm 1.49E-04	93.3%
Loenhout Fm.	3255	< 2.69E-04 \pm 9.90E-05	90.5%
Loenhout Fm.	3260	< 2.91E-04 \pm 9.14E-05	89.0%
Loenhout Fm.	3405	5.77E-04 \pm 2.50E-04	91.1%
Loenhout Fm.	3430	< 6.69E-04 \pm 2.89E-04	93.3%
Loenhout Fm.	3460	7.43E-04 \pm 3.98E-04	92.2%
Loenhout Fm.	3470	7.85E-04 \pm 2.37E-04	95.1%
Loenhout Fm.	3510	5.26E-04 \pm 2.31E-04	76.8%
Loenhout Fm.	3560	< 5.15E-04	(88.8%)

Table 5: Heat generation of the Lower Carboniferous limestones and the over- and underlying formations based on the spectral gamma-ray logs.

	Heat generation ($\mu\text{W}/\text{kg}$)					Contrib. ^{238}U	
	mean	std	min	50%	max	mean	max
Chokier Fm	1.51E-03	4.76E-04	6.13E-04	1.47E-03	2.50E-03	85.2%	91.8%
Souvré Fm	1.68E-03	7.28E-04	4.11E-04	1.56E-03	5.23E-03	90.1%	99.5%
Goeree Fm	6.04E-04	3.59E-04	6.09E-05	5.43E-04	2.26E-03	90.7%	99.1%
Loenhout Fm	3.93E-04	2.81E-04	2.35E-05	3.16E-04	2.80E-03	85.5%	100.5%
Velp Fm	2.56E-04	1.08E-04	6.58E-05	2.39E-04	9.53E-04	77.9%	96.8%
Steentje-Turnhout Fm	2.10E-04	8.80E-05	5.35E-05	2.06E-04	4.38E-04	82.0%	96.0%
Vesdre Fm	1.99E-04	9.71E-05	6.47E-05	1.74E-04	4.63E-04	66.1%	95.0%
Pont d'Arcole	5.10E-04	1.68E-04	1.75E-04	5.15E-04	7.83E-04	41.5%	61.3%
Bosscheveld Fm	5.05E-04	1.90E-04	8.08E-05	4.96E-04	1.45E-03	34.0%	60.1%
Evieux Fm	5.65E-04	2.70E-04	1.78E-04	5.29E-04	2.87E-03	41.8%	84.4%

The heat production was also calculated from the spectral gamma-ray logs using the formula given by Rybach, 1988 (Table 5). For the Chokier, Souvré and Loenhout formations, the figures are similar as those calculated from the massic activities. The logs also give an estimate of the heat production within the underlying formations. In general, the heat production of the limestones of the Velp and Steentje-Turnhout formations is 0.22 nW/kg (0.6 $\mu\text{W}/\text{m}^3$). That is about half the heat production calculated for the Loenhout formation.

The Vesdre formation has the lowest heat production: on average 0.2 nW/kg (0.55 $\mu\text{W}/\text{m}^3$). The formation mainly consists of pure dolostone and limestone.

The transitional beds of the Pont d'Arcole and Bosscheveld formations have a heat production of about 5 nW/kg (1.3 $\mu\text{W}/\text{m}^3$) (Table 5). In comparison to the overlying limestones formations, the contribution of ^{238}U to the heat production is lower. This suggests shale is to a large part contributing to the heat

production, whereas other minerals (i.e., related to diagenetic remobilization of uranium through fractures) or organic matter are responsible for most of the heat production in the overlying limestones.

Thermal conductivity

There are no thermal conductivity measurements available from the Lower Carboniferous Limestone Group. As a first estimate, the thermal conductivity of the matrix was calculated from quantitative XRD-analyses on cuttings from MOL-GT-01 (Pauwels, 2021). The mixing rule and thermal conductivity of the pure mineral phases given by Clauser and Huenges (1995) were used. The impact of temperature on the thermal conductivity of the pure minerals was calculated using the correlation given by Zoth and Hänel (1988). For minerals for which this correlation has not been established, the generic formula given by Sass et al. (1992) was used. The results are shown in Table 6.

Table 6: Matrix thermal conductivity of the Lower Carboniferous limestones and the overlying formations based on mineralogy defined by XRD.

Formation	depth m	TC matrix (25°C) W/m.K	TC matrix (140°C) W/m.K	shale	quartz
Chockier Fm.	3100	2.00	1.41	59.5%	30.3%
Souvré Fm.	3130	2.78	1.98	42.0%	40.9%
Goeree Fm.	3200	4.44	3.28	10.4%	48.7%
Loenhout Fm.	3235	4.57	3.40	6.1%	45.6%
Loenhout Fm.	3255	4.67	3.52	2.0%	41.2%
Loenhout Fm.	3260	4.91	3.67	2.1%	47.2%
Loenhout Fm.	3405	3.69	2.85	4.0%	19.1%
Loenhout Fm.	3430	3.65	2.83	4.0%	19.0%
Loenhout Fm.	3460	3.88	2.98	4.0%	24.2%
Loenhout Fm.	3470	3.72	2.85	6.1%	23.2%
Loenhout Fm.	3510	3.82	2.90	7.3%	28.1%
Loenhout Fm.	3560	3.99	3.09	0.0%	23.5%

The thermal conductivity of the mineral matrix at ambient temperature varies between 2 and 4 W/m.K. The clay-rich sample from the Chockier Formation has the lowest matrix conductivity. The matrix conductivity of the samples from the Loenhout formation under reservoir conditions (140 °C and 320 bar) vary around 3 W/m.K. Samples with a high (diagenetic) quartz content have the highest matrix conductivities.

Table 7 shows the thermal conductivity of the matrix and the mineralogy calculated from the spectral gamma, litho density and sonic log from MOL-GT-03. The values are similar to those calculated from the XRD-data. The high values of the Souvré and Goeree formation are due to the high quartz content. The high quartz content is confirmed by the cuttings. It is mostly diagenetic quartz. The uppermost part of part Loenhout Formation also contains levels that are rich in diagenetic quartz. The matrix thermal conductivities calculated for the Pont d'Arcole and Bosscheveld formations vary around 2 W/m.K. The overall lower conductivities of these formations are explained by the high clay content and/or occurrence of clay layers and a low quartz content.

Table 7: Calculated matrix thermal conductivities of the Lower Carboniferous limestones and the over- and underlying formations based on geophysical logs.

	TC matrix (25°C)		TC matrix (140°C)		shale		quartz	
	W/m.K		W/m.K					
	Aver.	Std.	Aver.	Std.	Aver.	Std.	Aver.	Std.
Souvré Fm	3.79	0.57	2.87	0.41	11.5%	5.6%	23.3%	13.8%
Goeree Fm	3.85	0.53	3.00	0.36	3.3%	3.3%	10.7%	14.8%
Loenhout Fm	3.58	0.51	2.81	0.37	3.4%	5.5%	4.8%	11.1%
Velp Fm	3.40	0.25	2.69	0.19	2.6%	1.8%	0.8%	4.0%
Steenjje-Turnhout Fm	3.63	0.39	2.86	0.28	1.5%	0.9%	3.3%	8.3%
Vesdre Fm	3.75	0.68	2.96	0.55	4.6%	5.6%	0.5%	3.1%
Pont d'Arcole	2.74	0.56	2.10	0.44	24.9%	12.7%	4.0%	8.7%
Bosscheveld Fm	2.48	0.55	1.90	0.43	28.8%	14.9%	1.7%	7.7%
Evieux Fm	3.73	0.98	2.79	0.68	19.4%	9.2%	24.3%	22.7%

Table 8 shows the calculated thermal conductivity of the formation under ambient and reservoir temperature conditions for MOL-GT-03. For all formations the figures are similar to the calculated matrix thermal conductivities. The impact of porosity on the thermal conductivity is small. This is due to the low porosity of the lithologies: between 2 and 4% in the lime- and dolostones, and 1 and 2 in the transitional beds at the base of the Lower Carboniferous and in the Evieux Formation.

Table 8: Calculated thermal conductivities of the Lower Carboniferous limestones and the over- and underlying formations based on geophysical logs. Porosity is the average value of density and sonic (DTP) porosity.

	TC lithology (25°C)		TC lithology (140°C)		porosity	
	W/m.K		W/m.K			
	Aver.	Std.	Aver.	Std.	Aver.	Std.
Souvré Fm	3.35	0.52	2.59	0.38	7.0%	2.5%
Goeree Fm	3.57	0.50	2.81	0.34	4.2%	1.5%
Loenhout Fm	3.34	0.44	2.65	0.32	3.9%	2.5%
Velp Fm	3.22	0.21	2.56	0.16	3.1%	1.3%
Steenjje-Turnhout Fm	3.42	0.35	2.72	0.25	3.4%	1.2%
Vesdre Fm	3.62	0.67	2.88	0.54	2.0%	2.2%
Pont d'Arcole	2.68	0.54	2.06	0.43	1.3%	1.1%
Bosscheveld Fm	2.41	0.51	1.85	0.41	1.8%	1.7%
Evieux Fm	3.60	0.92	2.71	0.64	2.0%	1.5%

Specific heat

There are no direct measurements of the specific heat available for the Lower Carboniferous Limestone Group. To get an estimate for the limestones and the overlying formations, the specific heat was calculated using the formula provided by Robertson (1988) and the results of quantitative XRD-analyses on cuttings from MOL-GT-01 (Pauwels, 2021). The correlations of specific heat versus temperature published by Robie and Hemingway (1995) were used to define the specific heat for the pure phases.

The average specific heat of the samples from of the Lower Carboniferous Limestone Group under reservoir conditions (140°C, 320 bar) is 0.93 J/g.K. Similar values are calculated for the samples of the overlying formations.

Table 9: Specific heat of the Lower Carboniferous limestones and the overlying formations based on mineralogy defined by XRD.

Formation	Depth (m)	Cp at 25°C (J/g.K)	Cp at 140°C (J/g.K)
Chockier Fm.	3100	0.777	0.913
Souvré Fm.	3130	0.765	0.894
Goeree Fm.	3200	0.78	0.904
Loenhout Fm.	3235	0.792	0.918
Loenhout Fm.	3255	0.799	0.927
Loenhout Fm.	3260	0.791	0.916
Loenhout Fm.	3405	0.817	0.956
Loenhout Fm.	3430	0.813	0.95
Loenhout Fm.	3460	0.81	0.946
Loenhout Fm.	3470	0.808	0.944
Loenhout Fm.	3510	0.801	0.932
Loenhout Fm.	3560	0.81	0.945

Geomechanical properties

No core material of the Dinantian carbonates from the Balmatt wells is available, the estimation of geomechanical formation properties is thus mainly based on well measurements and empirical relation derived from laboratory experiments. Wassing et al., (2022) provide the most recent update of the geomechanical data from the Balmatt site.

In this section, the geomechanical data for the Balmatt geothermal site reported by Wassing et al., (2022) are summarized. The estimation of formation properties (density and elastic rock parameters), pressure and in-situ stress magnitude and orientation and fracture and fault properties are presented. Note that no information on the elastic properties of the over- and underlying formations is available.

Formation properties

Dynamic elastic parameters and density

The dynamic elastic parameters have been derived from compressional and shear wave travel times measured for well MOL-GT-01. The sonic logs and density files of well MOL-GT-01 were analysed and the elastic parameters i.e., the dynamic Young's modulus (E_d) and Poisson's ratio (ν_d) were calculated. The variation of compressional and shear wave velocities, density and dynamic elastic parameters as a function of depth for well MOL-GT-01 is presented in Figure 6 .

Bulk densities for the Dinantian carbonates derived from the well logs are generally higher than 2600 kg/m³, whereas shallower deposits have lower densities, with an average of around 2360 kg/m³ for the upper 2000 m.

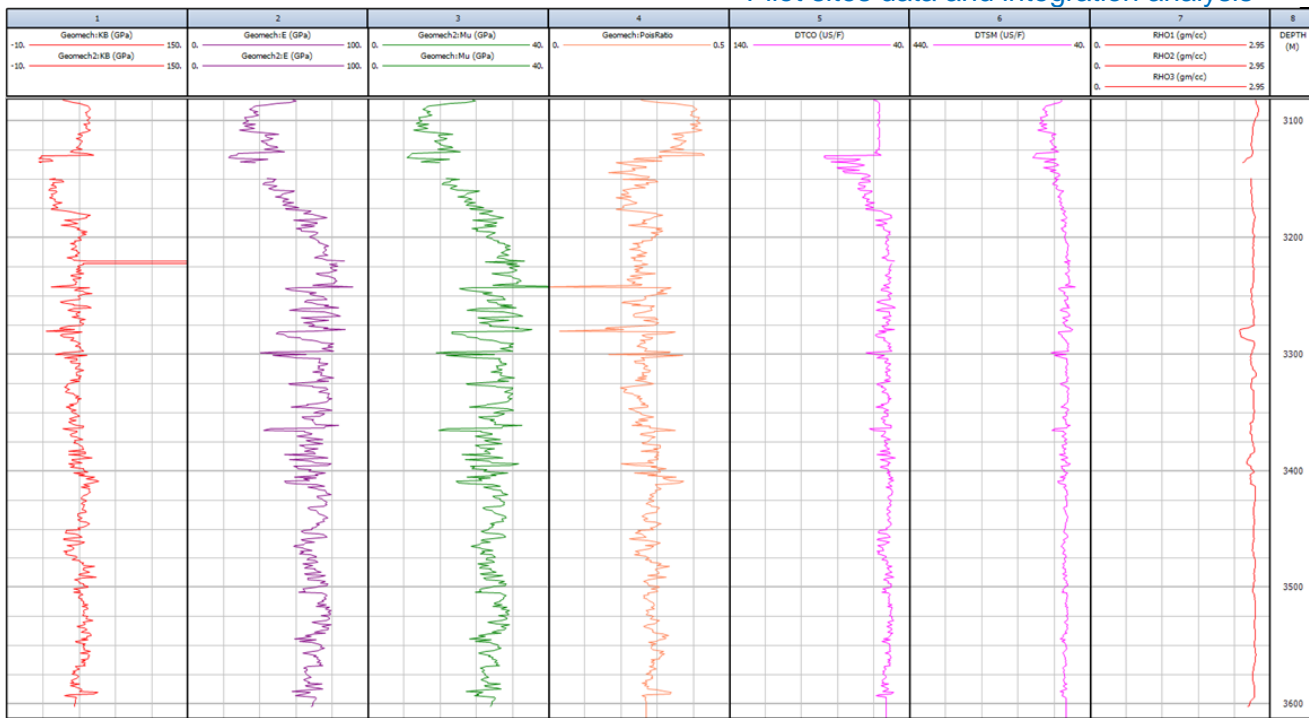


Figure 6: Variation of elastic parameters bulk modulus (1st column), Young's modulus (2nd column), shear modulus (3rd column), Poisson's ratio (4th column), compressional wave velocity (5th column), shear wave velocity (6th column) and density (7th column) as a function of depth.

Static elastic parameters

Ideally core plug measurements are required to determine the static elastic parameters. Unfortunately, as mentioned previously, no core material of the Dinantian carbonates from the Balmatt site is available. In that case, the static elastic parameters must be estimated from the dynamic moduli assuming that a reliable relationship between the two is available. Such a relationship is however not straightforward.

For an initial estimation of the static Young's modulus E_s , the relation from Najibi et al. (2015) for carbonate rocks has been used by Wassing et al., (2022):

$$E_s = 0.014E_d^{1.96} \quad [1]$$

Applying the above relationship to the dynamic elastic parameters presented in Figure 6 results in an average static Young's modulus E_s of 52 GPa and v_d of 0.28.

These values can be compared to the ones obtained when using the relation between dynamic and static Young's modulus and Poisson's ratio derived by Wassing et al., (2022) for Dinantian carbonates similar to the ones of the Balmatt reservoir. The relation they developed is based on a combination of laboratory triaxial deformation and acoustic (compressional and shear wave) velocity measurements for outcrop samples of Dinantian (Visean and Tournaisian) carbonates from quarries. The three outcrops samples they used are detailed in Table 10. Triaxial tests were performed at different effective confining stress and axial stress conditions.

In the experiments, both elastic and dynamic moduli from outcrop samples were measured corresponding to the same Dinantian formations as the Balmatt reservoir. It should be noted, however, that burial and exhumation histories are very different between the outcrop and reservoir formations. It remains of interest to compare values with samples from cores of the Dinantian carbonates at depth, should they become available.

The relationship that was proposed by the authors for Young's modulus follows a power law that allows them to build an empirical relationship for each formation:

- Visean limestone (MOHA):

$$\frac{E_d}{E_s} = 1.916 P_e^{-0.013} \quad [8]$$

- Tournaisian dolostone (MLD):

$$\frac{E_d}{E_s} = 2.527 P_e^{-0.054} \quad [9]$$

They identified a roughly linear relationship between v_d/v_s and P_e , which allows to establish the following relationships for dynamic/static Poisson's modulus:

- Visean limestone (MOHA):

$$\frac{v_d}{v_s} = 0.032 P_e + 1.126 \quad [10]$$

- Tournaisian dolostone (MLD):

$$\frac{v_d}{v_s} = 0.034 P_e + 1.410 \quad [11]$$

Finally, the experiments have also shown that differences in effective stress and porosity can have a strong influence on the elastic moduli. An alternative empirical power law relation between static and dynamic Young's modulus was derived for each formation:

- Visean limestone (MOHA):

$$E_s = 9.04 \times 10^{-7} E_d^{4.1} \quad [12]$$

- Tournaisian dolostone (MLD):

$$E_s = 0.015 E_d^{1.8} \quad [13]$$

No relationship between the static and dynamic Poisson's ratio could be established.

Combining sonic well logs with either the relation of Najibi et al. (2015) or the newly derived relations proposed for the Visean limestone or the Tournaisian dolostone leads to different geomechanical characterization of the reservoir at Balmatt. Indeed, Najibi et al. (2015) predicts a $E_s = 52$ GPa for a dynamic Young's modulus of ~66 GPa for the reservoir section at MOL-GT-01, while the Visean relation predicts $E_s = 26$ GPa and the Tournaisian relation predicts $E_s = 28$ GPa. If the outcrop samples used by Wassing et al., (2022) are more representative of mechanical behaviour of the Dinantian carbonates than the oil-producing limestones in Iran at unconfined conditions from Najibi et al. (2015), E_s is thus likely significantly overestimated by a factor of ~2. The dynamic Poisson's ratio ($v_d = 0.28$) is lower than experimentally derived values at reservoir conditions ($0.33 < n_d < 0.35$).

Table 10: Experimental data collected for the three outcrop samples.

Parameters	MOHA_3	MLD_L5_1	MLD_L6_1
Quarry	Moha	Marche-les-Dames	Marche-les-Dames
Formation	Visean	Tournaisian	Tournaisian
Lithology	Limestone (massif)	Dolostone (karst)	Dolostone (karst)
Length (mm)	47.543 ± 0.047	46.832 ± 0.025	47.907 ± 0.025
Diameter (mm)	25.198 ± 0.037	25.307 ± 0.021	25.133 ± 0.015
Test time (h)	118.5	146.3	23.8
Porosity (%)	0	2.31	2.63
Density matrix (g/cm ³)	2.66	2.83	2.87
Density saturated (g/cm ³)	2.66	2.79	2.82
Pe* at Failure (MPa)	35	35	1
σ_d at failure (MPa)	260	325	161
E_s at Pe = 1 MPa (GPa)	37.90 ± 1.23	25.41 ± 2.31	35.06 ± 1.78
E_d at Pe = 1 MPa (GPa)	72.64 ± 0.07	64.87 ± 0.13	75.09 ± 0.14
E_d/E_s at Pe = 1 MPa	1.917 ± 0.060	2.552 ± 0.227	2.142 ± 0.104
E_s at Pe = 35 MPa (GPa)	40.00 ± 0.02	36.66 ± 0.06	-
E_d at Pe = 35 MPa (GPa)	73.31 ± 0.08	77.79 ± 0.20	-
E_d/E_s at Pe = 35 MPa	1.833 ± 0.001	2.122 ± 0.002	-
v_s at Pe = 1 MPa	0.259 ± 0.008	0.260 ± 0.025	0.295 ± 0.007
v_d at Pe = 1 MPa	0.340 ± 0.001	0.358 ± 0.001	0.344 ± 0.001
v_d/v_s at Pe = 1 MPa	1.311 ± 0.040	1.381 ± 0.129	1.169 ± 0.024
v_s at Pe = 35 MPa	0.152 ± 0.009	0.126 ± 0.038	-
v_d at Pe = 35 MPa	0.341 ± 0.001	0.333 ± 0.001	-
v_d/v_s at Pe = 35 MPa	2.240 ± 0.138	2.654 ± 0.801	-

± error: propagated from standard deviations and device accuracy.

* Pe : Effective Confining Stress

In addition, bulk modulus (Kd) based on experimentally-derived v_p and v_s measurements on quarries samples would be in the range of 75-80 GPa at reservoir conditions, which higher than the log-derived values. Note that given the lack of data on reservoir samples, it remains unsure to what extent the outcrop samples are representative of the mechanical behaviour of the Dinantian carbonate reservoir at Balmatt.

In-situ stress characterisation

In-situ stress directions were obtained from caliper data and borehole image logging (Formation Microlmager – FMI) performed in the openhole sections of wellbore MOL-GT-01.

Drilling induced fractures

The open-hole sections between 3169 and 3604.5 m MD logged in MOL-GT-01 show a large number of drilling-induced fractures, with a consistent NNW-SSE orientation. Few borehole breakouts were observed with a general ENE-WSW orientation. In addition, caliper data show a slight ovalization of the borehole in the ENE-WSW axis. Caliper data, drilling-induced fracture orientations (SHmax-direction)

and borehole breakouts (Shmin-direction) reveal a consistent NNW-SSE orientation for the maximum horizontal stress (SHmax) and an ENE-WSW orientation for the minimum horizontal stress (Shmin). The orientations of drilling induced fractures in MOL-GT-03 seem to confirm the stress directions from MOL-GT-01. However, as the maximum well deviation of well MOL-GT-03 is 45°, the results give no direct relationship between orientation of breakouts and fractures and the in-situ stress field.

Magnitudes of principal stresses are poorly constrained due to the scarcity of Leak-off Test (LOT) and Formation Integrity Test (FIT) data.

Natural fractures

A considerable amount of conductive fracture orientations was visible in MOL-GT-01, with a dominant orientation of NNW-SSE to N-S. Conductive fracture orientations in MOL-GT-03 have dominant orientations between NW-SE and NNW-SSE. These conductive features are generally interpreted as natural fractures that are filled with conductive material, such as clays.

Note however, that the distinction between these natural conductive fractures and drilling-induced fractures is difficult, and fractures may even be of natural and induced origin i.e., natural fractures enhanced by drilling. Occurrences of 8 faults have been described in MOL-GT-01, of which 5 minor and major faults are oriented E-W, one major fault N-S, one minor fault NW-SE and one minor fault WNW-ESE. Only two minor faults were interpreted for MOL-GT-03, oriented WNW-ESE.

Figure 7 and Figure 8 give an overview of breakout, fault and fracture orientations in borehole MOL-GT-01 and MOL-GT-03.

Dip Picking Results – Geological Feature Orientation

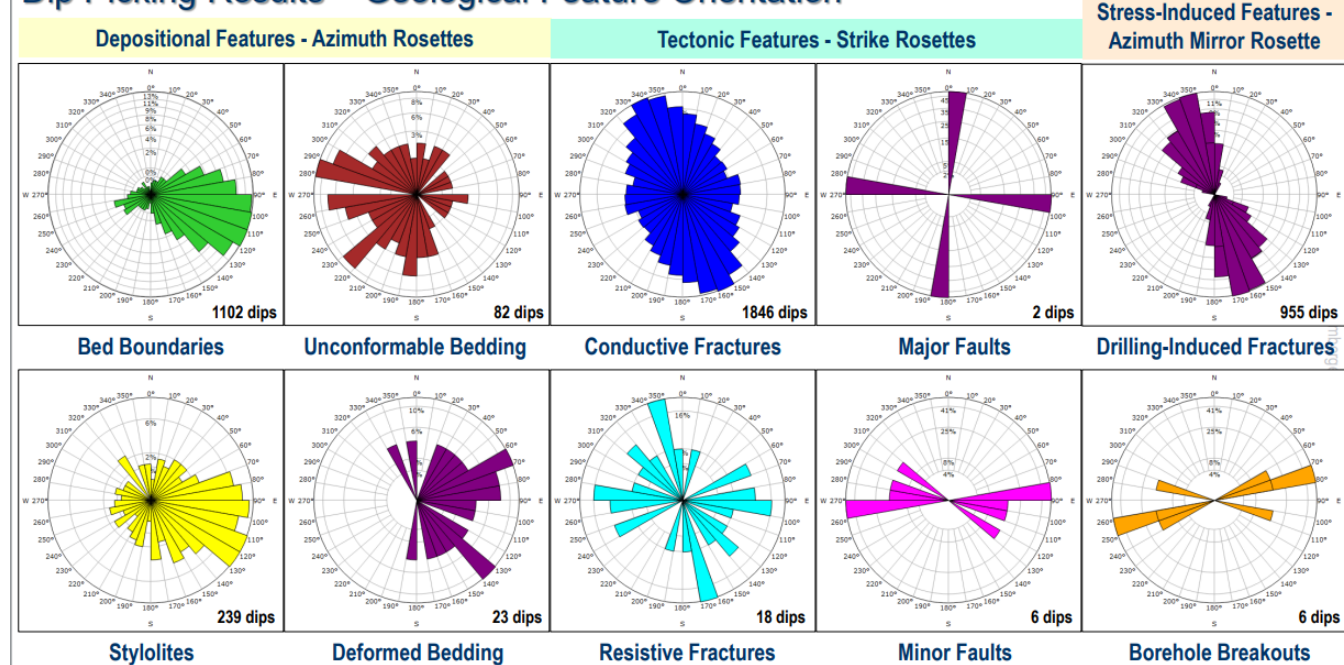


Figure 7: Geological feature orientations obtained from FMI-image log in open-hole section of MOL-GT-01-S1. From: Schlumberger presentation on FMI Image Analysis Results from Well MOL-GT-01-S1.

Interpreted Natural Fractures & Faults – Stereographic Analysis

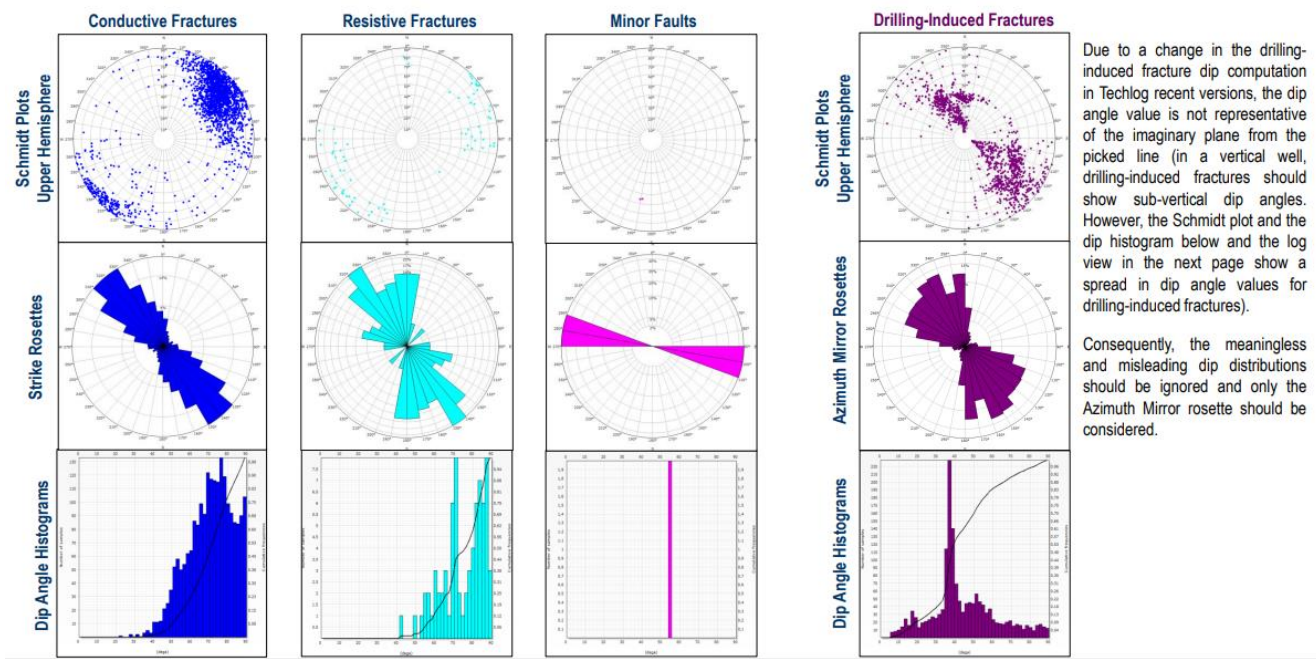


Figure 8: Geological feature orientations obtained from FMI-image log in open-hole section of MOL-GT-03-S1. From: Schlumberger presentation on FMI Image Analysis Results from Well MOL-GT-03-S1.

Flow properties

Porosity

The density and sonic logs of Mol-GT-03 were used to estimate the porosities of the Lower Carboniferous Limestones Group and the underlying formations. A series of cross-plots of density and Compressional Slowness were produced in order to obtain a rough idea of the porosities in each formation (Figure 9). The plot refers to waterwet formation with fluid slowness of 189 us/ft.

The calculated porosities are in the range of 2 to 5%. The overall porosity of the limestone and dolomite beds is low. Open fractures locally result in higher porosities (Table 11).

The porosity of the underlying Evieux formation is in the range of 0 to 1%.

Table 11: Porosity range for the formations of the Lower Carboniferous Limestone Group and the underlying formations derived from the cross-plots of density versus Compressional Slowness for MOL-GT-03.

Formation	Remark	Porosity
Souvré formation	Too high shale content, plots too far to the right	-
Goeree formation	Predominantly Limestone	3-4%
Loenhout formation	Limestone	2-3%
Velp formation	Limestone	2-3%
Steentje-Turnhout formation	Limestone / Dolomitic Limestone	2-4%
Vesdre formation	Dolomite and Limestone	2-5%
Ponte d'Arcole	Too high shale content, plots too far to the right	-
Bosscheveld	Too high shale content, plots too far to the right	-
Evieux	Sandstone	0-1%

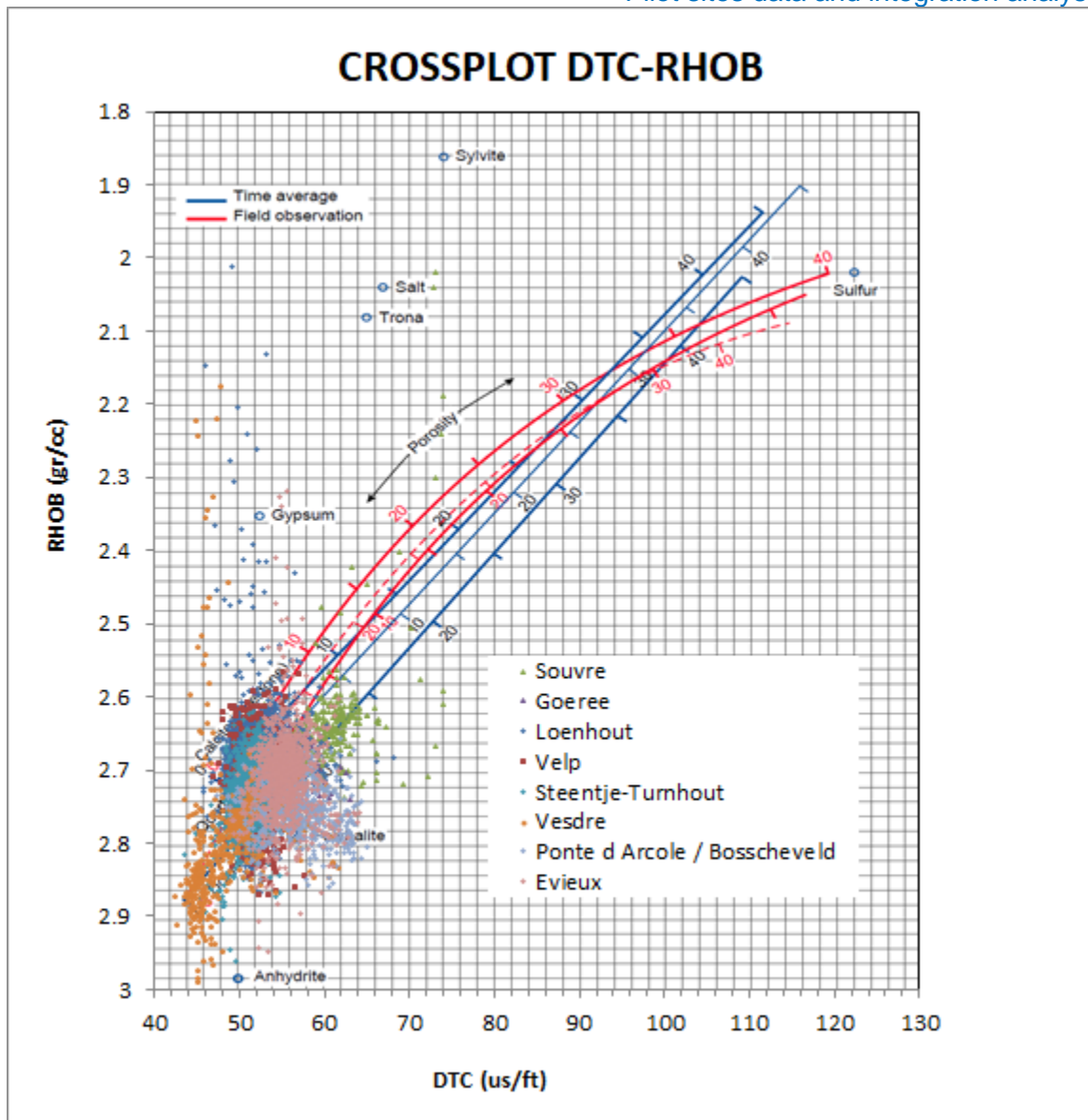


Figure 9: Cross-plots of Density versus Compressional Slowness for the lower sections of well MOL-GT-03.

Permeability thickness (kh)

Well tests were carried out on all three wells shortly after drilling was completed. Testing (production) of MOL-GT-01 up to a flow rate of 140 m³/h indicated a productivity index of 4 to 5 m³/h per bar, with a production temperature up to 128°C (Bos & Laenen, 2017). The well's permeability thickness (kh) is estimated to be 12-15 Dm.

Injection testing on MOL-GT-02 revealed a lower injectivity index, around 1.5-2 m³/h per bar. Based on the well's behavior during production in 2019, the permeability thickness is 5-6 Dm.

Initial well tests on MOL-GT-03 pointed to productivity far lower than anticipated. Production could not be initiated during a nitrogen lift test, whereas a short injection/falloff test revealed an injectivity of only 0.2 m³/h per bar. The permeability thickness of MOL-GT-03 is estimated to be below 1 Dm.

Observations from well Mol-GT-01 indicate that the permeability of the limestones is locally favorably influenced by the presence of fractures. The main zone where mud losses occurred during the drilling

of Mol-GT-01 is around 3280 m MD. In an attempt to locate the inflow points, a spinner flow measurement was performed after the third production test. However, the flowmeter blocked twice due to fine particles and iron flakes. Changes in the temperature log performed at the same time show that the main inflow points are between 3280 and 3420m MD. They correspond to the main loss zones during drilling.

The top of the interval coincides with a disturbance zone: around 3284 m depth, the FMI log of the lower section of MOL-GT-01 first shows an increase and then a decrease in the dip of the strata. This change in dip is interpreted as a fault cusp (van der Voet et al., 2020). MOL-GT-03 targeted the same fracture zone. As consequence a similar productivity was expected. However, no mud losses were observed during drilling, and the limestones in the vicinity of Mol-GT-03 appeared to be unproductive. This suggests that local differences in depositional environment, diagenesis and/or stress conditions strongly determine the permeability of the fracture zones.

The differences in k_h observed between the three wells show that the origin and maintenance of permeability in fracture zones, and in the reservoir in general, is a complex interplay between different processes. Several factors may have played a role, including (1) the structural context and the presence of fractures and their orientation within the current stress field (tendency to slip and dilatation), (2) the presence of fractures and their relationship to the mechanical properties of the layers, (3) the stratigraphic sequence and depositional conditions, (4) the diagenetic processes affecting the reservoir rocks, and (5) the presence of gas.

The contribution of the various factors and their interplay is not yet well understood. An in-depth analysis of the relationship between lithology and fracture density indicates that there is no correlation with lithotype or bed thickness (van der Voet, 2021). Lithology and depositional setting of the carbonates seems to have limited or no impact on the fracture pattern. Based on the current understanding the local stress field and diagenesis appear the important factors in defining which fractions are open and which are not.

Formation fluid

Chemical composition

The analyses of water samples taken during the production test are given in Table 12. The formation water is a Na(Ca)Cl brine with a TDS in the range of 126 and 144 g/l (11,6 – 13,1%_{wt}). Sodium and chlorine sign for 90% of the dissolved ions. Besides, the water contains minor amounts of Ca²⁺, Mg²⁺, K⁺, and SO₄²⁻. The composition of the brine is typical for deep sedimentary formation waters in contact with limestone.

The samples reveal a variable amount of dissolved iron. The iron measurement is likely skewed due to the airlift procedure. The injection of air will have resulted in the precipitation of dissolved iron in the aerated part of the wellbore. Moreover, the injection of oxygen in combination with high concentrations of electrolytes may have caused severe corrosion of the steel casing in the aerated part of the well.

The pH of the water samples taken at surface varies between 7,24 and 7,31. The HCO₃⁻ is about 150 mg/l. The pH-sensor in the production tubing recorded values between 5,1 and 5,9. It stabilized around 5,8 at the end of the last production step. The difference between the water samples and the continuous measurement can be explained by degassing of CO₂. Moreover, the oxidation of divalent iron also affects the pH. Within this respect, the readings of the pH-sensor will be closer to the actual pH than the results of the water samples.

Table 12: Concentration of major and minor cations and anions (all values except pH are in mg/l)

Sample	1611321-01	1611322-01	1611323-01	1611324-01
Na+	36500	37900	40500	38300
K+	2940	3300	3620	3240
Ca++	7100	7680	7970	7020
Mg++	462	506	519	494
Fe_total	0,147	84,8	0,081	149
Cl-	78200	83600	88000	94800
SO4--	192	261	269	278
HCO3-	155	173	137	122
CO3--	< 15	< 15	< 15	< 15
F-	3,05	3,05	3,05	3,05
pH	7,24	7,28	7,31	7,32

To get a reliable measurement of the dissolved iron content, pH and dissolved gasses, two pressurized downhole water samples were taken. When emptying the autoclaves, the fluids produced from the deep well MOL-GT-01 were clear water with a pH of 5.4. The fluid is slightly reducing (Redox potential SHE: 141 – 152 mV @20°C). The salt content is 165 g/l. The measured conductivity of approximately 184 mS/cm corresponds to that calculated from the ion concentrations. The concentrations of major and minor elements measured in these samples are shown in Table 13.

Table 13: Concentration of major and minor cations and anions measured in the downhole samples

Parameter	unit	MOL-GT01-3400m	MOL-GT01-3280m
Na+	mg/l	49800	49600
K+	mg/l	2770	2870
Ca++	mg/l	9160	9130
Mg++	mg/l	557	560
Sr++	mg/l	396	400
Ba++	mg/l	16.8	16.5
Fe++	mg/l	809	806
Mn++	mg/l	13.6	13.6
HNH4+	mg/l	267	264
Cl-	mg/l	98100	100200
HCO3-	mg/l	1117	1129
SO4--	mg/l	323	380
Br-	mg/l	153	134
F-	mg/l	< 0.88	< 0.88
pH		5.47	5.44
EC	mV	184.8	182.7

The downhole samples show a dissolved iron content of 800 mg/l. This is significantly higher than in the samples taken at surface. The difference in iron content between the surface and downhole samples suggests that most of the iron precipitated in the wellbore due to contact with oxygen. Indeed, when exposed to the air, the downhole samples turn brown due to the formation of iron-hydroxide.

Based on the chemical analyses of the 2 downhole samples, the density of the brine is estimated to be 1104 kg/m³ under standard conditions (25°C, 1 bar). This figure is similar to the density calculated from the pressure difference between the two downhole sensors (at 1000 and 2681.1 mTVDGL).

The heat capacity under standard conditions of is about 3527 J/kg.K.

Gas content

The amount of gas produced was estimated from the oxygen dilution measured in the exhaust of the geothermal separator with respect to the amount of oxygen in the injected air (20,95 %_{vol}) during the production teste on MOL-GT-01 (Table 14). Most of the gas emitted was water vapour. The average amount of dry gas emitted from the well – i.e., making abstraction of the amount of air injected – varied from 118 m³/h under normal conditions during step 1 to 320 Nm³/h in steps 2 and 3.

The ratio of the amount of gas released per m³ of water produced was 1,35 in step 1, 2,62 in step 2 and 2,93 in step 3. Most of the gas produced from the well is CO₂: 70 – 88 %_{vol}. The methane content was in the range of 11 to 15%_{vol}. Besides, trace amounts of H₂ and light hydrocarbons (C2 – C5) are present.

Table 14: Estimated average gas flow rates (gas from well is the estimated amount of dry gas released from the well) during the production tests on MOL-GT-01/

	O2 content (%vol)	wet gas flow (Nm ³ /h)	dry gas flow (Nm ³ /h)	gas flow from well (Nm ³ /h)
step 1	19,53	4770	1752	118
step 2	18,35	7130	2603	323
step 3	18,42	7100	2592	313

Two pressurized downhole water samples were taken to verify the findings of the production tests. The gas content and gas composition measured in the downhole samples are in line with the measurements during the production test. The gas content is in the order of 2,5 Nm³ of gas per m³ of formation water. The main component is CO₂. Besides, minor amounts of methane and nitrogen are present. The hydrogen content measured in the downhole samples is at a high 11% (Table 15).

Table 15: Total gas content and gas composition of the downhole samples taken at MOL-GT-01.

	MOL-GT-01-3400m		MOL-GT-01-3280m	
	%vol	Nm ³ gas/Nm ³ _{liquid}	%vol	Nm ³ gas/Nm ³ _{liquid}
Nitrogen	2.38	0.061	4.01	0.096
Argon	0.07	0.002	0.07	0.002
Carbon dioxide	77.3	1.977	75.8	1.813
Methane & ethane	8.23	0.21	8.46	0.202
Helium	0.23	0.006	0.2	0.005
Hydrogen	11.7	0.3	11.4	0.274
Total gas content		2.556		2.392

Radionuclides

Table 16 gives the concentrations of radionuclides detected in the formation water. ²²⁶Ra is the most active radionuclide with an average activity of 86.4 Bq/l. The activity of ²²⁸Ra is between 10 and 20 Bq/l. The ⁴⁰K concentration is about 80 Bq/l. The activity of the other radionuclides is low (see also Vasile et al., 2017).

The radioactivity concentrations of ²¹⁰Pb and ²¹⁰Po in the formation water were found to be low. In contrast, high ²¹⁰Po and ²¹⁰Pb activities were measured in scaling recovered from the heat exchangers

in July 2019 (). This can be explained by radioactive decay of ^{226}Ra in combination with the temperature drop in the heat exchangers. The latter cause Pb to precipitate (Pauwels et al., 2021).

The high Ra-activity is a result of complexation of radium by the chlorine in the brine. The Ra-isotopes are decay products of ^{238}U and ^{232}Th . The spectral GR shows that U and Th are enriched at the top of the CLG: up to 30 ppm of U and 17 ppm of Th is recorded in the black shales. In the Goerée Formation and at selected intervals in the Loenhout Formation elevated U (up to 25 ppm) and Th (up to 20 ppm) are recorded as well. U and Th are not easily mobilised under de reducing reservoir conditions, but the radium daughter isotopes readily dissolve in the chlorine-rich formation water.

Table 16: Average concentrations of radionuclides in the formation water sampled at MOL-GT-01. Uncertainty is given as expanded uncertainty ($k = 2$) (a.: data from Vasile et al., 2017)

	concentration (Bq/l)	
	average concentration	uncertainty
^{226}Ra	86.36	22.05
^{228}Ra	11.80	8.62
^{210}Pb	0.039	0.033
^{210}Po (a)	0.036	0.007
^{234}U	0.0012	0.0003
^{235}U	< 0.18	-
^{238}U	0.00085	0.00028
^{228}Th (a)	0.360	0.07
^{40}K	82	11

Temperature model

The thermal model for the Balmatt site is based on temperature measurements on MOL-GT-03 conducted in February 2021. The temperature log shows an average geothermal gradient of 0.029°C/m over the Cenozoic and Cretaceous sediments. The geothermal gradient over the Upper Carboniferous is 0.043°C/m. This high gradient is explained by the high clay content and the presence of coal, which results in an overall low thermal conductivity. In the Lower Carboniferous limestone formations, the geothermal gradient drops again to 0.021°C/m on average.

The temperature log that was run in 2021 didn't reach the bottom of the Lower Carboniferous Limestone Group. To get an idea about the rock temperature for deeper formations, a 1D thermal model was build (Figure 10). The model takes into account conductive heat transport and heat generation. The set-up of the model is described in Broothaers et al., 2020. Values for the thermal conductivity and heat production of the different formations were derived from well logs (see above). A surface heat flow of 0.058 +/- 0.003 W/m², and a surface temperature of 11°C was assumed. These figures correspond to the average values derived from temperature logs in Flanders (Broothaers et al., 2020).

The model predicts a temperature at the top of the reservoir (3100 m) of $130 \pm 6^\circ\text{C}$. At the bottom of the bottom of the Lower Carboniferous (bottom of the Bosscheveld formation; 4082 m) the estimated temperature is $151 \pm 7^\circ\text{C}$.

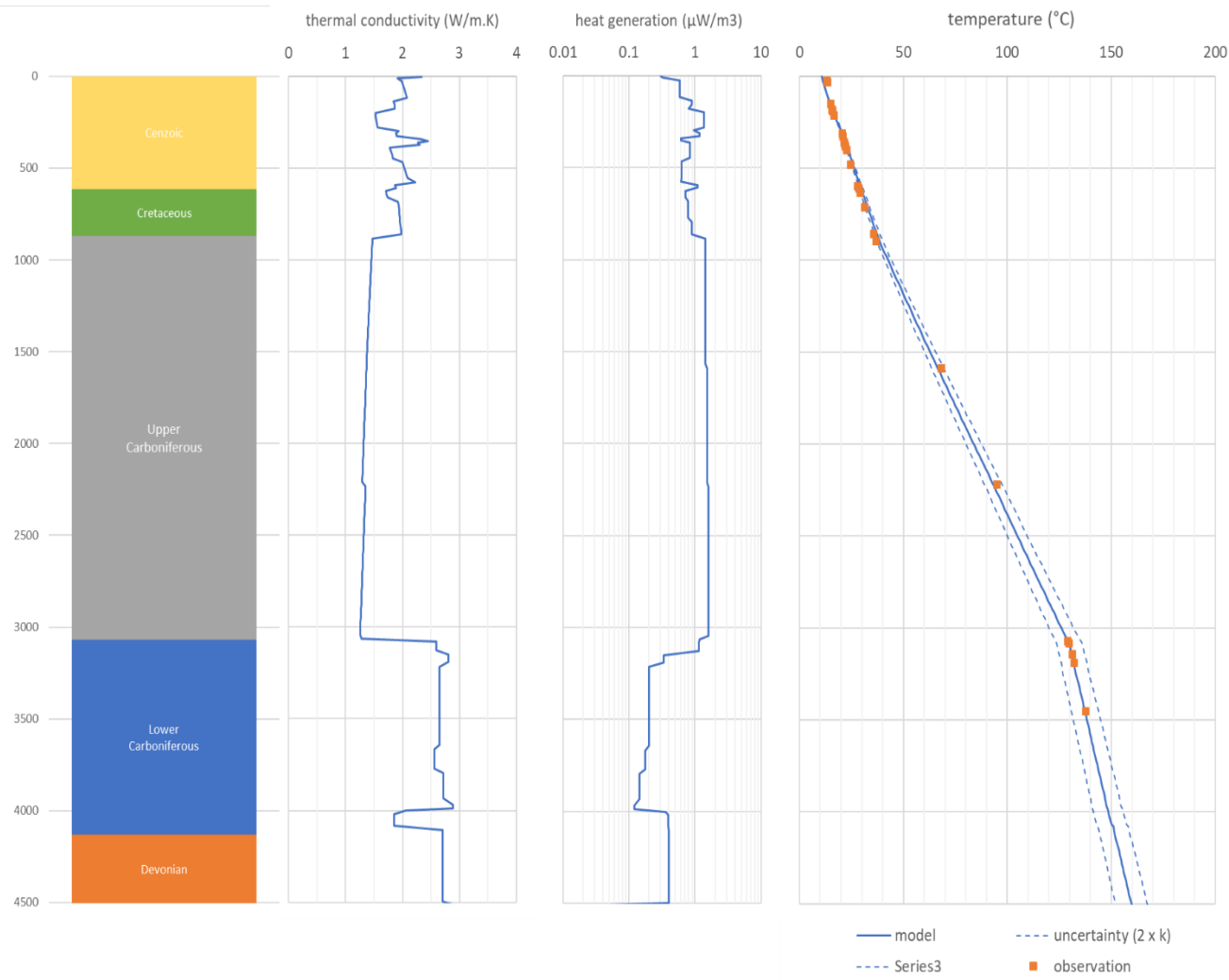


Figure 10: Temperature model for the Balmatt geothermal site based on data from MOL-GT-03)

Knowledge gaps

From a geological point of view, the main knowledge gaps are:

- Processes that control induced seismicity at the Balmatt geothermal site are not fully understood. Research is going to focus on the scientific key questions that are strongly linked to seismic hazard assessment at the Balmatt geothermal site. The research is divided into 2 fields of analysis: seismic data analysis, and geo-mechanic modelling. It should provide input to assess the technical-economic viability of a deep geothermal energy production as Balmatt, and lead to a better understanding of the mechanisms underlying induced earthquakes. It is intended to advance the development of next generation adaptive traffic light systems for deep geothermal.
- The geological model of the Balmatt geothermal site is mainly based on 2D seismic data. The resolution of the 2D data does not allow detection of fault systems with a small vertical throw. Moreover, it is hard to deduce the conclusive structure framework from it. A 3D seismic survey could help to build a more accurate geological model.

Past/Current/future above ground energy system

The geothermal loop at the geothermal plant of VITO in Mol, Belgium consists of the following components: Inhibitor lines against corrosion and scaling, electric submersible pump, gas-and-particle separator, heat exchangers, gas injection column, filter units, injection pumps. The flow in the geothermal loop is kept as constant as possible during operation and the system pressure is kept above bubble point to avoid degassing. A simplified schematic of the Balmatt geothermal loop is shown in Figure 11. A schematic drawing of the full plant is shown in Figure 12.

Gas and particle separator

When the brine reaches the surface, it is first passed through a separation tank where the flow rate is slowed to allow free gas bubbles to rise to the top of the tank and fine suspended particles to sink to the bottom. The separator can be bypassed for cleaning if necessary. Gas that separated at this point flows to gas injection column.

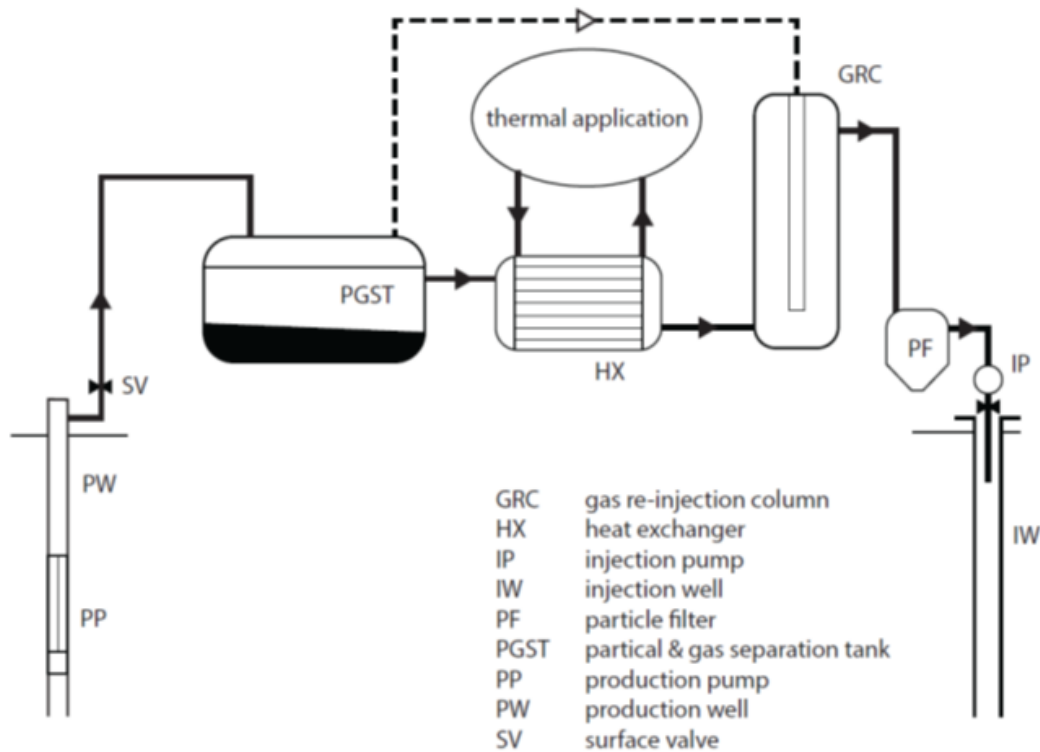


Figure 11: Geothermal Loop of the Balmatt plant

Heat exchangers

There are currently two identical heat exchangers (shell-and-tube) installed in series. One of the two heat exchangers can always be taken out of service for maintenance. Bypass pipes are installed for this purpose. The heat exchanger consists of 2 x 3 one-pass shell-and-tube heat exchanger packages, coupled in series to form one continuous heat exchanger unit. They are designed for a flow rate of 140 m³/h. The brine flows through the tubes. The heat exchangers have the following specifications:

- Capacity: 2 x 3300 kW
- Shell: heats water from 60°C to 114°C
- Tubes: cools the brine from the intake temperature to 65°C.

Originally the plant was designed as a combined heat & power geothermal plant, by including a demonstration ORC as presented in Figure 12. However, this ORC unit has become obsolete and will not be considered in the future for the Balmatt plant.

Gas re-injection and gas discharge

An aeration tank is installed just before the filter units to dissolve gasses that were separated from the brine (in the gas and particle separator or the heat exchangers) back into the brine. Gasses that cannot be dissolved in the brine (due to slow dissolution kinetics) are discharged through a silencer and chimney.

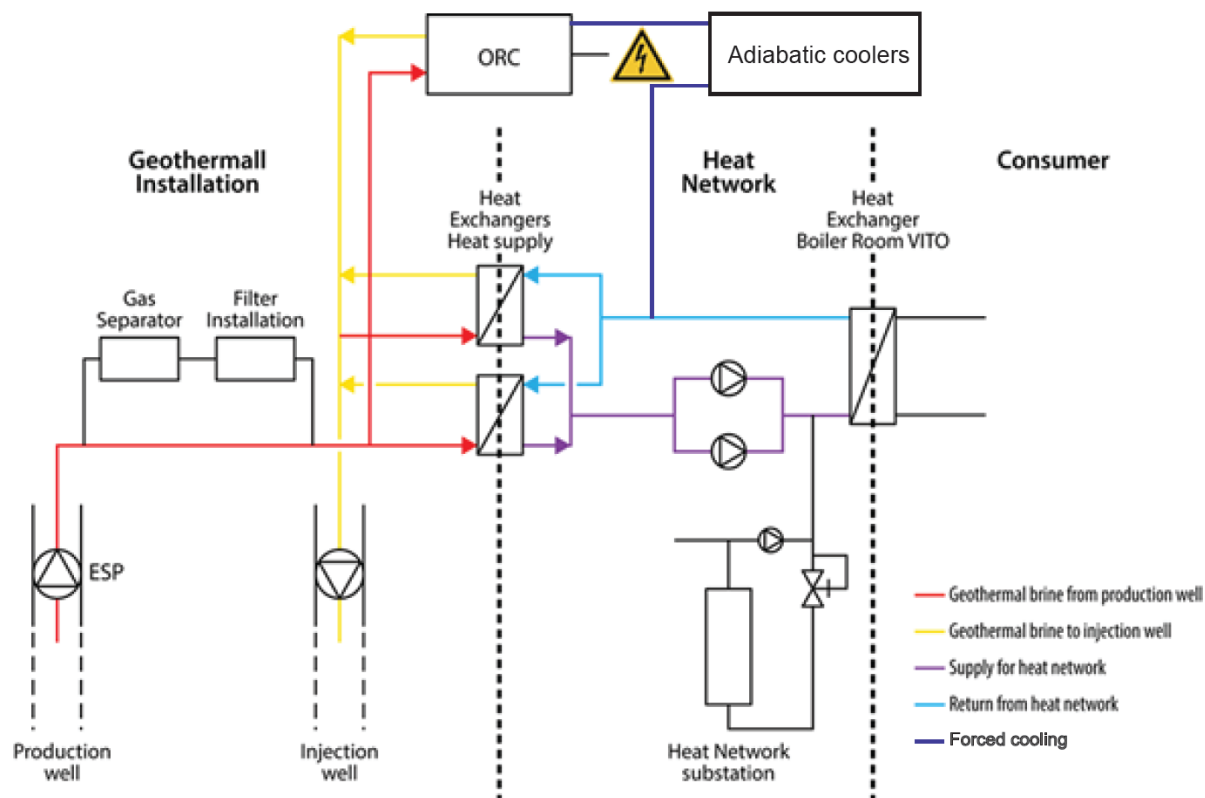


Figure 12: Schematic drawing of the Balmatt combined heat & power geothermal plant

Filter units

The purpose of the filter units is to remove suspended solids before the brine is reinjected. During normal production, the brine is routed to three parallel units, one of which is online and two are offline for cleaning or standby. The pressure upstream and downstream of the filter block is constantly monitored. Cleaning is required when the differential pressure is higher than the set parameter (e.g., 0.60 bar).

Injection pumps

These pumps were installed to inject the cooled geothermal brine back into the geothermal reservoir. The injection pressure at a flow rate of 30 m³/h is around 70 bar. Vito tries to operate the plant at a maximal injection pressure of around 80 bar. The pumps are switched on when the necessary injection pressure exceeds 47.5 Bar. The minimum flow rate is approximately 30m³/h.

Use of the geothermal heat

The Balmatt geothermal plant is connected to the district heating network of the research campus of VITO and SCKOCEN in Mol (Figure 13). The campus is situated at a distance of 1.8 km of the geothermal power plant. The buildings on the campus (office buildings + laboratories) are interconnected with a local heating grid. Heat is currently provided with three non-condensing gas boilers with a total installed capacity of 21 MW. Total gas consumption is measured on an hourly basis. The gas consumption can be converted to heat injected in the heating grid through the thermal efficiencies of the gas boilers, which is 82%. The average annual heat demand of the heating grid over the last three years equals 25 GWh per year. There is no clear trend towards an increasing or decreasing heat demand on the research campus.

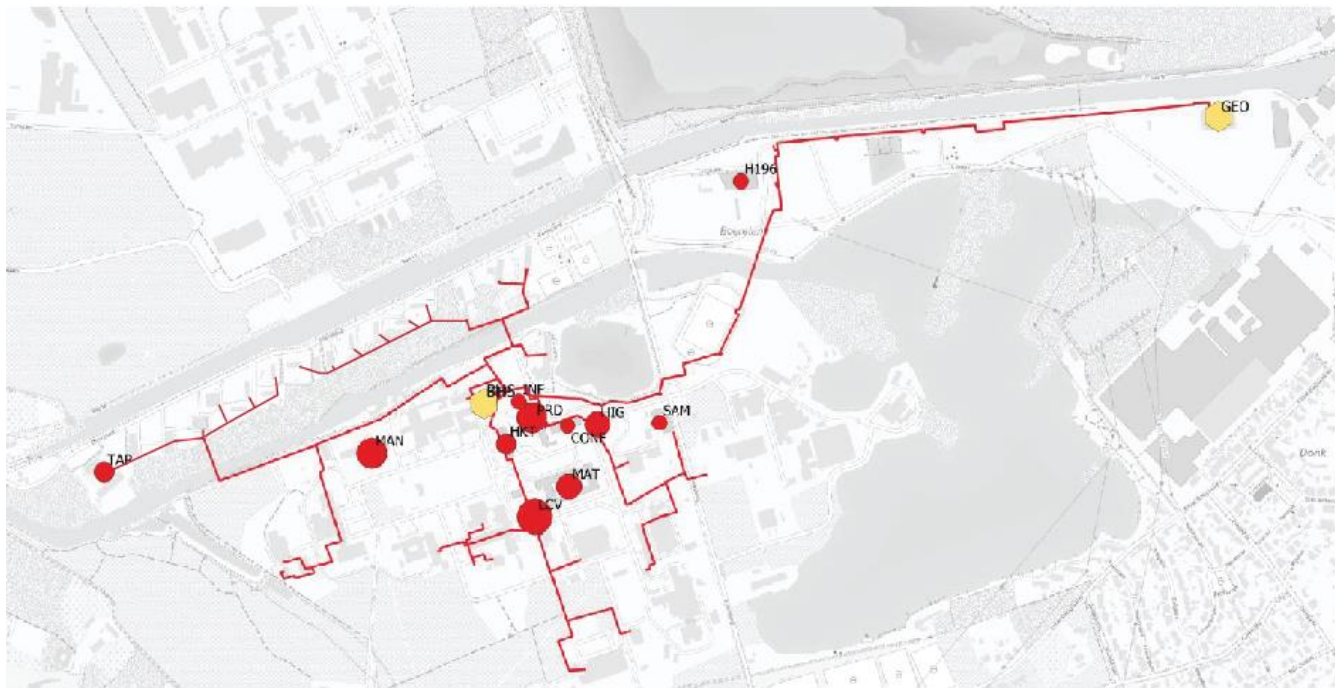


Figure 13: Layout of the existing district heating network at the research campus of VITO and SCKOCEN. The two yellow dots are GEO: Balmatt geothermal plant, BHS: boiler house.

The temperature regime of the heating grid has a seasonal dependency. It varies between 95°C/80°C at -10°C ambient air temperature and 65°C/60°C at 20°C ambient air temperature. During testing of the geothermal heat supply, lower return temperature was realised however: the injection temperature fluctuated between 55 and 65°C during the winter season of 2021 – 2022.

The geothermal plant is connected to the boiler house of the district heating system through a 1.8 km long pipelines (one for supply and one for return). New developments are planned however along connecting pipes. The new office buildings and labs will require low supply temperatures for heating ($\leq 65^\circ\text{C}$ for labs, 45°C for office buildings). A few of the new buildings are already in use. The heat demand of the new developments is estimated to rise from 800 MWh/y to about 2,500 MWh/y over the period 2022 – 2030 and to about 3,450 MWh/y by 2040. The buildings also have a cooling demand, that is estimated at 2,250 MWh/y in 2030 and 3,200 MWh/y in 2040.

Description and Schematic overview on different integration options of the HOCLOOP

The pilot project using the HOCLOOP technology will make use of well MOL-GT-03. The intention is to provide geothermal heat to both the existing heating network and to the new developments that are planned in the area. 3 basic integration options are considered (Figure 14). In the presented schemes,

the HOCLOOP technology will either provide heat to the existing geothermal system or to a new cold-and-heat network. More options can be defined to link the existing geothermal system with the cold-heat network.

In scheme a.) the HOCLOOP technology will be used to pre-heat the return flow that comes from the boiler house, before it enters the heat exchanger of the existing geothermal plant. In case the heat demand on the network can be covered by the HOCLOOP, the geothermal plant can be bypassed. This can be the case during most of the summertime, allowing the existing geothermal plant to be shut down. Periodic shutdown of the geothermal loop between wells MOL-GT-01 and MOL-GT-02 may help to reduce the seismic risk at the Balmatt geothermal site.

In this scheme, a new heat exchanger and control valve will be installed on the return pipe that connects the boiler house with the Balmatt geothermal plant.

The pros of this scheme are:

- Increase of the thermal power of the Balmatt geothermal plant without having to increase the flow rate between wells MOL-GT-01 and MOL-GT-02,
- Less cooling of the geothermal brine in the existing geothermal loop may help to reduce the seismic risk,
- Periodic shutdown of the geothermal loop between MOL-GT-01 and MOL-GT-02 that may help to reduce the seismic risk,
- Easy integration in the existing geothermal heating system.

The contras of this scheme are:

- Higher return temperature will result in a less cooling of the geothermal brine and hence lower thermal output of the existing geothermal loop,
- High injection temperature in the HOCLOOP will result in a lower thermal output of the system.

In scheme b.) the HOCLOOP technology will be used to provide low temperature heat to a newly build cold-and-heat network that serves the new development near the Balmatt geothermal site. Cooling will be provided using an air-water heat pump with heat recuperation. In this scheme, no connection is foreseen with the existing geothermal loop. Such a connection may be considering in case the HOCLOOP cannot provide sufficient power. As an alternative, thermal storage can be considered to deal with peak demands.

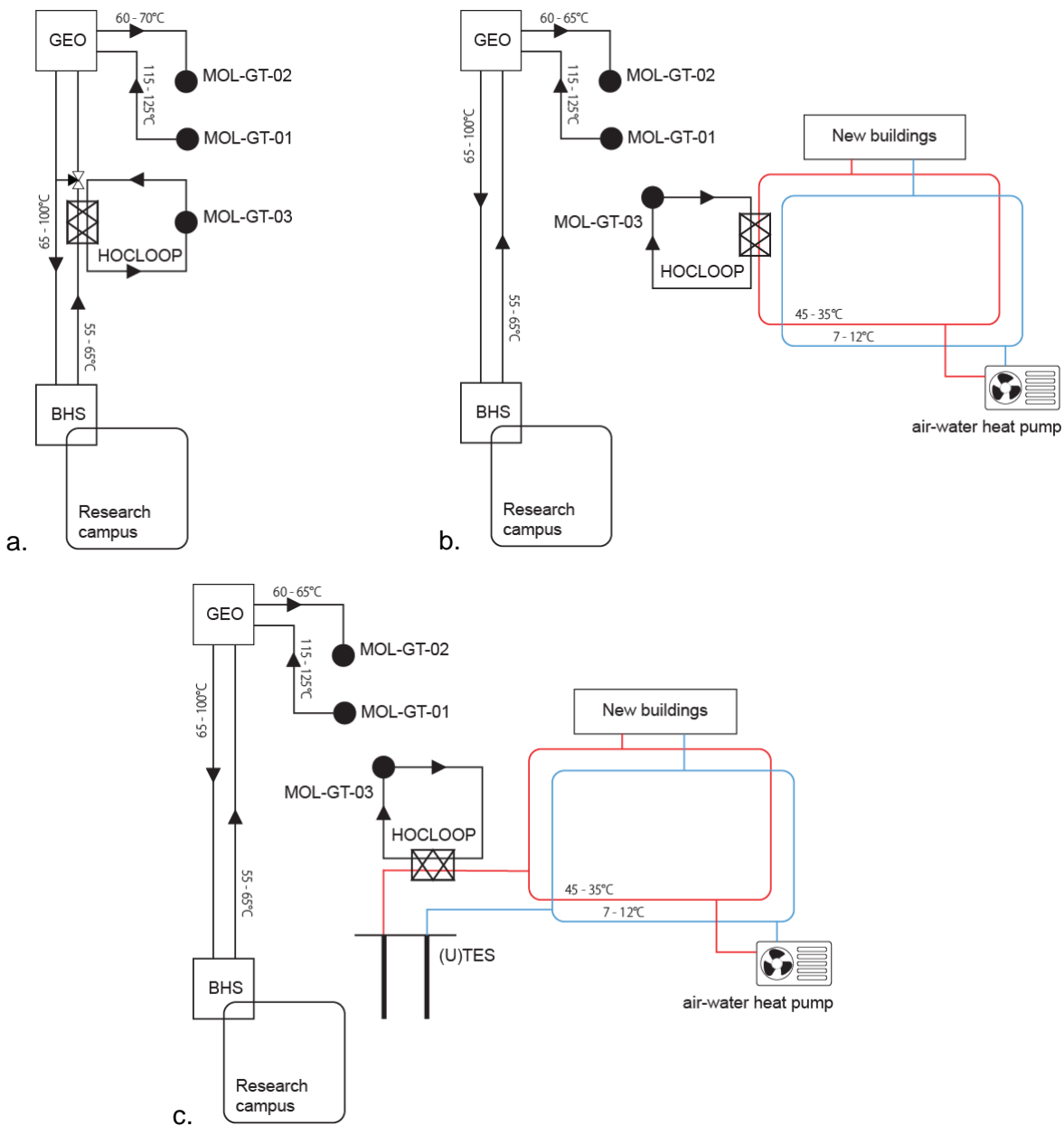


Figure 14: Integration options for the HOCLOOP technology at the Balmatt geothermal site. a.) Integration in the existing geothermal district heating system; b.) as a heat source in for a new cold and heat net for the new developments; c.) as a heat source in for a new cold and heat net for the new developments in combination with thermal energy storage.

The pros of this scheme are:

- The injection temperature of about 35°C is positive for the thermal output of the HOCLOOP,
- Optimisation of the system is possible both at the side of the HOCLOOP and of the cold-and-heat network, including thermal energy storage (e.g., tank storage, UTES),
- Energy exchange between buildings.

The contras of this scheme are:

- Investment in the cold-and-heat network needed (double pipe and central heating plant),
- Cooling is 100% provided by the heat pump.

In scheme c.) the HOCLOOP technology will be used to heat the water that comes from an underground thermal storage (UTES). The UTES will provide cooling during the summer, and at the same time store heat for the winter season. In addition, the UTES can be charged with heat from the HOCLOOP to deal with higher demands during wintertime. When the cooling demand exceeds the cooling output of the UTES, an air-water heat pump with heat recuperation is foreseen. No connection is foreseen with the existing geothermal loop. Such a connection may be considered in case the HOCLOOP cannot provide sufficient power. As an alternative, an extra water-water heat pump or gas boiler can be installed to deal with peak heat demand.

The pros of this scheme are:

- The injection temperature of about 35°C is positive for the thermal output of the HOCLOOP,
- More thermal energy can be produced from the HOCLOOP in combination with UTES
- Optimisation of the system is possible both at the side of the HOCLOOP and of the cold-and-heat network, including thermal energy storage (e.g., tank storage, UTES),
- Energy exchange between buildings.

The contras of this scheme are:

- Investment in the cold-and-heat network needed (double pipe and central heating plant),
- Investment in the UTES system (drilling of the wells).

Technical challenges

Induced seismicity

A major challenge for the geothermal operations at Balmatt is induced seismicity. Seismicity was first detected during the test phase of drilling MOL-GT-02 in September 2016. The recordings were made by borehole seismometers managed by the Royal Observatory of Belgium. In 2018, this led to the installation of a seismic measurement network consisting of seven borehole stations and the setting up of a traffic light system.

Several earthquakes were detected during the start-up phase of the geothermal plant between the end of 2018 and mid-2019. The strongest quake occurred on June 23, 2019. It had a magnitude of M_L 2.2. The earthquake was felt in parts of the municipalities of Mol, Dessel and Retie. It happened after the longest test period, but also three days after operations were abruptly interrupted due to a failure on the medium-voltage grid. The operations were suspended, and study was performed to identify the processes that lead to the induced seismic events as Balmatt (Kinscher et al., 2023).

In April 2021, the production was resumed to extend the seismic, and to collect additional information about the relationship between the plants' operations and seismic activity. After a second seismic event that was felt in the vicinity of Balmatt on November 16, 2022, the operations have been suspended again. The earthquake had a magnitude of M_L 2.1.

Based on the current understanding, seismicity seems to occur along a pre-existing fracture zone oriented parallel to the direction of the maximum horizontal stress SH ($\sim N340^\circ$) that is dominated by conjugated strike-slip faulting oriented NNW-SSE and WNW-ESE (Kinscher et al., 2023). Both pressure and cooling induced stress changes seem to control the seismic activity at the Balmatt geothermal site.

Naturally occurring radioactive material (NORM)

The occurrence of radioactive elements in the formation water of the Lower Carboniferous Limestone Group has been reported by Vandenberghe et al. (2000). The brine produced from MOL-GT-01 contains naturally occurring radioactive substances. Analysis of radioactive elements in the brine indicate an

activity of 95 to 110 Bq/l for ^{226}Ra , and about 8.5 Bq/l for ^{228}Ra (Vasile et al., 2017). Consequently, monitoring of the radiation level had to be installed, and protocols have been implemented for routine activities that pose of risk of exposure to NORM.

For activities that pose a risk to exposure and that are not covered by the protocols that are in place, the supervisory authorities (Federal Agency for Nuclear Control – FANC) must be informed and permits are required. Moreover, the activity of tools that come in contact with the brine must be measured before and after they have been used. Only clean tools can be allowed on site. In case the radiation exceeds the norm, the tools have to be cleaned before they can be shipped from the site.

People who may come into contact with the brine, scales or any component that may be contaminated with NORM should follow procedures and wear protective equipment when performing their duties. Waste must also be disposed of in accordance with regulations.

Corrosion

The corrosion risks are high for all components that come into contact with the formation fluid. This is due to:

- The high mineralization of the geothermal fluid; more precisely high concentrations of chlorides can induce pitting corrosion,
- The temperature of the fluid,
- The presence of dissolved gases rich in CO₂, which can cause uniform corrosion,
- The partial pressure variation possibilities,
- The potential presence of sulphides, which can cause cracking corrosion,
- The formation of scales that can lead to localized attack.

Moreover, high heavy metals contents, oxidation possibilities and cooling are aggravating factors of corrosion processes. The risks of pitting and crevice corrosion as well as stress corrosion cracking must be considered in the design and material selection for well completion and surface installations.

Combining materials of different grades for subsurface parts that come into contact with the formation fluid should be avoided, as this will lead to galvanic corrosion phenomenon. Generally, the least noble alloy will corrode.

Economic aspects

VITO is operating the boiler house of the existing district heating network and will be responsible for the energy supply to the new building that are planned on the old industrial grounds near Balmatt. Prices for electricity and natural gas vary according to the SPOT-market (Belgium).

Economic analyses will be done by comparison of the annual costs for heating and cooling for the integration options shown in Figure 14, with the heating and cooling costs based on gas boilers for the existing heating network and reversible air-to-water heat pumps for the new buildings.

Summary table

Parameter	Value	Unit
Geological information		
Top reservoir Depth	3100	m
Thickness of the reservoir	760	m
Temperature at the top of the reservoir	130	°C
Type of reservoir (homogeneous, fractured/fissured)	Fractured	
If fractured, fracture distribution type	-	

Hydraulic properties		
Permeability of the reservoir	$10^{-16} - 10^{-14}$	m ²
Matrix porosity	< 1 – 4	%
Regional flow	Unknown***	
Thermal properties		
Thermal conductivity (in reservoir) – average value at 140°C	2.68	W/m.K
Thermal conductivity(ies) above	2.6 – 2.8	W/m.K
Geothermal gradient(s) up to the top reservoir	32.5	°C/km
Thermal Capacity (reservoir rock) – average value at 140°C	0.93	J/g/K
Geothermal loop		
Extraction well depth (MOL-GT-01)	3610	m
Injection well 1 depth (MOL-GT-02)	3830	m
Injection well 2 depth (MOL-GT-03)	4235	m
Brine extraction temperature*	125 – 115	°C
Brine extraction flow*	140* – 30**	m ³ /h
Brine reinjection temperature*	65	°C
Brine reinjection max temperature*	80	°C
Hot water loop		
Supply collector water temperature*	114	°C
Return collector water temperature*	60 – 70	°C
Supply and return collectors pipe size	DN400	-
Heat transportation network		
Supply temperature*	85 – 100	°C
return temperature*	72	°C
distribution pump flow rate	20 – 110	m ³ /h
distribution pump delivery pressure	5 – 6.6	barg
distribution pump discharge head	32 – 49	m
distribution pump NSPHa	21	m
pipe length to VITO boiler house	2	km
pipe diameter to VITO boiler house	DN250	-
VITO boiler house		
Gas boiler capacity*	7	MW _{th}
Gas boiler quantity	3	-
HTR/DHG heat exchanger capacity*	3.3	MW _{th}
HTR/DHG heat exchanger quantity	3	-
Emergency cooler		
Cold side inlet temperature*	30	°C
Cold side outlet temperature*	50	°C
Hot side inlet temperature	114 (124*)	°C
Hot side outlet temperature*	80	°C
Maximum cooling power*	9	MW _{th}

* Design conditions

** Operational conditions during the last test period

*** Strong regional groundwater flow is unlikely in the Lower Carboniferous reservoir due to low difference in head between the recharge zone and Balmatt

4.3 Case study Darmstadt, Germany

General description of the pilot site

Darmstadt offers excellent conditions for a potential future pilot site. There, three 750 m deep borehole heat exchangers had been built on the Lichtwiese Campus by 2023 to demonstrate the concept of a medium deep borehole thermal energy storage systems. This demonstration site is also integrated in several national and international research programs (BMWK funded 'SKEWS', EU-Horizon funded 'PUSH-IT' and EU-Interreg-funded 'DGE-Rollout'). Lichtwiese Campus geology consists of granodiorite of the Frankenstein Complex of the variscan Odenwald crystalline complex under a thin 3 m cover of Quarternary sediments. The basement upper part is characterized by a locally varying weathering zone that can reach a thickness of up to 40 m (Greifenhagen 2000). It consists of clay containing weathering products of the granodiorite, with monocrystalline and lithoclast grains whose granulometry ranges from sand to medium gravel. In the north, east and south of Lichtwiese Campus, coarse to fine-grained Permian sandstones and conglomerates unconformably, as well as basalts overlay the Variscan basement units. This geological context makes this site well suitable for the implementation of a closed loop geothermal system.

The Lichtwiese DHC system is the second largest sub-grid of TU Darmstadt's thermal energy system. The grid is supplied by a central cogeneration heat and power plant on Campus Lichtwiese and is connected to a public district heating (DH) grid. A total of 155,000 m² of heated floor area on campus are supplied with 22.6 GWh/a of heat and 8 GWh/a of cooling. The central plant provides heat and electricity to the university with three CHP units with a thermal power of 2 MW each and an additional one with a power of 3 MW. The units are operated to meet the campus' power demand and the residual thermal demand is satisfied by six gas peak boilers with 9.3 MW_{th} each. In contrast to the heating grid, which supplies the whole university, the cooling grid only supplies campus Lichtwiese by an absorption chiller of 1 MW_{th}, cooling. The planned decarbonization of the Campus Lichtwiese DHC network, the potential implementation of additional renewable energy sources, as e.g., solar thermal collectors or waste heat from high-performance computers leads to the Campus energy system being exceptionally well studied for example by the 'EnEff Stadt Campus Lichtwiese' I and II project, which aim to improve the Campus energy system. This well-known heating and cooling grid can be the basis for the simulation and optimization of suitable surface solutions for the distribution of generated power and electricity.

Geological conditions

Used data

Seismic campaigns

The two seismic profiles shown below in Figure 14 and 15 the geologic structure at the Lichtwiese campus to a depth of up to 400 m, below which the seismic section is dominated by noise. The top of the seismic profiles is a reference level of 180 m above sea level. The profiles can be divided vertically into two units: an upper, more reflective part and a lower part with lower impedance contrasts. Both units show only a few continuously traceable reflector bands.

In profile 1, the northeastern area is characterized by two distinct reflectors. One at a depth of 40 m and one at a depth of 90 m. Both reflectors are affected by a crosscutting fault and are separated by an area without notable reflectors. Furthermore, several faults are suspected in the southwestern part of the profile, but their offset cannot be unambiguously determined because a clear correlation of the reflectors on both sides of the fault surface is not possible. A change in geological facies is not observable in the profile without a doubt.

Profile 2 also displays a lateral change in its structure. The southeastern area is characterized by comparatively long continuous, dipping reflectors, that are separated by small faults. The north-western part consists of comparatively noncontinuous reflectors.

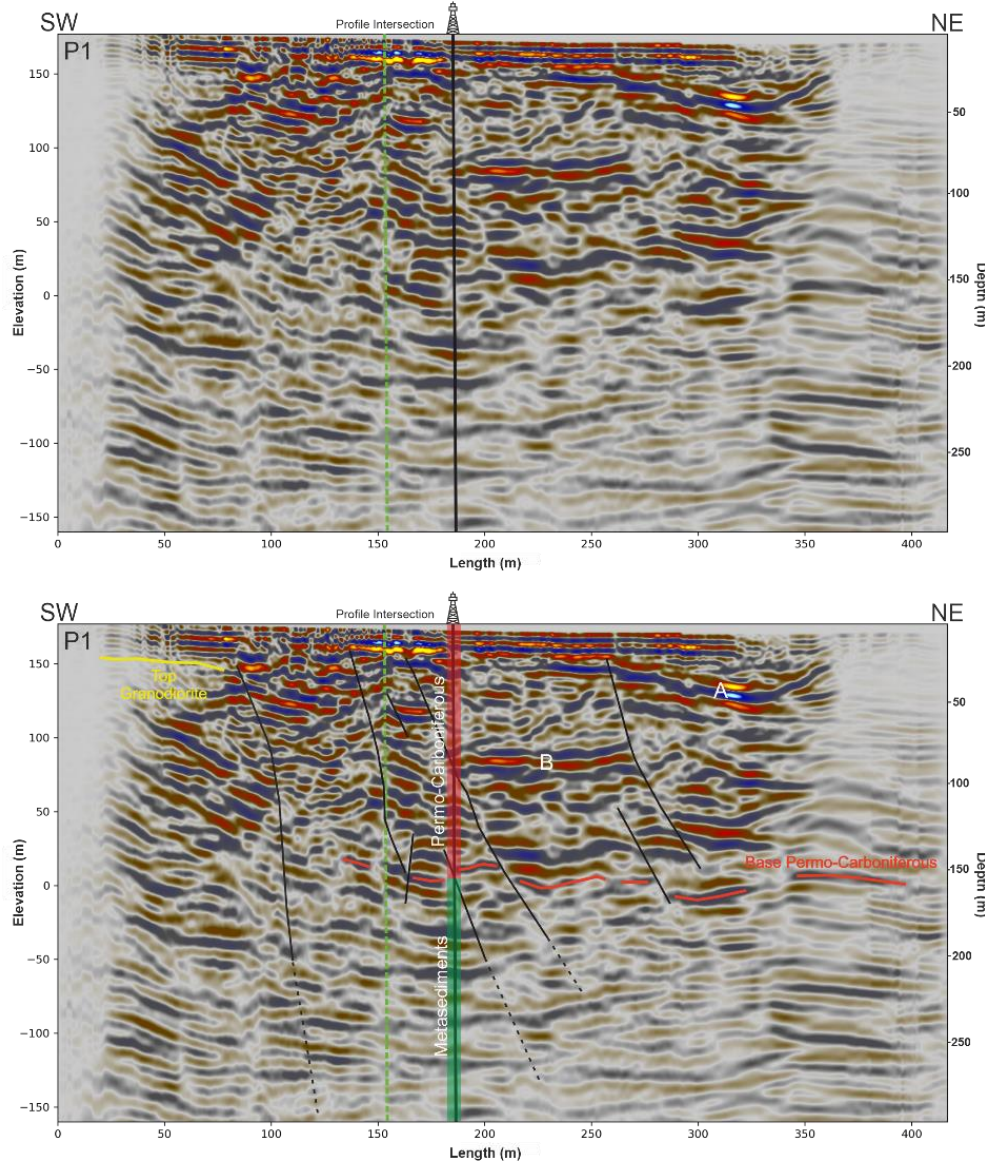


Figure 15: 2D seismic profile 1 (top) without interpretation and (bottom) without interpretation.

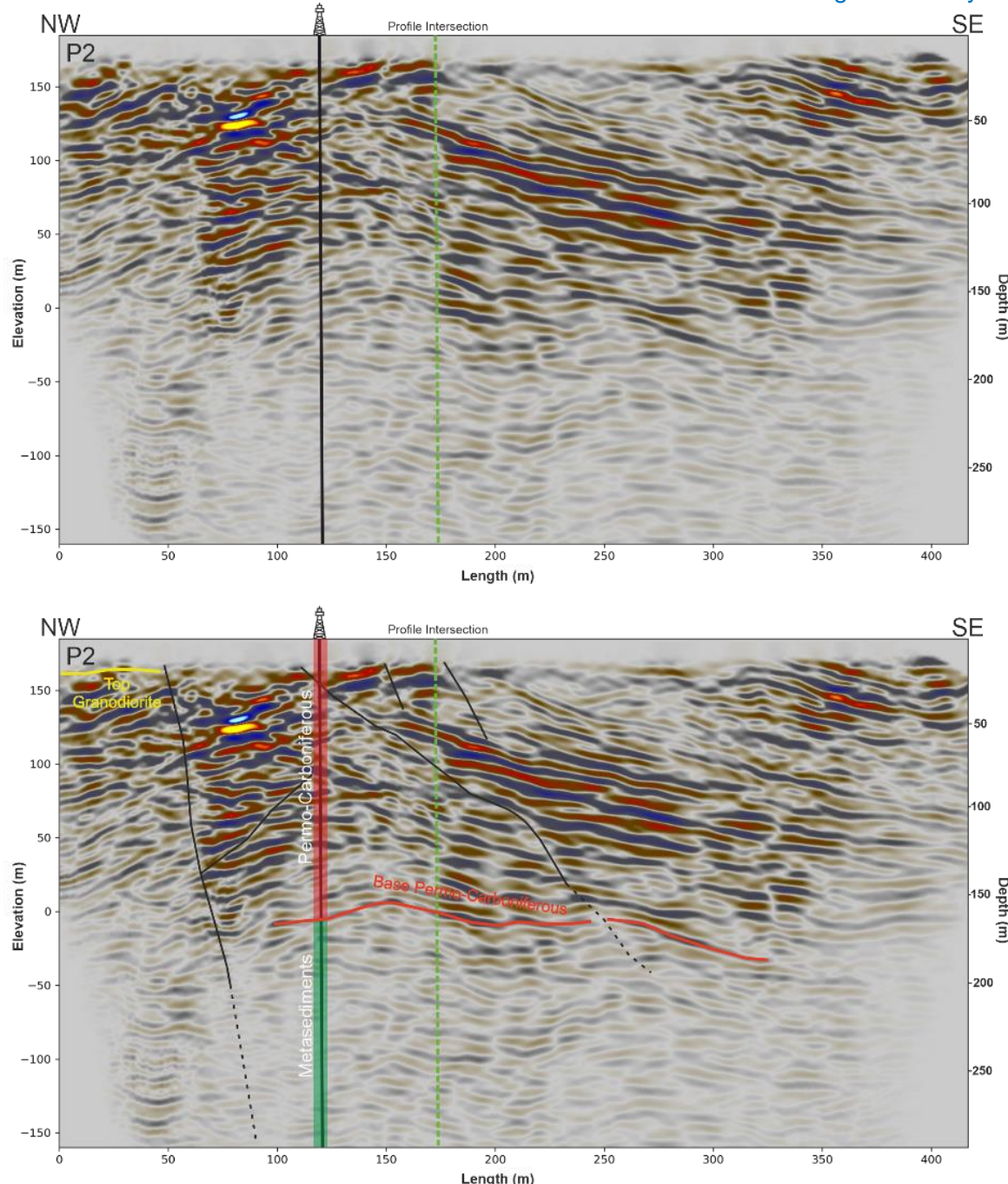


Figure 16: 2D seismic profile 2 (top) without interpretation and (bottom) without interpretation.

Electrical resistivity tomography

In January and March 2022, a total of 18 2D profiles were acquired as demonstrated in Figure 16. Four profiles were already measured in a previous study. The measurements were carried out with an ARES II automatic multi-electrode resistivity system by GF Instruments with a maximum of 92 electrodes with a spacing between 1 m and 3 m. The contact resistance was generally low-ranging from 300 to 800 Ω for most parts of the profiles yielding a generally good signal-to-noise ratio. In the profile segment located in forests with porous soils and high organic content, contact resistances up to 3000 Ω were measured.

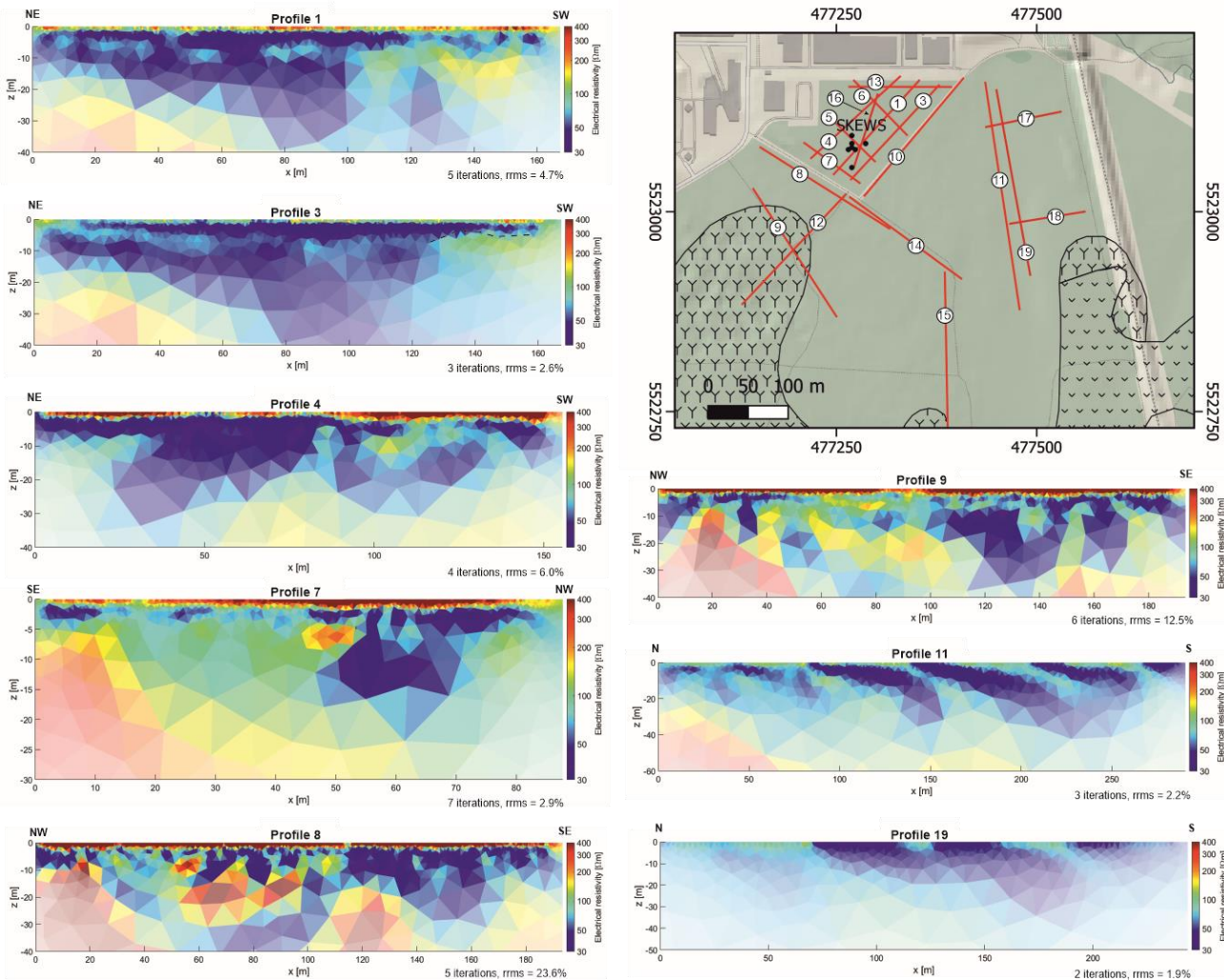


Figure 17: Geoelectric profiles of the Lichtwiese site.

Gravimetric profiles

Terrestrial gravimetry is a comparatively inexpensive and non-invasive method, that allows the detection of lateral density variations in the subsurface. Thus, lithological variations in basement rocks covered by Quaternary or older sediments can potentially be mapped. In February and March 2022, gravimetric data were acquired at 267 stations using the Scintrex CG-6 Autograv gravimeter as shown in Figure 17. Along the seismic profiles, a point spacing of 10 m was used to obtain the gravity field with an appropriate resolution. At the storage site, areal measurements were performed with a spacing of 20 m. In the other parts of the Lichtwiese, the point spacing was about 25 to 150 m. Base measurements were taken three times per day to record the instrument drift.

Since the Bouguer anomalies at Lichtwiese Campus are dominated by long-wavelength signals from several kilometer-deep crustal regions, several filters were used to enhance the short-wavelength component of the gravity field and to detect the boundaries of near-surface geologic units. First, the regional trend in the gravity signal was removed using a high-pass filter with a cutoff wavelength of 1000 m. In addition, the vertical gradient of the Bouguer anomalies (G_{zz}) was calculated, which also behaves like a high-pass filter that concentrates the signal above the source. With the total horizontal gradient (G_{horiz}) lateral variations in the gravity field can be amplified allowing the edges of the source bodies to be detected. Finally, the so-called gradient derivative (G_{tilt}) was calculated, which normalizes the G_{zz}

with Ghoriz. This amplifies particularly small amplitudes without disturbing the signal's polarity. Maxima and minima of Gtilt are concentrated over the source bodies, and the zero crossing marks the edges.

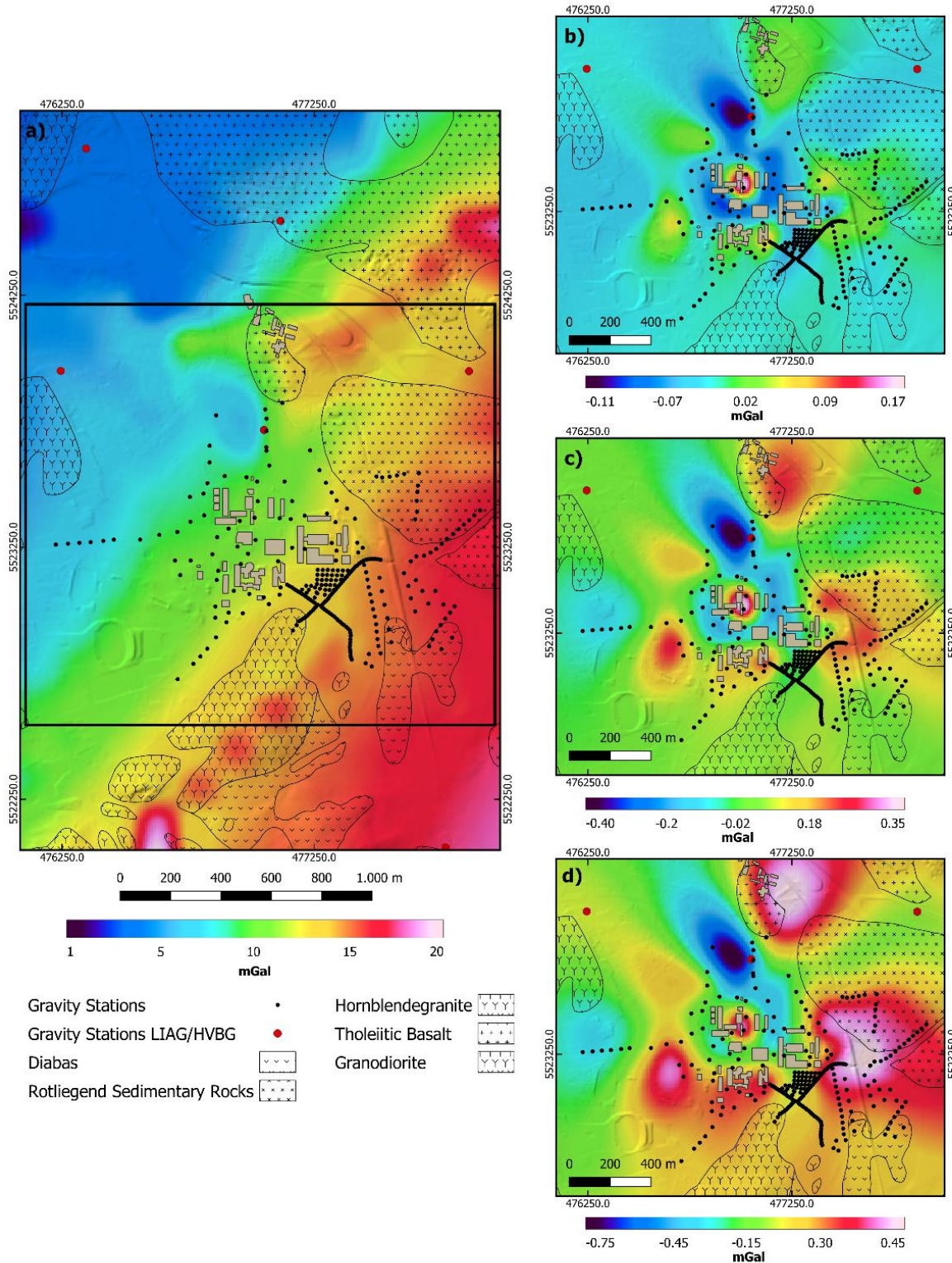


Figure 18: Gravimetry profile of the Lichtwiese site.

Geological setting

The Lichtwiese project site is located in the southeast of Darmstadt, Hessen, Germany. The main eastern fault of the Upper Rhine Graben which divides the city is the main geological feature of this site (see Figure 15) (Seib et al. 2022).

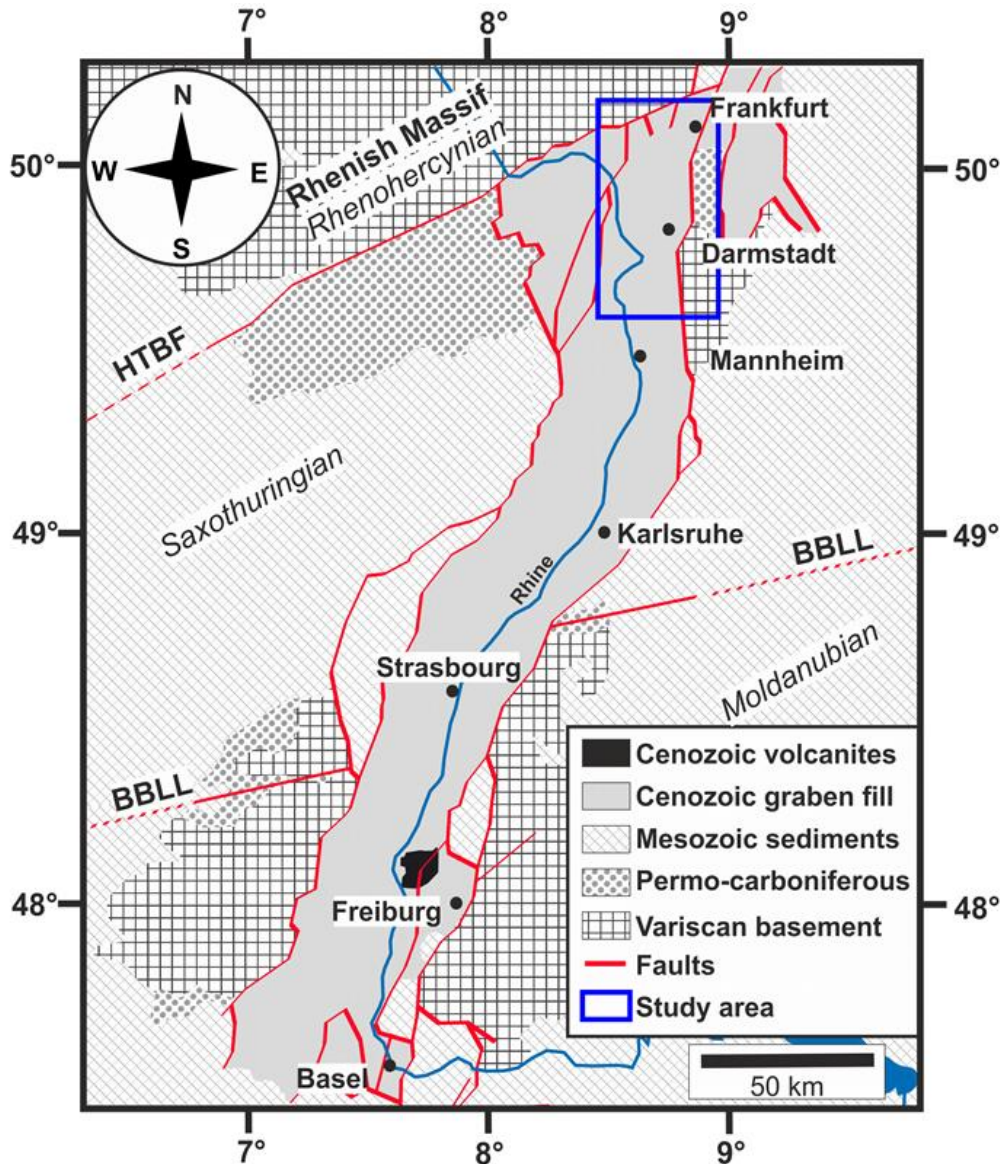


Figure 19: Upper Rhine Graben geological setting.

The local structural setting

The eastern part of the site is fracture controlled igneous, volcanic and sedimentary rocks of the Odenwald and Sprendlinger Horst (Klemm, 1911; Greifenhagen, 2000). The Odenwald crystalline complex is the largest outcrop massif of the Mid-German crystalline high and belongs to the northern margin of the variscan orogen. The Frankenstein complex's northernmost unit consists of pyroxene, hornblende, and olivine gabbros and diorites on the southern margin. Its northern part underlying the city of Darmstadt and the so-called Sprendlinger Horst is built of paragneiss, granodiorite and granite (Dorr and Stein 2019; Stein 2001; Mezger et al. 2013). During the late Carboniferous and Permian, crustal extension

led to the establishment of several intramountainous basins, later filled with sediments in arid climates in the area of the Sprendlinger Horst (Greifenhagen 2000; Aretz et al. 2016). The resulting conglomerates, claystones and sandstones of the sedimentary cover of the Sprendlinger Horst are locally interbedded with basalts as a product of permo-carboniferous volcanism (Al-Malabeh and Kempe 2009). During the Cenozoic the regional geology was affected by the opening of the Upper Rhine Graben (Schumacher 2002; Derer et al. 2005) and associated volcanic activity (Mezger et al. 2013).

The western part of Lichtwiese Campus consists of granodiorite of the Frankenstein Complex under a thin 2–6 m cover of quaternary sediments. The upper basement is characterized by a weathering zone with a variable depth of up to 40 m (Greifenhagen 2000). Locally, this zone might be even thicker, which became evident by the drillings. It is composed by the weathering products of granodiorite, with monocrystalline and lithoclast grains whose granulometry ranges from sand to medium gravel size. In the North, East and South of Lichtwiese Campus, coarse to fine-grained sands originating from weathered Permian redbeds unconformably overlay the Variscan basement units. Previous research suggests the interpretation of the North–South oriented boundary separating the granodiorites from the Permian as a fault zone (Fahlbusch 1975, 1980; Klemm 1938; Kempe et al. 2001; Lang et al. 2011; Backhaus 1965). This fault or a similar one was hit by the first of four BHE drillings recently.

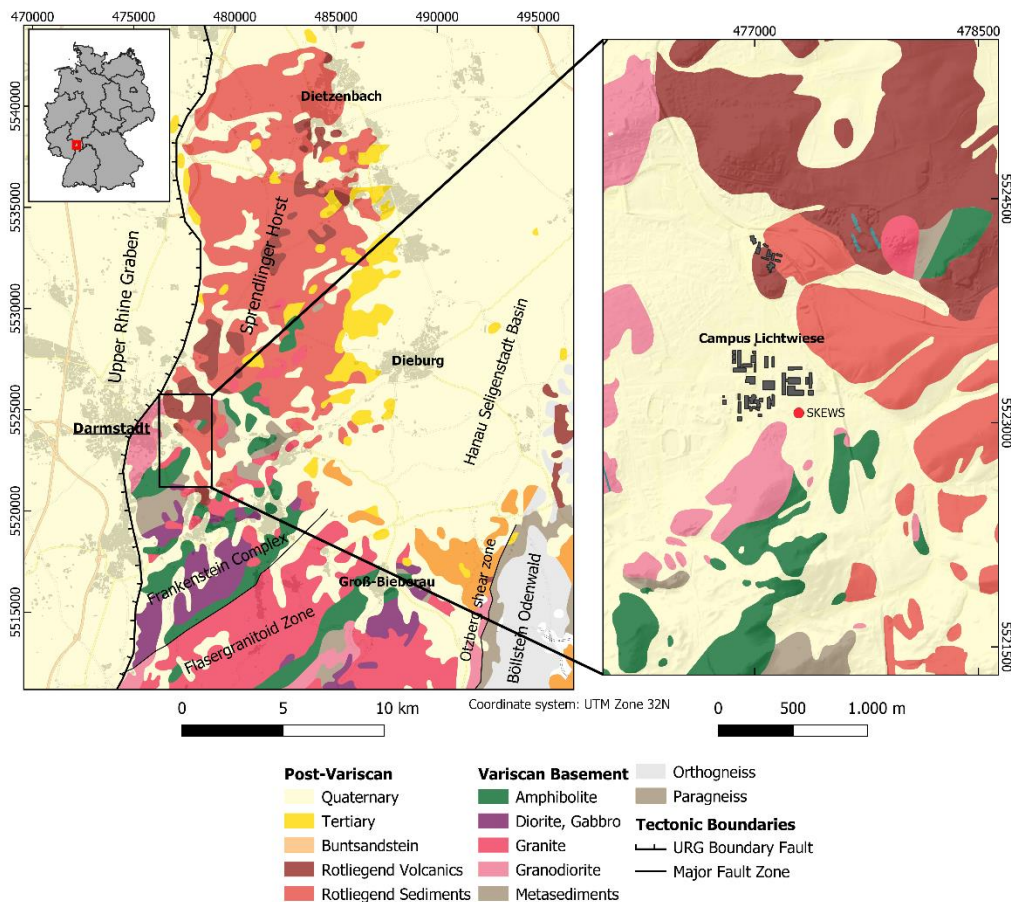


Figure 20: Geological overview of the Sprendlinger Horst and northern Odenwald (Modified after Guek300 Hessen, HLNUG, 2007 and Seib et al. 2022).

Description of the geothermal target

The Table 17 provide information about essential thermal and mechanical properties of the target formations for the HOCLOOP system.

Table 17: Thermal and mechanical properties of the target formations for the HOCLOOP system at TU Darmstadt

Parameter	Quaternary	Rotliegend Basalt	Dieburg Granite	Darmstadt Granodiorite
Depth (below surface)	0-5	5-200	200-475	475-750
Volumetric heat capacity (MJ/m ³ /K)	1.45	1.65	2.12	2.16
Thermal conductivity (W/m/K)	1.4	2.71	2.71	2.64
Porosity	0.17	0.05	0.03	0.03
Hydraulic conductivity (m/s)	3.7e-4	6.5e-6	4e-8	4e-8
Density		2.75	2.65	2.65
Poisson's ratio			0.25	0.25
Young's modulus			44.8	44.8
Temperature gradient	21°C/km	21°C/km	21°C/km	21°C/km

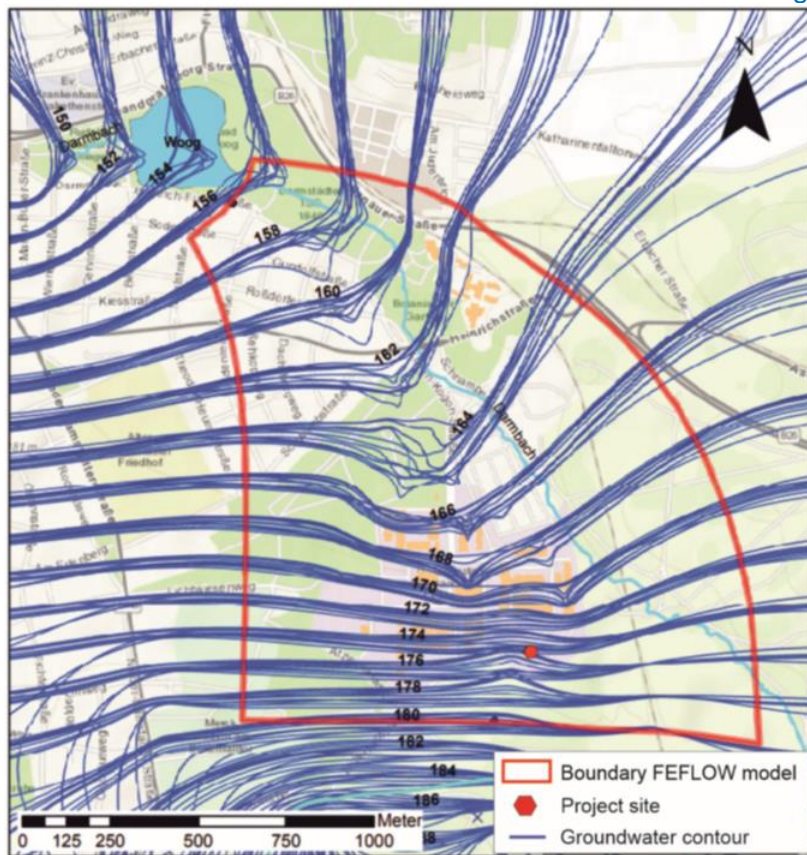


Figure 21: Average groundwater contour lines for each month for the period 2000–2020. In red the FEFLOW model boundary, derived from the groundwater flow direction is shown.

The near surface groundwater has a south–north direction of flow, which deviates to the west at the North of Campus Lichtwiese towards the URG (Figure 21). The depth of the phreatic surface displays an average of approx. 5 m below surface. Groundwater recharge of 170 mm per year is considered for the top of the geological site considering an approximate degree of artificial soil sealing of 10% at the Lichtwiese campus (Beier 2008). Hydraulic conductivity parameters for the sedimentary units and the granodiorite weathering zone are available from pumping tests at the project site. The hydraulic conductivity for the basement shown in Table 17 is based on the formation permeability data for crystalline rocks (Stober and Bucher 2007).

The temperature at 1000 m depth is approximately 50 °C (Ruehaak et al. 2012) corresponding to a geothermal gradient of 4 °C per 100 m. For the surface temperature, the average temperature in Darmstadt for the years 1981 to 2010 of 10.1 °C is applicable. The thermophysical rock properties (see Table 17) for the different geological units can be derived from the outcrop analog studies of regional outcrops (Bär et al. 2019; Weinert et al. 2020).

Knowledge gaps

Actions to fill gaps in available data/knowledge about the geothermal target are:

- Finalize the geological model,
- Update the groundwater model-define aquifer connectivity,
- Acquire petrophysical parameters for units without sufficient sample coverage (Permian basalts).

The work program to fill in crucial knowledge gaps and to (further) explore the geothermal potential exists of:

- For a precise petrological characterisation of the encountered rock types, thin sections will be analysed beginning in February 2023, allowing a better integration of the encountered rock types into the regional geological context.
- Further, thermophysical rock properties and its behavior will be measured and characterized in the test phase from April 2023 onward during enhanced geothermal response test.

Past/Current/future above ground energy system

Figure 22 provides a simplified schematic of the BTES installation.

Generally, a gradual renovation of the old building stock at campus Lichtwiese is envisaged for the next few years starting with the mechanical engineering facilities. This will include new windows and more efficient heating systems as well as new facade materials.

The plans for the plant that is under development include:

- Optimization of the design and operation of the generation facilities for heating, cooling and electric energy, including demand prediction, to make optimal use of thermal storage.
- Reduction of temperatures in district heating: Identification of errors in the design and control of district heating substations and in-building heat distribution, as well as development of metrics to determine where to apply which improvement measure to reduce network temperatures most efficiently.
- Integration of locally available waste heat into district heating, namely waste heat from data centres.
- Describe plant restrictions and operational conditions.

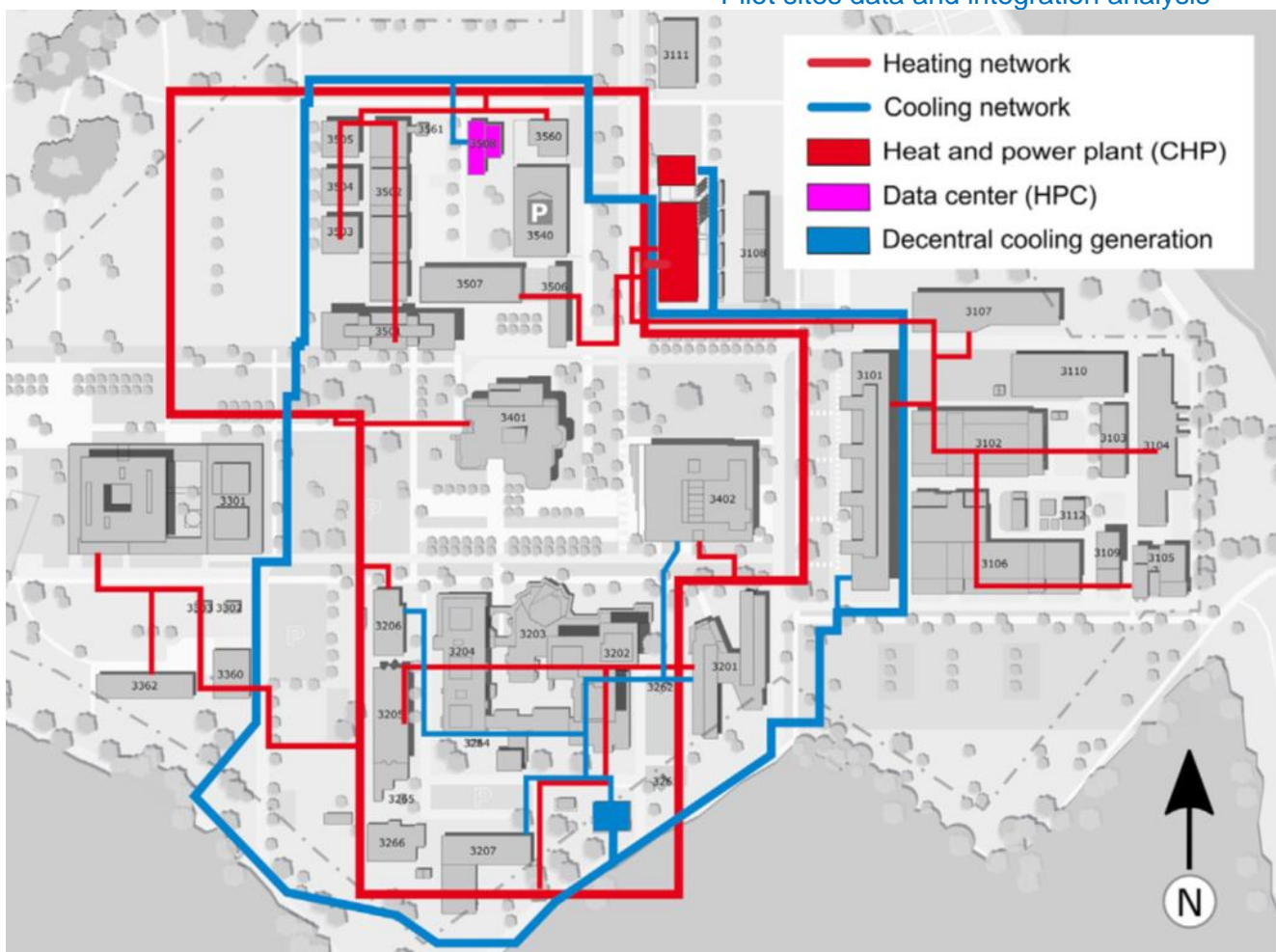


Figure 22: TU Darmstadt campus Lichwiese district heating and cooling network in 2018 (Changed after Oltmanns, 2021, Formhals et al. 2021).

Description and Schematic overview on different integration options of the HOCLOOP concept

The option that is foreseen for the integration of the HOCLOOP concept would consist in drilling new closed-loop horizontal wells with much deeper bottomhole as shown in Figure 22. This will provide us more leverage on integrating it with district heating system with or without heat pump. As the aim is to lower temperature levels of the DH-system in the future, geothermal solutions like horizontal closed-loop heat exchangers will become a viable solution for a renewable heat supply of the campus. Especially with the then well-explored subsurface conditions.

HOCLOOP

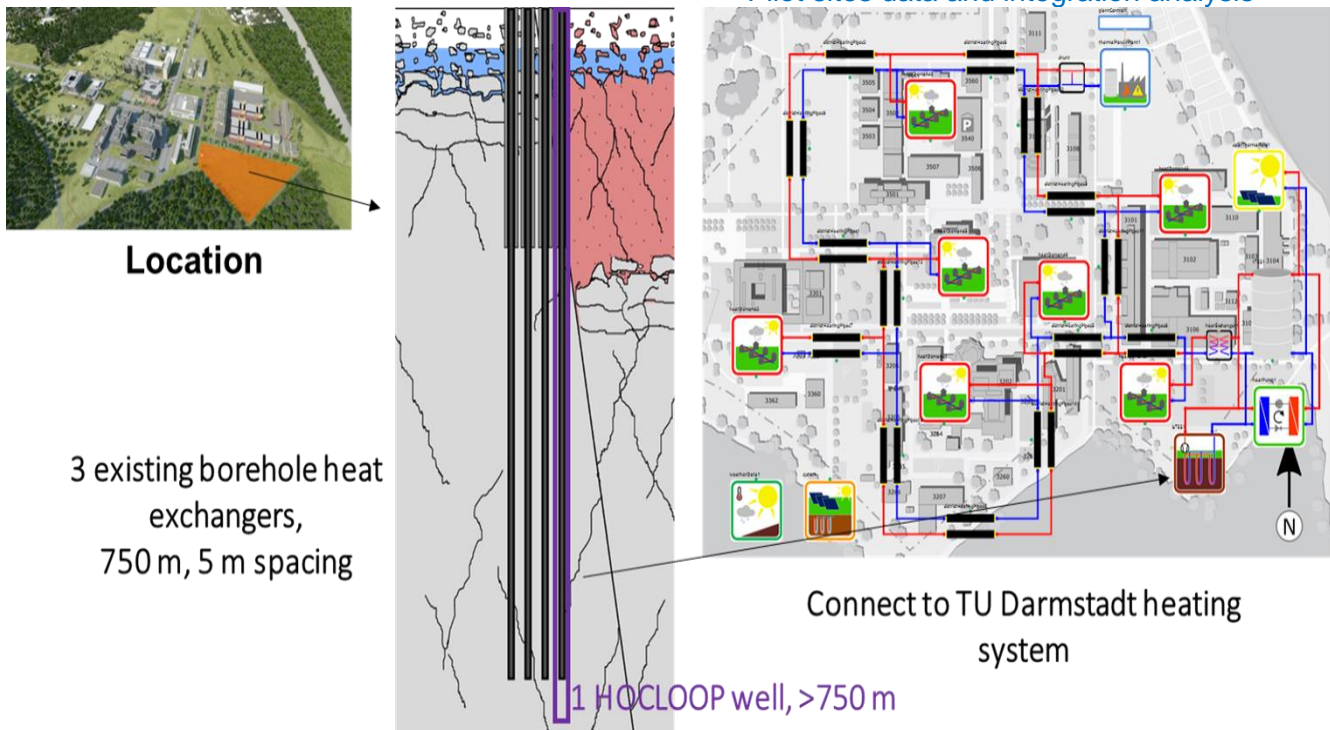


Figure 2322: HOCLOOP integration with TU Darmstadt DHS.

Pros:

- DH system is already developed.
- It is easy for integration of HOCLOOP with both DH system or with a single building.

Cons:

- New horizontal closed loop wells are required.

Technical challenges

The geological site of the Lichtwiese drilling site has a complex geological setting which may lead to additional cost. These losses may incur by for example by the mud losses.

Current technical challenges are:

- Seismicity: It is a closed system. Therefore, there have not been any seismicity.
- Scaling issues will not occur as it is closed system.
- Drilling fluid losses occurred during the drilling process which require cementation of certain well area before the continuation of the drilling was made possible.

Economic aspects

By 2026, the business model solution will be tested at TRL7. However, the output will be solely used for university consumption.

Summary table

Parameter	Value	Unit
Geological information		
Top reservoir Depth	200	m
Thickness of the reservoir	-	m
Temperature at the top of the reservoir	15.2	°C
Type of reservoir (homogeneous, fractured/fissured)	Fractured	
If fractured, fracture distribution type	-	
Hydraulic properties		
Hydraulic conductivity of the crystalline basement	4e-8	m/s
Matrix porosity	0.03	%
Thermal properties		
Thermal conductivity (in reservoir)	2.71	W/m.K
Thermal conductivity(ies) above	2.71	W/m.K
Geothermal gradient(s) up to the top reservoir	21	°C/km
Thermal Capacity (reservoir rock)	2.16	J/kg/K
Well design		
Well 1 length	750	m
Well 2 length	750	m
Well 3 length	750	m
District heating network		
Supply temperature	65-105	°C
return temperature	50-75	°C

4.4 Case study Parisian basin, France (IFPEN)

General description of the pilot site

The Parisian basin subsurface is exploited by deep geothermal doublets for district heating since 1969 and the density of the exploitation of the Dogger carbonates is the largest in the world with 49 doublets in activity. New reservoirs are targeted as the deeper and hotter Trias (up to 90 °C) or the shallower and more accessible lower cretaceous (35-40 °C), both silico-clastic reservoirs. However, the Trias projects realised in the 1980's have failed due to a rapid loss of injectivity, and the lower Cretaceous recent realizations face similar difficulties. To reach the target of the French pluri-annual energy plan, different options must be considered, among which the close loop concept. The geological setting of this case study is representative of a sedimentary basin in thermal equilibrium and thus with a normal geothermal gradient. Not limited by the known aquifers, different depths should be considered from 200 m to the basement. For most of the depths, no heat recharge is to be considered, but in presence of an aquifer, a heat advection associated with the natural hydrodynamic will be considered. For the closed-loop modelling at different depths, direct petrophysical data are not available. The rock parameters needed for the simulation will be based on IFPEN existing basin models calibrated with the available data.

For this study, a geothermal site was to be selected to consider the applicability of the HOCLOOP technology to the Paris basin. The site selection was based on the following criteria:

- The presence of the different known aquifers of the sedimentary pile,
- The availability of the data, among which a well log down to the Trias,
- The large need for renewable heat and cold at the surface.

Considering these criteria, the site of Fresnes, south of Paris, near Paris Orly airport (Figure 24) was chosen. This area is densely populated, and the Dogger reservoir is already widely exploited. There, geothermal heat production started in 1986 with one production and one injection well reaching the Dogger limestones reservoir, and new investments were made in 2010 to drill a third well as production well and refurbish the two first as injector wells. The surface heat distribution network is growing over the years. In parallel, a 2667 m-deep oil & gas well reaching the Lower Cretaceous was also drilled in 1984, and logs are available.

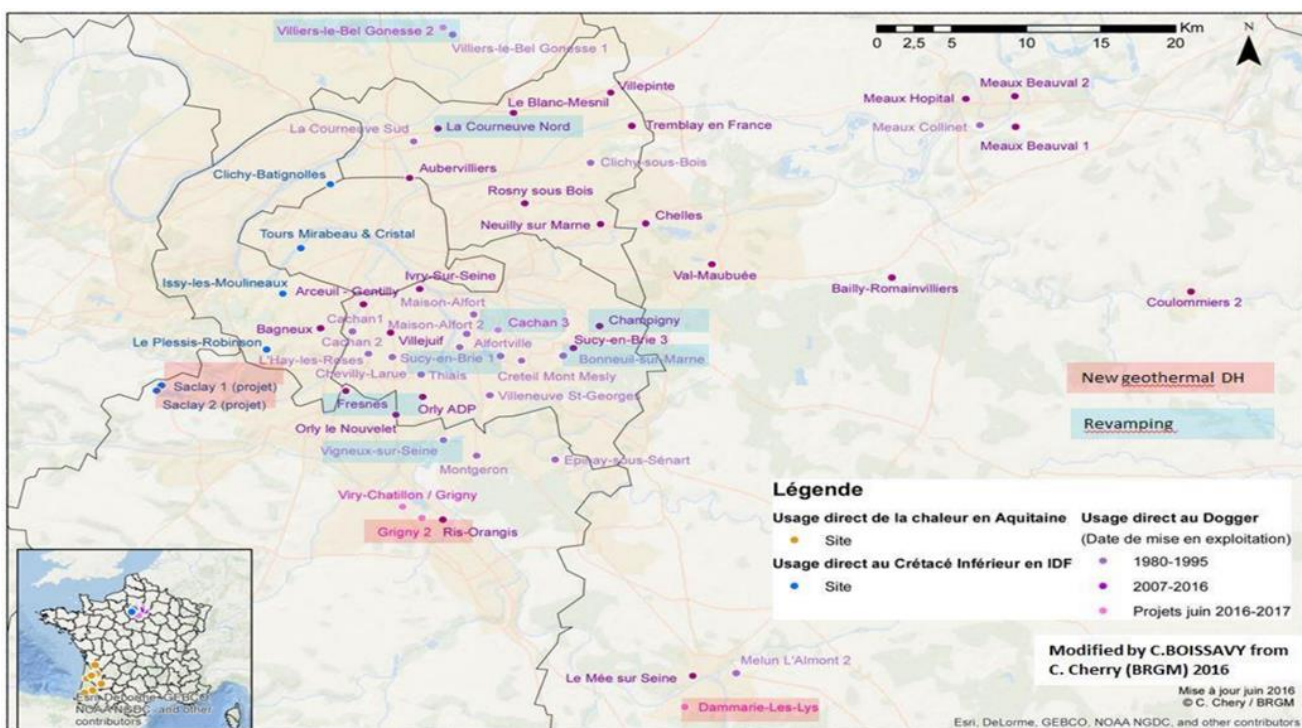


Figure 24: Geothermal doublets used for district heating existing in the Paris area in 2016. Blue dots indicate a lower Cretaceous target while the pink and purple indicate a Dogger target. The different shades of pink/purple refer to the date of commissioning. The pink dots were in project in 2016 but have been realized since then. From Boissavy et al.2019

Geological conditions

Regional setting

The Paris basin (Northern France) is characterized by two different evolution histories; the first one is linked to the last phase of the Hercynian orogeny during which a strong fault activity has led to a sudden subsidence in some specific regions (e.g., Saar-Lorraine basin and Contres-Brecy basin) followed by the deposition of the Paleozoic continental source rocks. The second one is linked to the Alpine evolution and represents the beginning of the Paris basin history in which the first depocenter is formed (Carnian age) followed by the deposition of the Mesozoic marine source rocks.

The Hercynian orogeny was the major tectonic event that affected the Paris Basin. It was the result of a north-south compression that initiated a set of structures in the basement of the basin (Weber, 1973). Along the northeastern edge of the basin, the faults trend towards 60°N (NE-SW Metz, Verdun-

Luxembourg, Wittlich faults); in the west they are oriented 120°N (NW-SE Eu, Somme, Bray, Seine Banthelu faults); in the southern portion they are oriented 90°N (N-S Sennely, Sancerre, St Martin-de-Bossenay faults) (Parrodon and Zabek, 1990; Delmas et al.; 2002).

The initial thermal anomaly at the origin of the subsidence of the Paris basin is most probably inherited from the Late Carboniferous-Early Permian Variscan history (Prijac et al., 2002). At the same time (Stephanian-Autunian) orogenic and post-orogenic rift basins subsided and were filled with continental coal-bearing sediments. These Paleozoic rift basins are the result of the first phase of post-orogenic shearing, following the Y-pattern of the basement.

During the Early and Middle Triassic, the Paris basin formed the western end of the Germanic basin, under an overall continuing extensive tectonic regime, due to Tethys opening, with strong faults activity (Beccaletto et al.; 2010; Delmas et al.; 2002). This extensional phase was a period of high heat flow (Brunet et al; 1981), but there was not known volcanic activity within the Paris basin. Grabens developed over the Y-pattern of faults within the basin, separating the Armorican, Morvano-Vosgian and Ardennes blocks; the thickness and facies variations of the Mesozoic Series indicate that these blocks are fundamental elements of the basin's framework (Parrodon and Zabek, 1990).

During the Late Triassic a gradual sea level rise was followed by a gradual diachronous westward progression of the depocenters and nearshore and continental clastics sediments gradually prograded across the basin from west to east (Ziegler, 1980; Durandau and Koning, 1985). At the end of the Triassic, the Paris Basin was a northeast-trending sag depression filled with an average of 500 m of sediments.

During the Early Jurassic time (Lias) took place a rapid subsidence and the Paris Basin expanded from restricted trenches to a more extensive basin (Parrodon and Zabek, 1990). From the Hettangian until the Toarcian the sedimentation was characterized by the deposition of pelagic organic matter rich sediments deposited in a restricted area near the center of the basin. The subsidence rate slowed down during the middle Jurassic time (Brunet and Le Pichon, 1982; Loup and Wildi, 1994) and this decrease has been interpreted as evidenced for a post-rift thermal decay associated with the Thethys rifting. During the Kimmeridgian the Paris basin was characterized by local subsidence along the rejuvenated basement faults: in the western part it was connected to the widening proto-Atlantic Ocean while the southeast side remained open to the Thethys sea (Parrodon and Zabek, 1990). Until this period the Paris basin had been subjected to continuous extension. The Tithonian marked the beginning of the first exposure of the Paris basin, with the uplift of the Vosges-Rhine block to the northeast, due to early compression.

In the Lower Cretaceous the basin was invaded by the boreal sea while the Lorraine arch remained exposed and closed the basin to the northeast; in this shallow-marine environment took place a clastic sedimentation. During the Upper-Cretaceous an eustatic sea-level rise and a renewed subsidence in the central part of the basin lead to an increase in the sedimentation rate followed by chalks deposition. The sea retreated completely from the basin at the end of the Cretaceous (Parradon and Zabek, 1990).

The boundary between Mesozoic and Cenozoic corresponds to an erosional hiatus due to latest Cretaceous and mid-Paleocene compressional intra-plate deformations which can be related to stresses exerted by the Pyrenean and Alpine orogens (Ziegler 1988, 1990). These two compressional periods were separated by an Oligocene extensional event in the southeastern part of the basin. During the

Tertiary it was sensitive to slight eustatic variations of sea level followed by numerous transgressive and regressive cycles before the complete emergence of the basin (Brunet, 1981).

At present day, the Paris basin is in thermal equilibrium. THM modelling (Torelli et al., 2020) shows that the thermal structure of the basin is dominated by conduction, no effect of heat advection could be demonstrated. The heterogeneity is due to the basement rock types as well as the thicknesses and thermal conductivities of the overlying sediments.

Lithostratigraphic framework

The chrono-stratigraphic chart of the Paris Basin is displayed in Figure 25. As a whole, the Paris Basin underwent subsidence and sedimentation since Triassic time. Its total thickness is of around 800 m in the northeastern part, 700 m in the central part and 500 m in the southern area (Perrodon and Zablek, 1990).

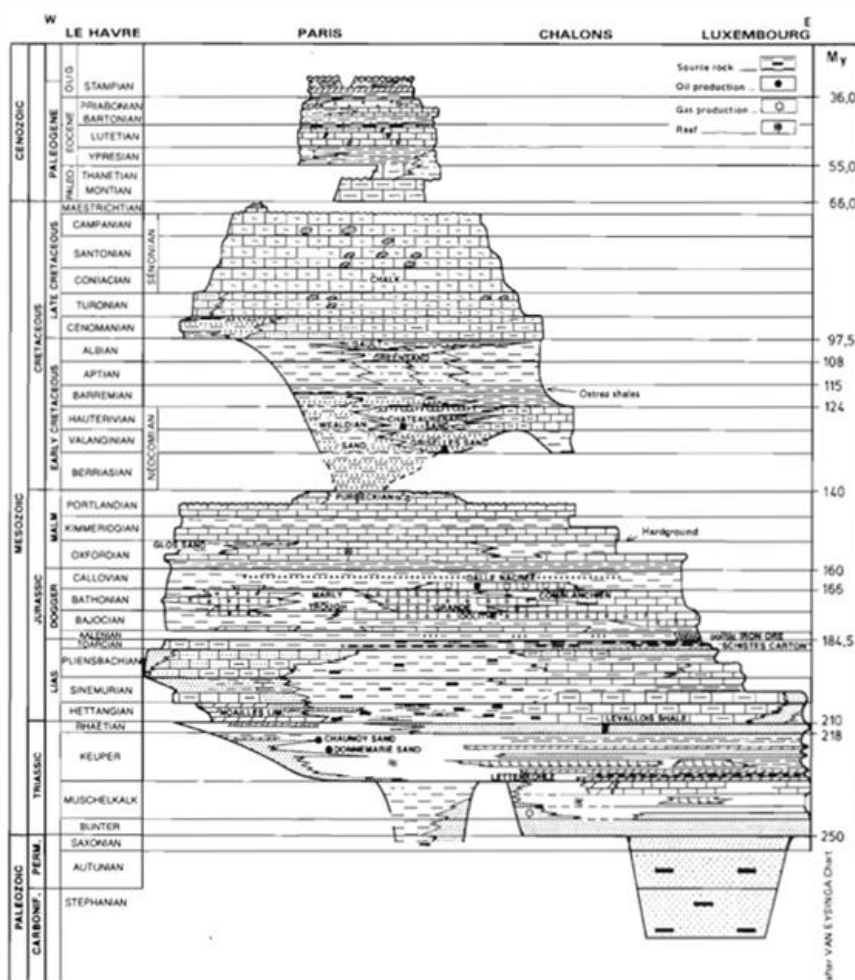


Figure 25: Chrono-stratigraphic chart of the Paris Basin

The chrono-stratigraphic chart of Figure 25 shows the three main formations making up the Triassic interval of the Paris Basin: Bunter (Bundsandstein), Muschelkalk and Keuper characterized by gradual progradation from east to west. In detail, the Buntsandstein Fm is confined in the eastern part of the basin and presents sandstones with conglomerate intercalations and layers of thin shales. The Muschelkalk Fm. is made up by sandstones, marls, dolomites and thick evaporitic rocks (75 to 100 m).

Sandy beds beneath the evaporate seal constitute a petroleum trap in the eastern section of the Paris basin (Parrodon and Zablek, 1990). About the Keuper Fm., it consists of sandstone overlaid by clays.

The Jurassic started with a thick succession of shales and carbonates, due to a period of subsidence synchronous of extensive transgression. The Liassic Formation consists mainly of organic-rich black shales with an average thickness of 500 to 600 m. The most important source rocks of the Paris basin were deposited in this period (Schistes Cartons). During the Dogger, there was the evolution of a large carbonate platform; the subsidence was minimal, and the sea level was stable (Purser, 1975; Curnelle and Dubois, 1986). The Dogger limestone reaches 400 m in the central Brie-Champagne region and represents one of the main oil exploration targets in the Paris Basin. The Malm is characterized by regressive sequences that grade from shaly facies to skeletal carbonates, indicating a gradual filling of the basin. The Tithonian ended with marly limestones grading upward to subreefal and lagoonal limestones, a prelude to an important regression and the exposure of the basin (Perrodon and Zabek, 1990).

In the Early Cretaceous, sandy and shaly continental deposition occurred in the Paris Basin. During the Hauterivian, the deposition changed and became mostly marine limestone and sands. The Lower Cretaceous reaches a thickness of 300 to 400 m in the central part of the basin. The Upper Cretaceous was characterized by an eustatic sea-level rise, and chalk with chert interbeds was deposited. The thickness reaches 350 to 400 m in the Brie area east of Paris. Most of the basin was exposed above sea level at the end of the Cretaceous.

The Tertiary in the Paris Basin was characterized by a drastic reduction of the sedimentation rates. Several sea invasions occurred from the North Sea or from the Atlantic (Cavelier and Pomerol, 1979; Gély and Lorentz, 1991). During this period high sequences of clastic deposits were recorded, due to Pyrenean and Alpine movements. The Rupelian erosion surface marks the emersion of the basin and the end of sedimentation.

Local structural setting

The study area around the FRESNES-1 well (FRS 1 in the Figure 26 here below) is located in the central part of the Paris Basin, a few kilometres south of Paris.

From a structural point of view, Figure 26 and Figure 27 show that the study area is located in a relatively stable and poorly deformed zone, i.e. far from the major faults affecting the Paris Basin (Figure 27).

The end of drilling report associated to the FRESNES-1 well indicates a general dipping of beds towards NW all over the drilled interval. Dips are highly variable between 2072 m MD (Lias) and 2666 m MD (Keuper Fm), with the exception of the Middle to Upper Lias, where beds are quite sub-horizontal.

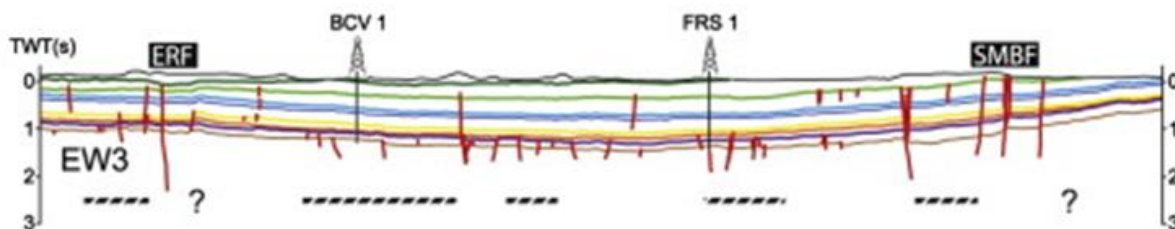


Figure 26: Seismic cross-section through the study area, interpreted by Beccaletto et al. (2011). The location of FRESNES-1 well is also displayed (FRS 1 in the figure).

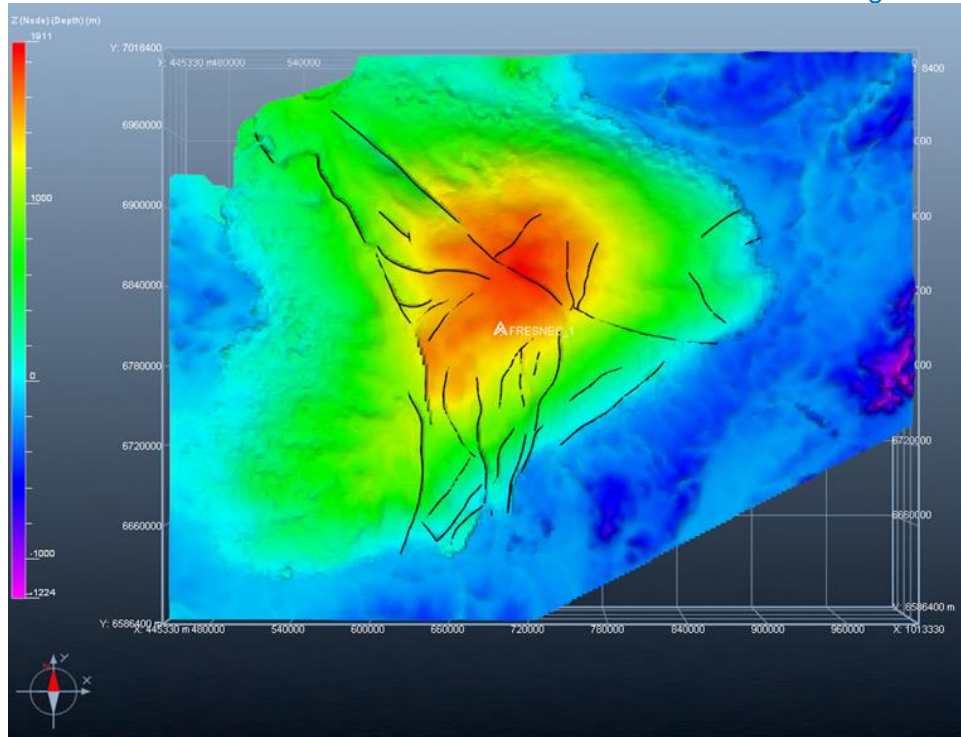


Figure 27: Structural map at the top of Bathonian reservoir, showing the fault network affecting the Paris Basin. Location of FRESNES-1 well is also displayed.

Description of the geological target

Lithology, depth and thickness

The FRESNES-1 well intersected the following reservoir rocks:

- Green sands Albian (590-637m): shaly sandstones alternated with sands and thin layers of shales
- Oxfordien (1237-1061m): packstones and mudstones;
- Bathonian (1639-1840m): high energy calcarenites (Oolithe Blanche Fm) and grey packstones and wackestones (Comblanchian Fm);
- Lower Callovian (1631-1639m): dark grey shaly wackestones alternated with light grey to white grainstones (Dalle Nacrée Fm.);
- Rhetian Trias (2230-2240m): light grey shales alternated with fine-grained sandstones;
- Donnemarie Fm. (2439-2491m): fine-grained sandstones alternated with thin layers of red silty shales.

The impermeable units crossed by the FRESNES-1 well were the following:

- Gault Albian clays (546-590m): dark grey to black shales, very glauconitic, bioturbated and rich in fossils;
- Barremian (637-908m): multicolored sandy shales to shaly sands;
- Upper Callovian (1601-1631m): grey marls to calcareous shales;
- Middle and lower Lias (2060-2230m): shales to marly shales, with rare intercalations of mudstones and shaly mudstones.

Used data

Hard data

- Caliper, Gamma-ray log (GR), sonic log (DT) are available down to the lower Trias
- End of survey report with the depth of the different markers and a lithologic description based on cuttings observation.
- A large-scale Paris basin model is available. It is based on the analysis of thousands of wells, and the interpretation of numerous seismic sections.

Data resulting from basin modeling

Additional data like thermal properties, mechanical properties, flow properties, formation fluid and the temperature model result as outputs of the Paris Basin model built at IFPEN for R&D purposes. Basin modeling is the dynamic modeling of geological processes in sedimentary basins over geological time spans. A basin model is simulated forward through geological time starting with the sedimentation of the oldest layer until the entire sequence of layers has been deposited and present day is reached. Several geological processes are calculated and updated at each time step. Most important are deposition, compaction, heat flow analysis, porosity, permeability, etc.

The general analysis of the basin type and the main phases of basin evolution precede the construction of the model input data. This encompasses information about plate tectonics, rifting events, location of the basin, and depositional environments through geological time, global climates, paleo– bathymetries, and tectonic events. Input data used to build a basin model include present day model data with depth horizons, facies maps, fault planes, the age assignment table for the geological event definition, additional data for the description of paleo–geometries, thermal and mechanical boundary conditions through geologic time, the property values for lithologies, fluids, compaction curves for each defined lithology.

Description of the geothermal target

Temperature model

In the Paris Basin model, the numerical simulation of the thermal properties were pointed out based on different parameters such as sedimentation, facies, porosity, radiogenic production and thermal conductivity. Input physic and thermal parameters for each facies of the model were defined with the default values defined in the software which, in turn, were based on the existing bibliography. In detail, data from 54 wells within the basin containing information on surface temperature, temperature at base upper mantle and the temperature gradient were entered in the model to calibrate the present-day thermal regime. On the contrary, the past thermal regime has been calibrated using different kinds of paleo-thermal parameters, such as measured vitrinite values (Uriarte, 1997), fluid inclusions (Guilhaumou, 1993) and clumped isotope thermo-chronometers ($\Delta^{47}\text{-U/Pb}$).

Flow properties

Flow properties of the different units making up the model were pointed out based on compaction curves vs depth. These latter are the controlling factors for modeling, among others, porosity evolution during both backward and forward modeling. Figure 28 displays a compaction curve used as input data for the Comblanchian Fm (Bathonian).

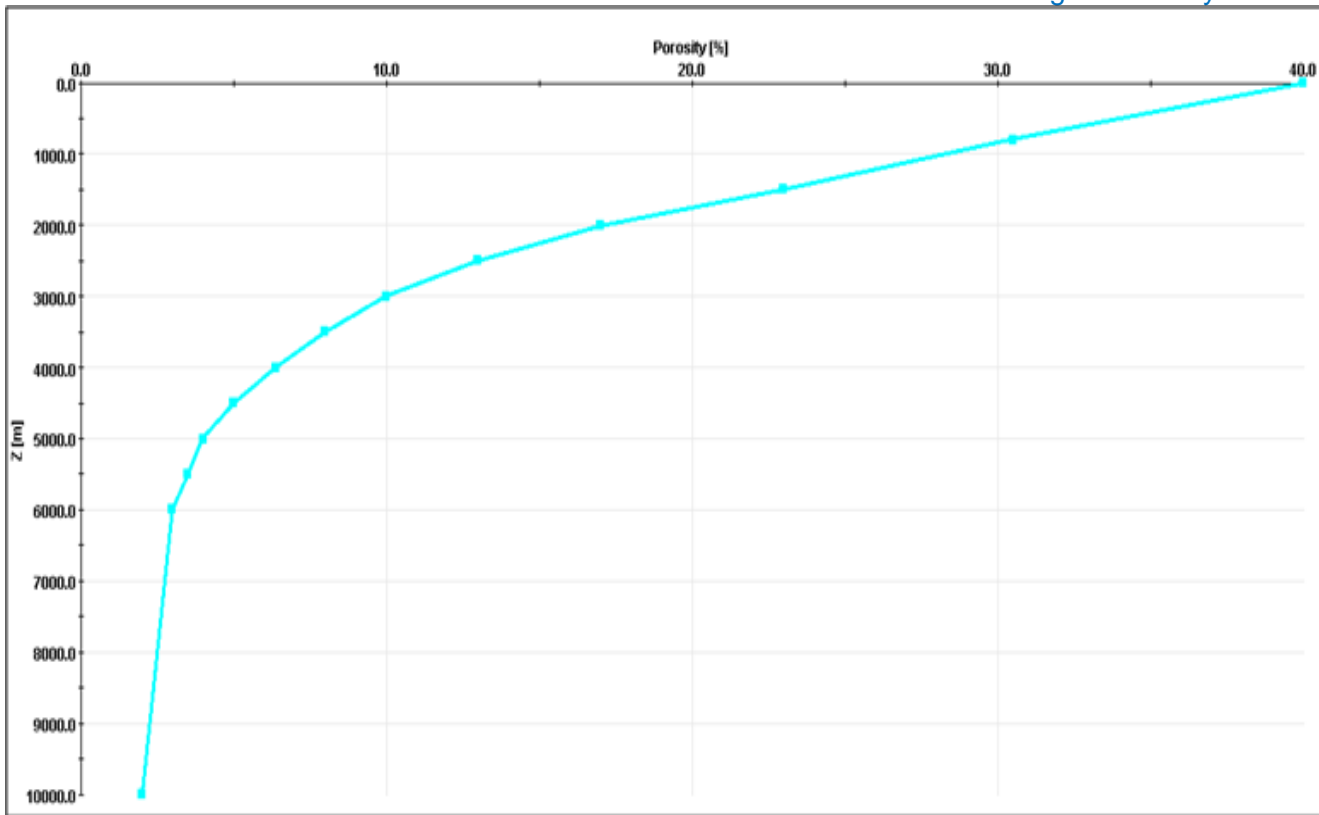


Figure 28: Example of compaction curve (porosity as a function of depth)

Finally, the permeability was computed by using a permeability-porosity relationship which is typically expressed by the Kozeny-Carman equation. Figure 29 illustrates an example of permeability-porosity relationship, coming from the Comblanchian Fm. In detail, this curve has been calibrated with values of porosity and permeability from available data (cores, dynamic data) and then used to compute permeability maps (K_x , K_y and K_z).

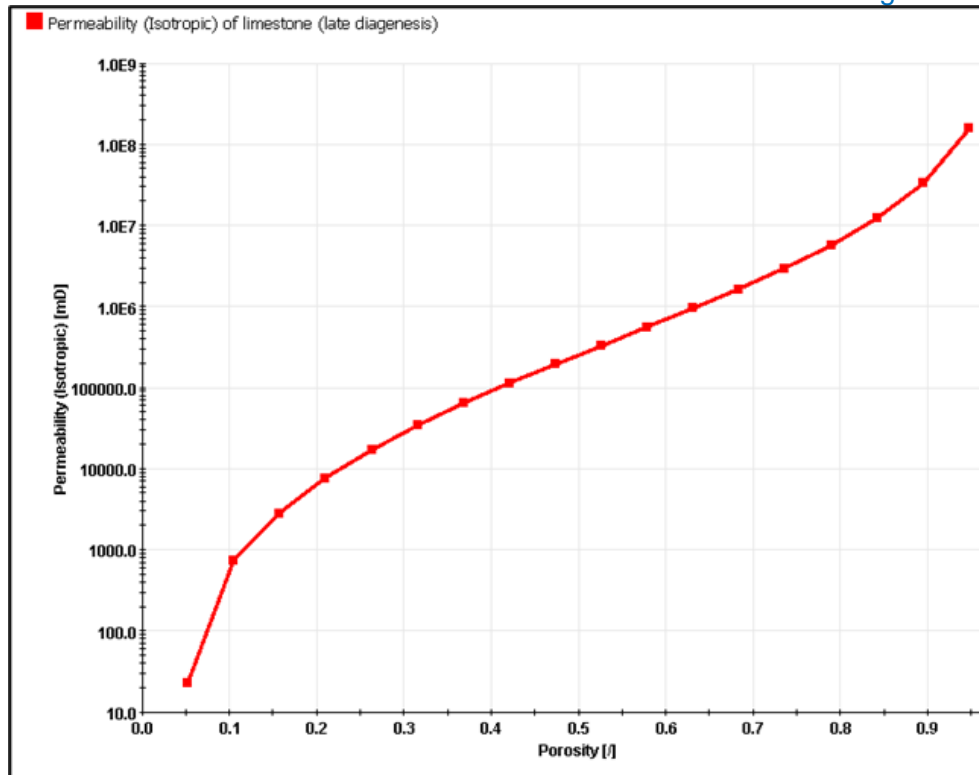


Figure 29: Example of permeability-porosity relationship, coming from the Comblanchian Fm (Dogger)

Data from simulation

Table 18 summarizes the data extracted from the best simulation of the Paris basin.

Table 18: Summary of the data extracted from the calibrated paris basin simulation for the Fresnes well: Facies (aquifer in yellow, seals in green), and their associated depth, flow properties (porosity and horizontal permeability), thermal properties (temperature, thermal conductivity and its temperature dependency) as well as the modelled natural brine velocity in the reservoir (Qmean).

	MD	Temperature [°C]	Thermal capacity [J/C.kg]	Thermal Conductivity[W/(m²·°C)]	T° dependency (1/°)
Gault_Shale	548	30,6	903	1,59	4,00E-04
Albian	608	32,6	859	3,16	3,00E-04
Barremian	754	38,3	915	1,63	3,00E-04
Oxfordian (Lusitanian)	1322	58,4	795	2,24	3,00E-03
Callovian	1623	68,1	915	1,73	3,00E-04
Lower Callovian (Dalle Nacrée)	1727	71,7	805	2,14	2,60E-03
Bathonian (Comblanchian)	1767	73,7	806	2,14	2,60E-03
Dommerian	1963	81,0	915	1,74	3,00E-04
Rhetian (Chaunoy)	2146	88,0	887	2,63	3,00E-04
Anisian (Donnemarie)	2590	100,4	710	2,94	3,70E-03

	Qmean (m/My)	Bulk Density [g/cc]	Porosity [%]	KH [mD]
Gault_Shale	69	2,38	0,19	1,7E-02
Albian	4441	2,27	0,23	1,4E+00
Barremian	23	2,48	0,13	5,3E-03
Oxfordian (Lusitanian)	813	2,39	0,19	1,2E+00
Callovian	1	2,59	0,07	3,0E-04
Lower Callovian (Dalle Nacrée)	18	2,45	0,14	2,5E-02
Bathonian (Comblanchian)	15	2,59	0,06	4,0E+01
Dommerian	0	2,60	0,06	1,7E-04
Rhetian (Chaunoy)	22	2,51	0,10	3,0E-02
Anisian (Donnemarie)	800	2,37	0,18	3,9E+00

Knowledge gaps

- The data with the largest uncertainty among those useful for the close-loop technology assessment concerns thermal conductivity. No direct data are available in the end of survey report. The thermal conductivities presented hereabove are resulting from the modelling, but, in absence of data, no calibration on existing data has been carried out.
- A work is in progress on the different ways to evaluate the rock conductivity either from logs or from the mineralogy, based first on a bibliographic study as the thermal conductivity of rocks has been previously studied not only for the petroleum system assessment but also for the burial of radioactive waste.

Past/Current/future above ground energy system

Schematic of the geothermal installation

The Fresnes geothermal site is based on 3 wells targeting the Dogger reservoir:

- 2 injection wells
- 1 production well.

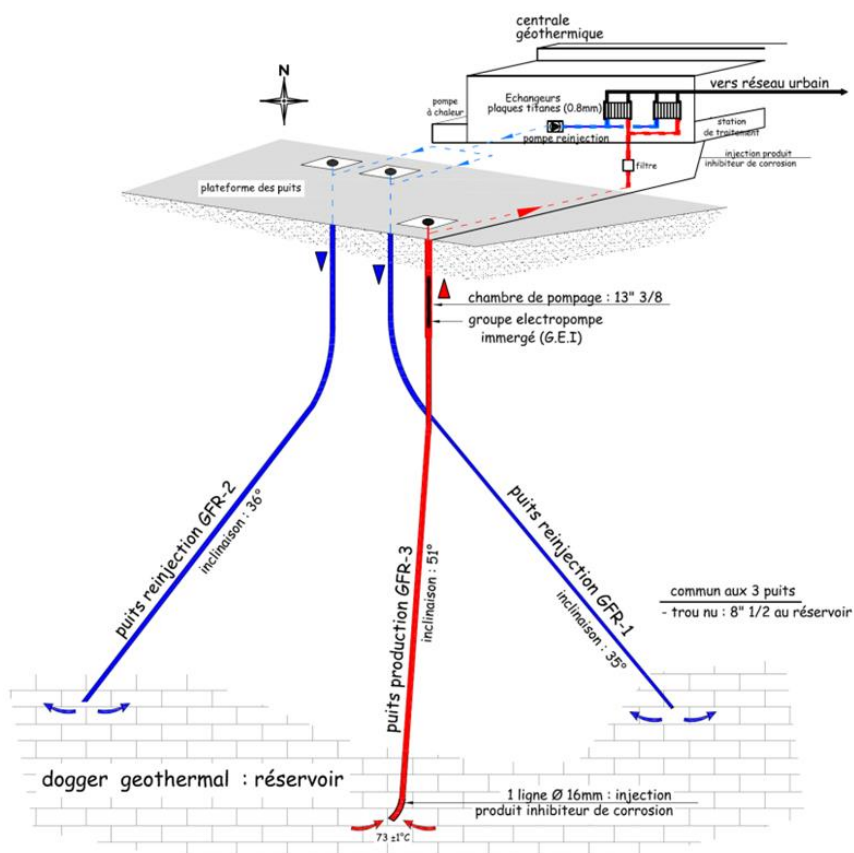


Figure 30: Schematic representation of the production (red) and two injection (blue) wells, reaching the Dogger limestones reservoir, and simplified surface installations (From « Schéma directeur du réseau de chaleur à base géothermique de la ville de Fresnes »).

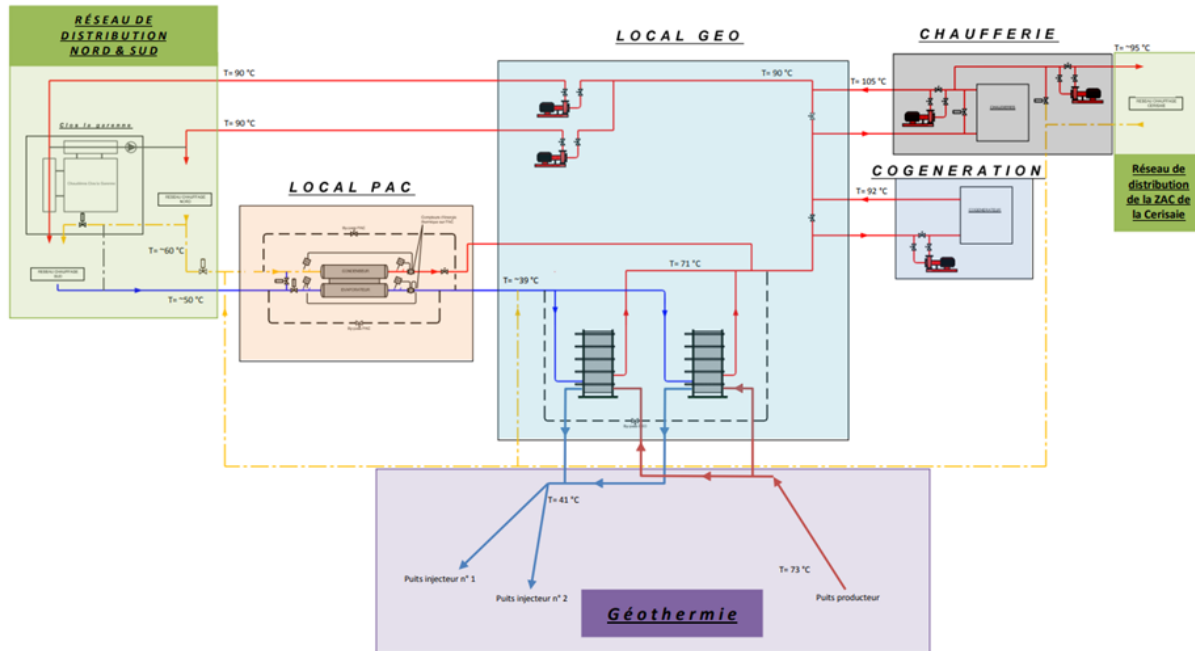


Figure 31: Schematic diagram of the Fresnes geothermal power plant (From « Schéma directeur du réseau de chaleur à base géothermique de la ville de Fresnes »). Local PAC : heat pump room ; Local geo : geothermal installations room including the filters, the heat exchangers as well as the pumps for the secondary fluid; chaufferie: boiler house; Réseau distribution: heat network.

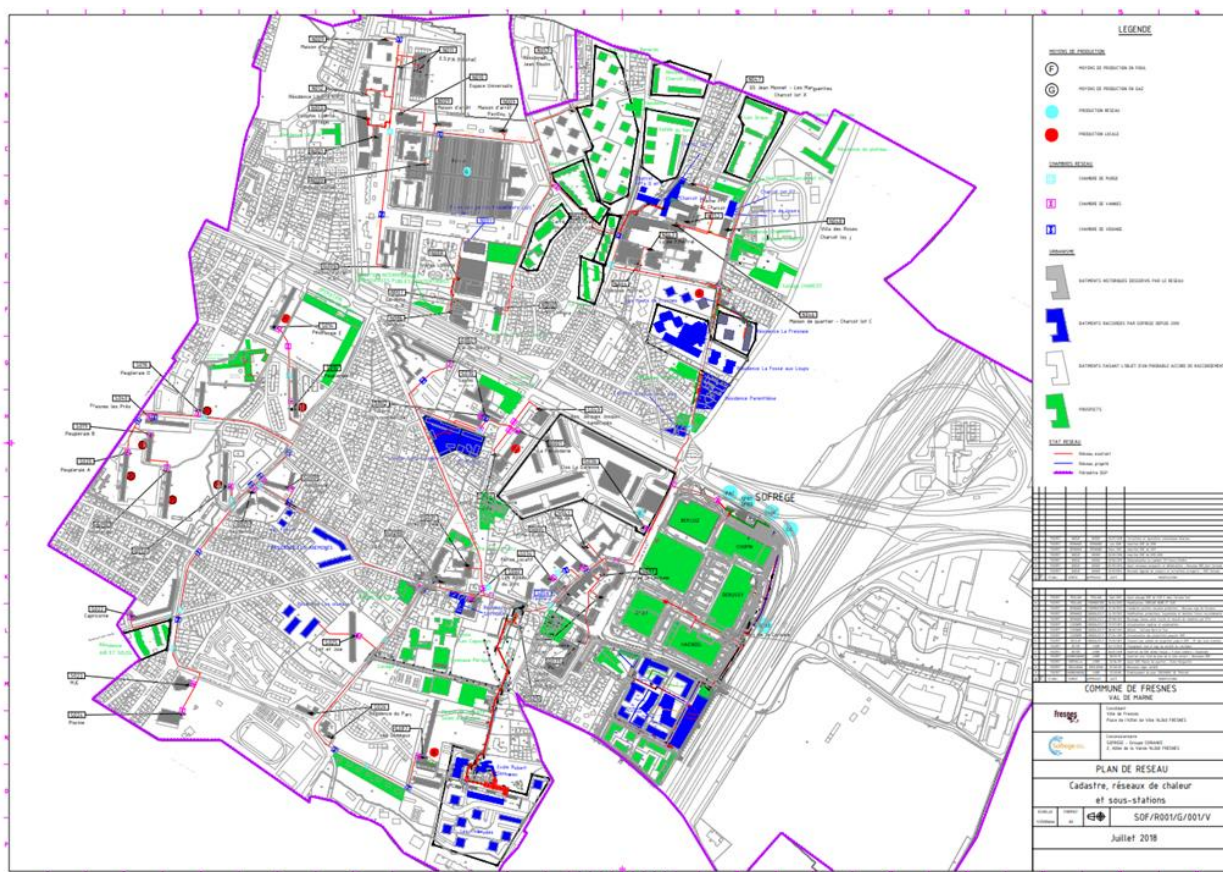


Figure 32: Map of the district heating before 2010 (grey buildings), connections since 2010 (blue buildings) and present prospect (green buildings). From « Schéma directeur du réseau de chaleur à base géothermique de la ville de Fresnes ».

This configuration results from the evolution of the site since its first commissioning in 1986. At that time 2 wells were drilled GFR-1 and GFR-2. In 2010, as the production well was damaged, a third well was drilled as a productor well and the two first wells were rehabilitated to be both injector wells. At the same time, an extension of the district heating was realized, and the surface installations were updated to include high temperature heat pumps and cogeneration.

At present day, the primary fluid is produced from GFR-3 at 73°C with a 250 m³/h flowrate, goes through the filtration, the heat exchangers, before being reinjected between 41 and 35°C in wells GFR-1 and GFR-2. If outside temperatures fall below 8°C, a thermal heat pump is used after the heat exchangers and the temperature of the reinjected brine is falling down to 25°C. This outside temperature limit is 6°C if the parallel cogeneration turbine is used. Emergency turbines are also present for maintenance or any breakdown of the installations.

General overview of the future plans

In the present configuration, the geothermal district heating network covers 76% of collective housing and public equipments. A network enlargement is planned (Figure 32) and an additional production well might be needed in the future. This enlargement might be difficult in an area with a high density of geothermal wells already drilled or planned.

Description and Schematic overview on different integration options of the HOCLOOP concept

The HOCLOOP technology could be an alternative solution to the drilling of an additional production well. The best option in that case, would be to target layers at different depths than the Dogger reservoir. During the HOCLOOP project, the optimization of the depth of the horizontal part of the well, its length, the diameters, insulation and the nature of the heat transfer fluid will be analysed to obtain the best heat production over time. This work will be based on the previously presented data for the different aquifers and seal lithologies.

Economic aspects

Current and future heat prices

In 2018, the heat production of the deep geothermal sector in France reached 1,78 TWh for an installed capacity of 627 MW. 93% of this production feed the collective heat network, 6% the agriculture, 1% the balneology. This covers only 0.3% of final 2018 French heat consumption (cf. "Panorama de la chaleur renouvelable et de récupération – Edition 2019")

LCOE for heat production (not taking into account the heat distribution) for these projects were comprised between 15 and 55€/MWh (Figure 33). At the same period, the cost of the heat production from new combined cycle gas powerplants was between 50 and 66€/MWh.

Considering the present gas cost increase, geothermal energy is becoming more competitive, even if the geothermal project CAPEX will also need to be re-evaluated.

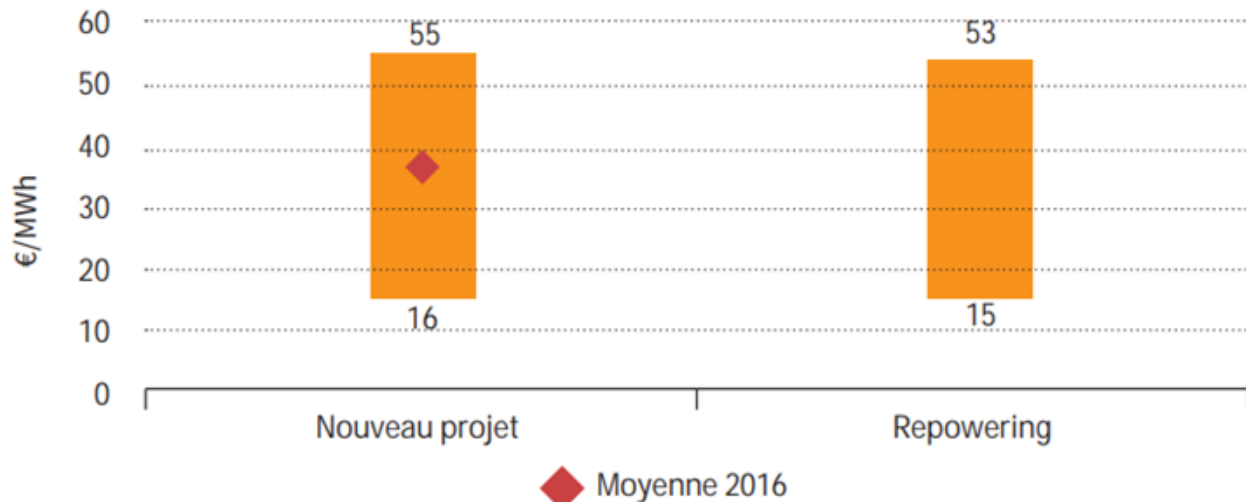


Figure 33: LCOE for heat from deep geothermal energy in France based on the 9 last projects realised before end 2017 (Haeusler et al., 2020), either new or corresponding to repowering of existing sites.

CAPEX of the HOCLOOP solution

It is important during this project to evaluate the cost of a MWh using the HOCLOOP technology. The cost might be reduced by using existing abandoned geothermal wells. Since the main reason for abandoning a well is insufficient permeability, these already drilled wells could eventually be used for a closed loop geothermal system. The conversion of O&G wells has already been considered (H2020 MEET project) but several problems were raised making it very difficult to reuse oil wells for geothermal energy. The conversion of dry geothermal wells to a closed loop would not require changing the type of use of the well and the mining code should therefore not be an issue. These wells, already intended for direct heat use, are located close to the heat needs. In addition, the well diameters are already large and therefore suitable. Once the conditions of efficient deployment of the proposed closed loop technology are defined, the wells that could be reused will be considered.

Summary table

Parameter	Value	Unit
Geological information		
Top reservoir Depth	1767	m
Thickness of the reservoir		m
Temperature at the top of the reservoir	73,7	°C
Type of reservoir (homogeneous, fractured/fissured)	Porous homogeneous	
If fractured, fracture distribution type		
Hydraulic properties		
Permeability of the reservoir	40.10 ⁻¹⁵	m ²
Matrix porosity	6	%
Regional flow	15	m/My
Thermal properties		
Thermal conductivity (in reservoir)	2,14	W/(m ² .°C)

Thermal conductivity(ies) above	1,73	W/(m ² .°C)
Geothermal gradient(s) up to the top reservoir	35,3	°C/km
Thermal Capacity (reservoir rock)	806	J/C.kg
Geothermal loop		
Extraction well depth (GFR-3)		m
Injection well 1 depth (GFR-1)		m
Injection well 2 depth (GFR-2)		m
Brine extraction temperature*	71	°C
Brine extraction flow*	250	m ³ /h
Brine reinjection temperature*	35	°C
Brine reinjection max temperature*	41	°C
Hot water loop		
Supply collector water temperature*	90	°C
Return collector water temperature*	50	°C
Supply and return collectors pipe size		-
Heat transportation network		
Supply temperature*	90	°C
return temperature*	50	°C
distribution pump flow rate		m ³ /h
distribution pump delivery pressure		barg
distribution pump discharge head		m
distribution pump NSPHa		m
pipe length to VITO boiler house		km
pipe diameter to VITO boiler house		-
Boiler house		
Gas boiler capacity*	18,9	MW _{th}
Gas boiler quantity		-
HTR/DHG heat exchanger capacity*		MW _{th}
HTR/DHG heat exchanger quantity		-

4.5 Case study Italy

The tectonic evolution of Italy resulted in a wide range of heat flux values, from low (about 40 mW/m²) to very high (> 1000 mW/m²), affecting areas with different lithologies and tectonic settings. Thanks to this, different Italian case studies have been selected as examples of a wide range of geological settings for possible application of the closed-loop technology (Figure 34).

The first case study, Gargano, south-eastern Italy, is representative of low heat flux regions and is characterized by a heat flux value of about 40 mW/m². It is defined by Jurassic-Cretaceous fractured limestone with local hydrothermal circulation. The area is rich in geophysical and boreholes information, permitting integration with data collected at the surface (fracture distribution and lithology) and providing the dataset for evaluating the potential location of the HOCLOOP solution, in the presence/absence of hydrothermal fluids at suitable depth, through modeling.

The second and third Italian cases, Gavorrano and Monte Amiata, are representative of regions with intermediate and high heat flux as the value there are about 70 mW/m^2 and higher than 80 mW/m^2 , respectively. Both Gavorrano and Monte Amiata are located in central Italy, (western side) where the thermal anomaly is regionally relevant.

The Gavorrano case is an abandoned mining area, where geophysical and sub-surface data is available. Integration with the fracture distribution dataset will enable to define a clear picture of the possible water pathways, providing key information on the potential HOCLoop solution in such a context. On the other hand, the Monte Amiata area is close to an active geothermal field where a massive dataset on the substratum is already available. Here, the solution will potentially focus on shallow depth and, the geometrical setting of surficial permeable fractures, connected to the target will be studied.

- ★ **Gargano:** $\approx 40 \text{ mW/m}^2$
Boreholes and geophysical data
- ◆ **Gavorrano:** $\approx 70 \text{ mW/m}^2$
Mining area
- ◆ **Mt. Amiata:** $> 80 \text{ mW/m}^2$
Mining area

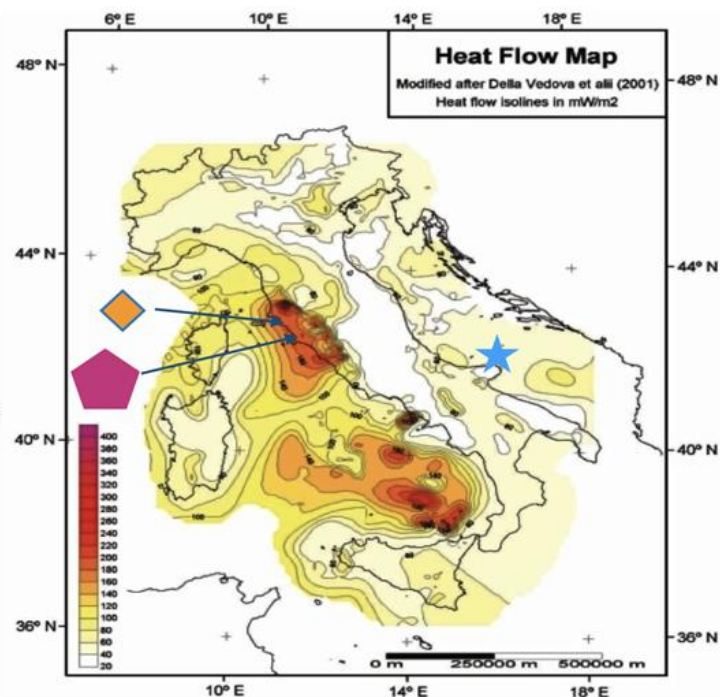


Figure 34: Heat flow map of Italy, illustrating the different conditions in the Peninsula. The location of the study areas is indicated.

Geological conditions

The Italian sites (Gavorrano, Monte Amiata, and Gargano) are in the inner Northern Apennines and in the foreland of the southern Apennines (Figure 35).

The Apennine Belt is a NE/E-verging Alpine belt that experienced convergence and collisional processes after the closure of the Ligurian Ocean (Cretaceous-early Miocene). The collision gave rise to the superimposition of different tectonic units forming the Northern Apennines. From the top, the units are (Carmignani et al., 1994): (a) the Ligurian Units, derived from the Ligurian-Piedmont Domain, and consisting of remnants of Jurassic oceanic crust and its late Jurassic-Cretaceous, mainly clayey, sedimentary cover; (b) the Sub-Ligurian Units (Sub-Ligurian Domain), made up of Cretaceous-Oligocene turbidites; (c) the Tuscan Units forming a duplex system and composed of HP metamorphic and sedimentary units ranging from Palaeozoic to early Miocene in age (Carmignani et al., 1994; Rossetti et al., 2002; Brogi and Giorgetti, 2012).

After the collisional event, Inner Northern Apennines was affected by extensional tectonics since the early-middle Miocene (Carmignani et al., 1994). One of the clearest indications of the collisional process is given by high-pressure metamorphism (up to 1.5 GPa, Bianco et al., 2019) developed during the eastward stacking of the tectonic units deriving from the oceanic (Ligurian units, Auctt.), transitional (Sub-Ligurian units, Auctt.) and continental (Tuscan Nappe, Auctt.) paleogeographic domains of Northern Apennines (Molli, 2008). The subsequent eastward migration of the extensional tectonics resulted in: (a) Miocene lateral segmentation of the previously stacked units (Brogi et al., 2005; Brogi and Liotta, 2008); (b) development of Pliocene-Quaternary NW-striking normal faults cross-cutting all the previous structures and inducing NW-trending tectonic depressions, filled by continental and marine sediments (Martini and Sagri, 1993;).

The primary evidence of extension is the opening of the Tyrrhenian Basin (Bartole, 1995) and the present crustal and lithospheric thickness of about 20 and 40 km (about 24.85 mi), respectively (Di Stefano et al., 2011; Moeller et al., 2013). At least since the Langhian, extension was accompanied by eastward migrating magmatism (Serri et al., 1993), affecting the Tuscan archipelago and the inland inner Northern Apennines (Dini et al., 2005, 2008) (Figure 36). Magmas were emplaced at shallow crustal levels (mainly at 6–8 km depth; Serri et al., 1993) mostly along the NE-striking brittle shear zones (Dini et al., 2008; Spiess et al., 2021), which played the role of transfer zones in the inner Northern Apennines (Liotta, 1991; Dini et al., 2008) and lateral ramps in the outer Northern Apennines (Liotta, 1991), where coeval compression occurred (Elter et al., 1975).

Currently, no active volcanoes are present in Tuscany although heat flux is 120 mW/m² on average (Pauselli et al., 2019). However, local peaks up to 1000 mW/m² were estimated in the Larderello geothermal area (Gola et al., 2017), which is located along one of the most relevant transfer zones crossing the Northern Apennines (Fig. 1a). The geothermal fluid flow is particularly active (Gola et al., 2017; Rochira et al., 2018; Liotta and Brogi, 2020), contributing to determine the bulk of the electricity production in Italy from the Larderello and Monte Amiata geothermal fields (Romagnoli et al., 2010). Information from deeper structural levels derives from deep boreholes drilled during geothermal exploration and exploitation (Romagnoli et al., 2010), and interpretation of reflection seismic lines. These latter display a high-impedance seismic reflector, named *K-horizon* ranging in depth between 3 and 7 km, and considered as an active shear zone, located at the top of the brittle-ductile transition (Liotta and Ranalli, 1999), possibly hosting fluids at supercritical conditions (Agostinetti et al., 2017). The *K-horizon* shows a dome-shaped culmination in both Larderello and Monte Amiata areas.

The foreland of the southern Apennines is mainly represented by carbonate successions (Apulia carbonate platform) deposited on the Adria margin (Ricchetti et al., 1988). The carbonate succession was drilled by a few deep boreholes for oil and gas exploration. It consists of Late Triassic evaporite overlain by 3–6 km thick Mesozoic carbonate rocks, in turn, overlain by Tertiary terrigenous-carbonate succession. In the Gargano promontory, the whole succession is deformed by folds and faults, with some of the latter still active.

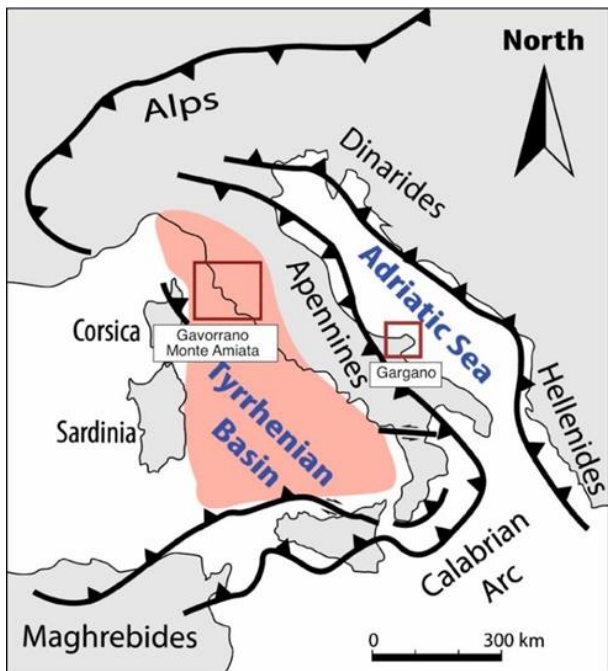


Figure 35: Schematic structural sketch map of Italy and its surroundings, showing the main axial trends of the Alpine chains; the locations of the case studies are highlighted.

Pilot sites data and integration analysis B Late Oligocene - Early Miocene

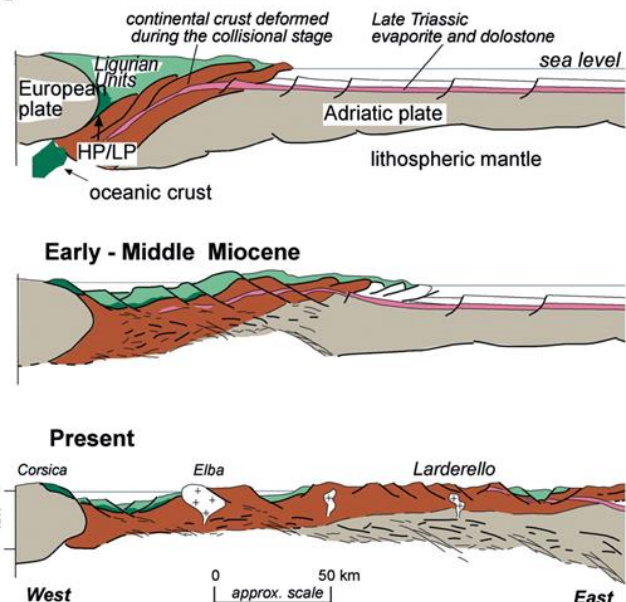


Figure 36: Schematic structural sections illustrating the evolution of the Northern Apennines since the late Oligocene. Eastward migrating extension has been affecting the inner Northern Apennines zone since Early Middle Miocene, along with coeval magmatism.

Gavorrano site

The Gavorrano area comprehends a pyrite mining area, mainly exploited at the end of the nineteenth century and the last decades of the twentieth century. The activity produced about 25 million tons of pyrite and other sulfides (chalcopyrite, fluorite, marcasite, barite, realgar, and stibnite). The mineralization was associated with a geothermal system related to the emplacement and cooling of a Pliocene felsic magmatic body (Gavorrano pluton) which intruded the continental succession made up of Palaeozoic-Triassic quartzite and phyllite, Triassic metacarbonate and late Triassic evaporite. The Gavorrano pluton is partially exposed and has a maximum length of 3 km, a width of 1.7 km and an estimated maximum thickness of 0.7 km. It is a porphyritic quartz-monzonite, crossed by tourmaline-rich microgranite and aplitic dykes (Figure 37).

The depth of the granite emplacement was reckoned at about 4-5 km. The exhumation of the Gavorrano granite was controlled by polyphase normal faults. The main faults show an NNW-SSE orientation and delimit the western and eastern margins of the pluton. Normal faults juxtaposed the Jurassic-Cretaceous carbonate of the Tuscan Nappe with the granite, giving rise to damaged rock volumes controlled by the fault geometries and kinematics (Brogi et al., 2021).

Mining exploration data permitted to reconstruct of the heat flow local peak and the expected temperature at 1000 m depth below sea level (Figure 38)

Hydrothermal circulation is still active in the Gavorrano area. Thermal springs were active before the mining activity and thermal waters have been encountered within the mine tunnels during the exploitation. Hydrothermal fluids within the mine (50 m a.s.l.) display the following features: T= 33°C; pH= 7.10; TDS = 2239 mg/l, Ca = 409 mg/l, Mg= 107 mg/l, Na= 43 mg/l (Minissale, 2004; Garzonio and Affuso, 2004).

The structure of the Gavorrano area is reported in Figure 39 where the mining, now abandoned, boreholes are also indicated. The geological cross-sections display the geometry and the attitude of the main fault zones.

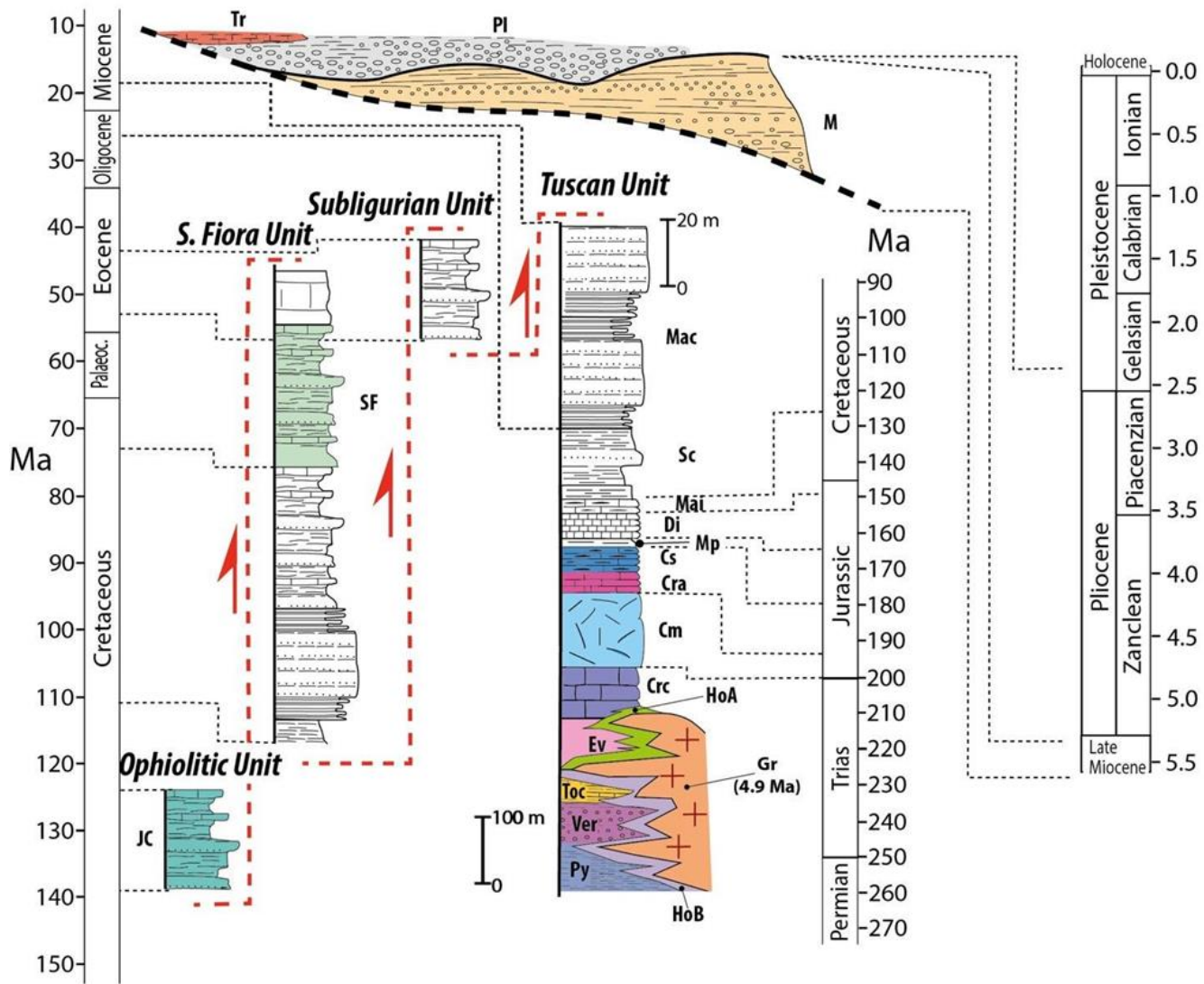


Figure 37: Stratigraphic logs of the tectonic units exposed in the study areas. The successions that are exposed are indicated by colors. Symbols: Tr—continental carbonate consisting of travertine and lacustrine limestone; Ple—fluvio-lacustrine sediments consisting of pebbly sand and sandy clay with interbedded pebble layers; M—Late Messinian polygenic reddish sandy-conglomerate and clay level (Montebamboli conglomerate Autt.); JC—Argille a Palombini Fm: siliceous calcilutite, calcarenite, shale, and marl; SF—Santa Fiora Fm: limestone, sandstone, and shale passing to marl and silty-marl at the top; Mac—Macigno Fm: quartz-feldspar sandstone and shale; Sc—Scaglia Toscana Group: shale, limestone, marl, calcarenite, and biocalciranite; Mai—Maiolica Fm: cherty limestone, calcilutite; Di—Diaspri Fm: radiolarite and shale; Mp—Marne a Posidonia Fm: marl and marly limestone; Cs—Calcare Selcifero Fm: cherty limestone, marl, and shale; Cra—Rosso Ammonitico Fm: reddish nodular limestone and shale; Cm—Calcare Massiccio Fm: massive limestone; Crc—Calcaria a Rhaetavicularia contorta Fm: bedded limestone and marl. Ev—Burano Fm: dolostone and gypsum/anhydrite layers; Toc—Tocchi Fm: metacarbonate and phyllite; Ver—Verrucano Group: quartz-metaconglomerate, metasandstone, and phyllite. Py—Palaeozoic phyllite-quartzite Group: organic-matter bearing phyllite and metasandstone. HoA: carbonate hornfels; Hob: pelitic hornfels; Gr: Gavorrano magmatic complex (After Brogi et al., 2021).

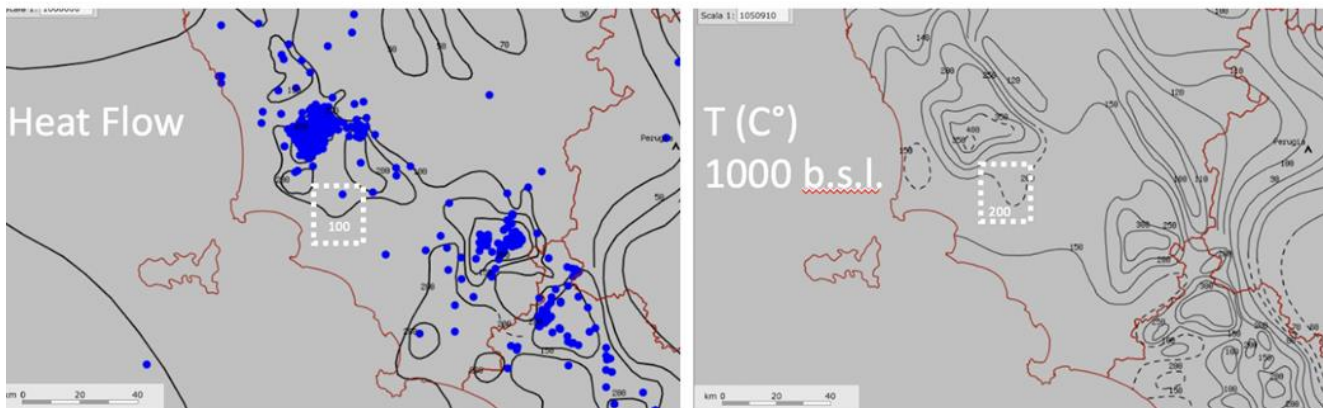


Figure 38: Left: heat flow map (contour lines in mW/m²) in the south-western part of Tuscany, where the Gavorrano and Monte Amiata study areas are respectively located to the north and south (dashed squares); right: estimated temperature at 1 km below sea level in the Gavorrano area (dashed square). Data are from <http://geothopica.igg.cnr.it>.

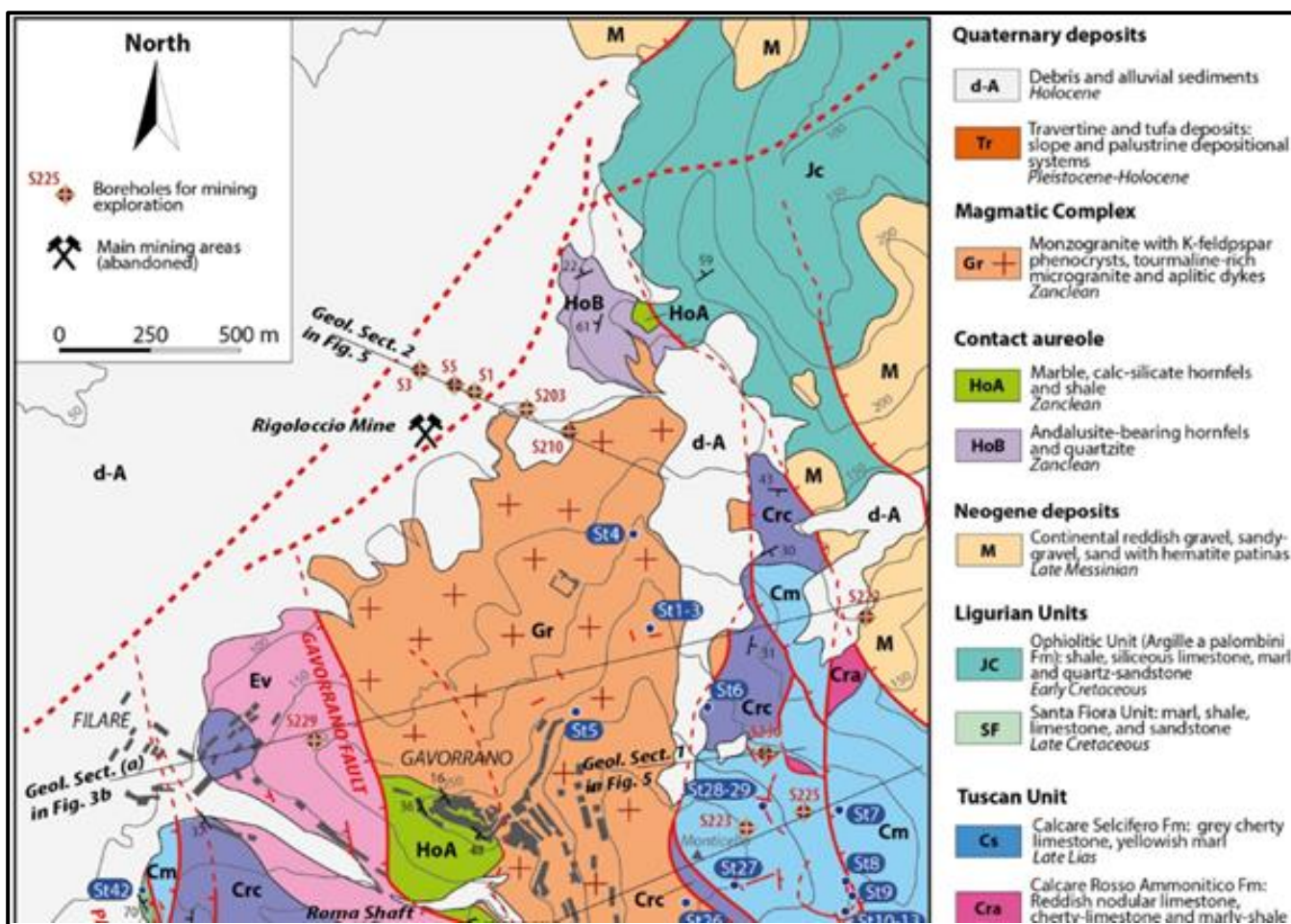


Figure 39: Geological map of the Gavorrano mining district and geological cross sections. Locations of the abandoned mines and boreholes drilled during the mining exploration are also indicated (After Brogi et al., 2021).

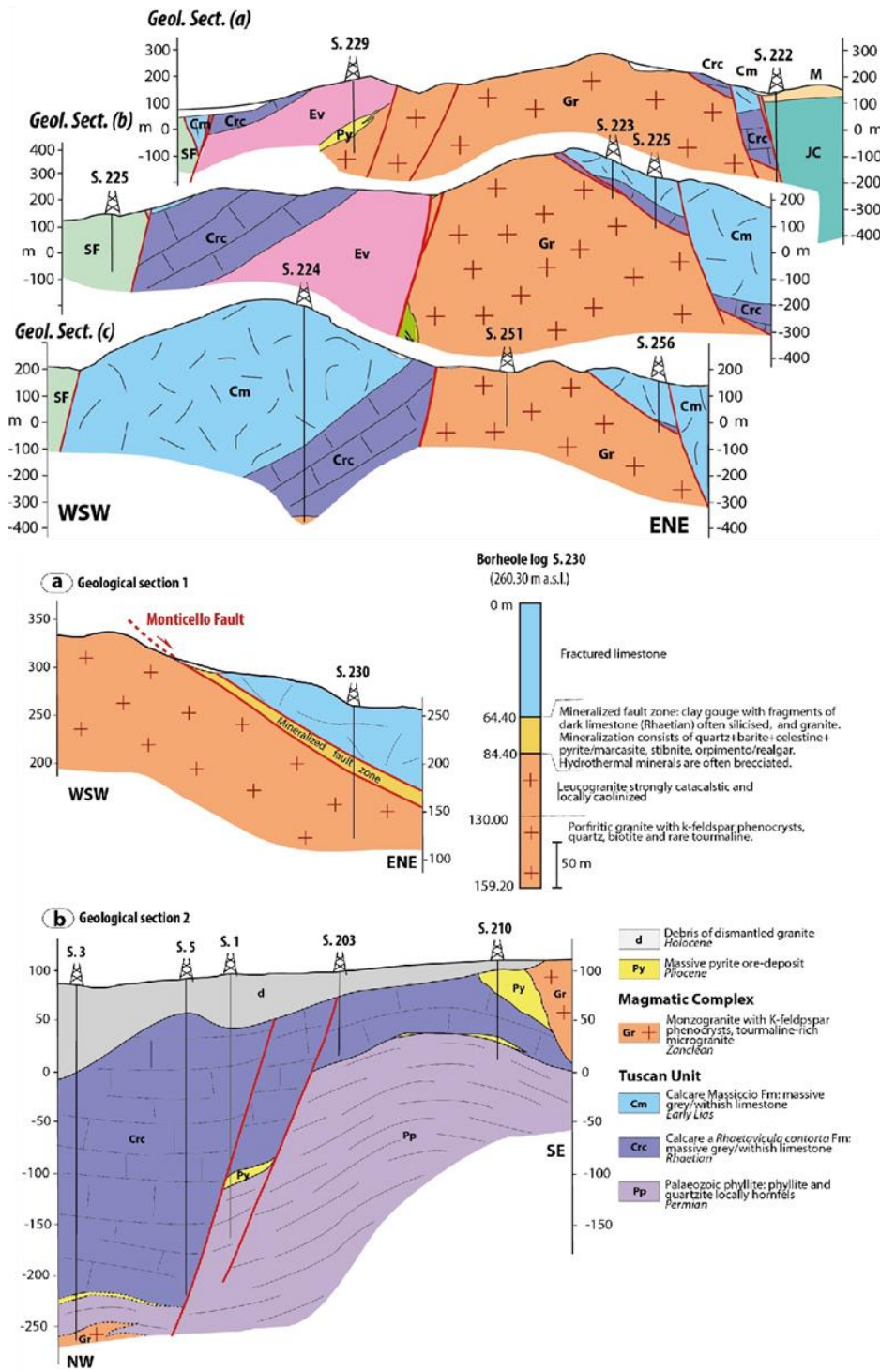


Figure 40: Cross sections of the geological map of the Gavorrano mining district and geological cross sections. Locations of the abandoned mines and boreholes drilled during the mining exploration are also indicated (After Brogi et al., 2021).

Considering borehole S3 as a potential pilot site (Figure 39), the thermal conductivity of the different lithologies is given in

, following Bellani et al. (2005) and Della Vedova et al. (2008). Temperature at 1 km b.s.l is estimated to be about 170°C (Figure 37).

Table 19: Thickness, thermal conductivity, and heat capacity of the lithologies both encountered in S3 borehole and supposed to be, down to 1 km b.s.l.

Lithology	Thickness (m)	Thermal conductivity (W/m°K)	Heat Capacity (MJ/m³K)
Alluvial sediments	100	1.8	2.18
Limestone and dolostone	220	2.5	2.18
Phyllite	60	3	2.18
Granite	200	2.5	2.18
Phyllite	550	2.7 - 3	2.18

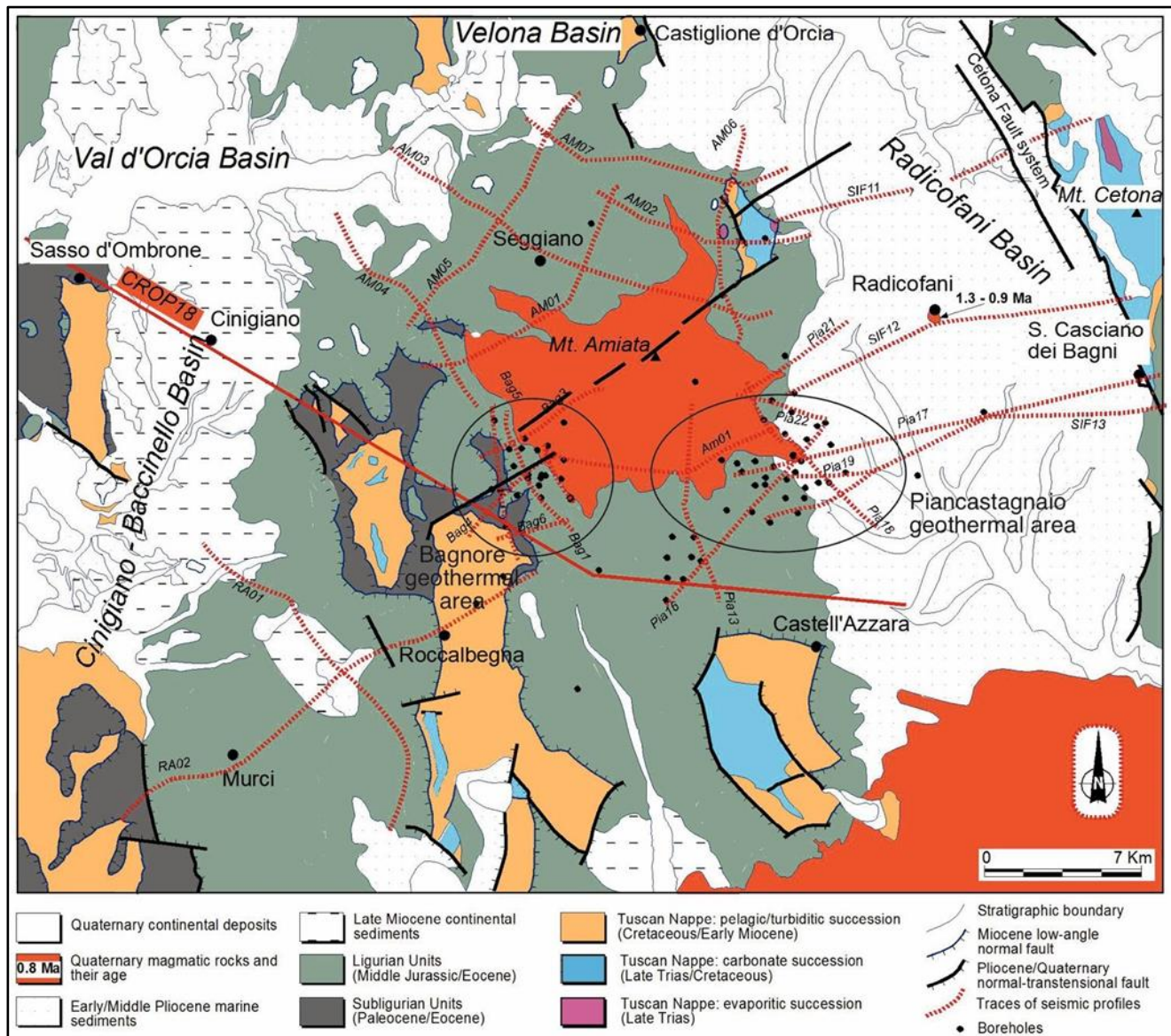


Figure 41: Geological sketch map of the Monte Amiata volcano-geothermal area. Borehole locations indicate the areas exploited for geothermal purposes. The traces of seismic profiles acquired during geothermal and oil and gas exploration are also indicated (after Brogi, 2008).

Monte Amiata site

The Monte Amiata area comprehends a mining area exploited for cinnabar and stibnite from the Etruscan period to the end of the nineteenth century. This hydrothermal mineralization is associated with a Pleistocene geothermal system, still active in the Piancastagnaio and Bagnore areas and where ENEL GreenPower installed power plants for electricity production (Figure 41). The geological setting of the Monte Amiata geothermal area is characterized by the tectonic units of the inner Northern Apennines and by the Neogene sedimentary successions deposited in structural depressions (i.e. basins) formed during the post-collisional evolution (Calamai et al., 1970; Brogi, 2004, 2008; Cadoux and Pinti, 2009; Brogi et al., 2010) (Figure 42):

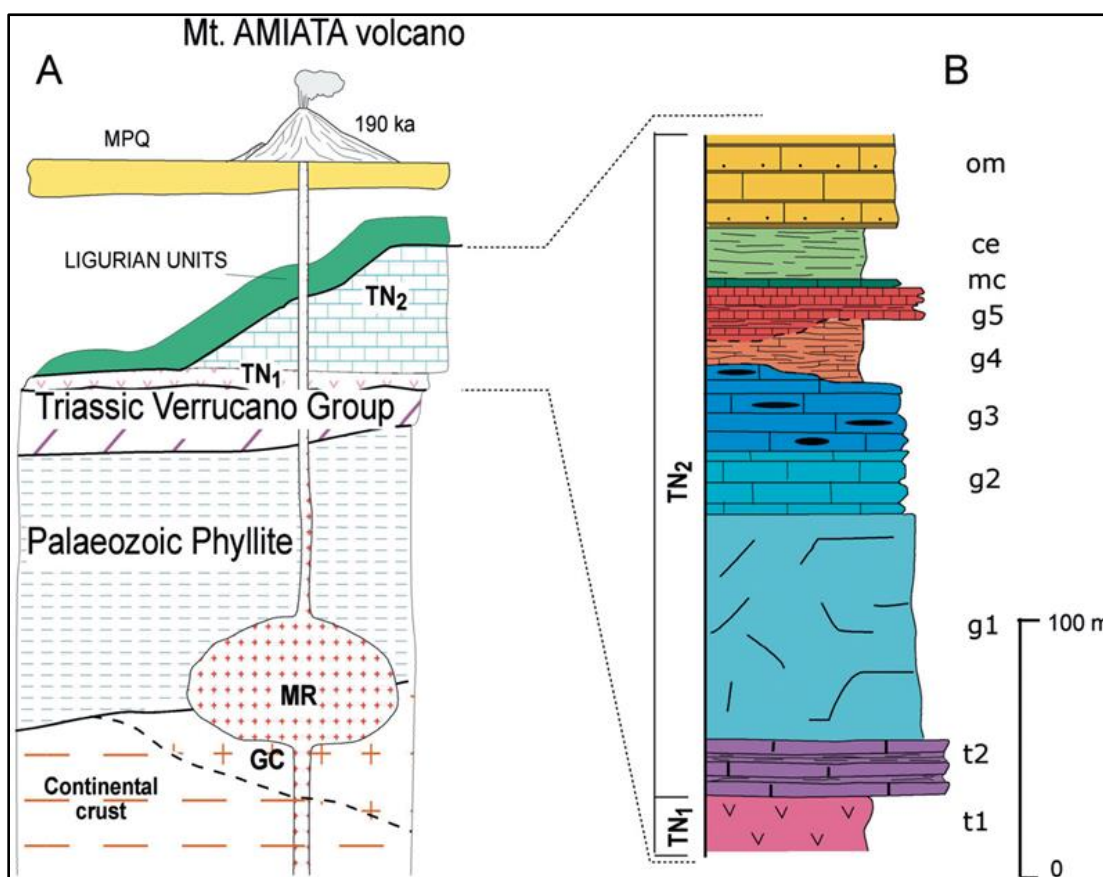


Figure 42: Stratigraphic (A) - Tectonostratigraphic units of the Mt. Amiata area. MPQ: Quaternary, Pliocene and Miocene sediments; MR - Magmatic rocks; Tuscan Nappe(TN): TN₂ - early Miocene-Rhaetian succession; TN₁ - late Triassic evaporite(Burano-Calcare Cavernoso Fm); Gneiss xenolithes have been recognized embedded in the Mt. Amiata Pleistocene lavas, thus suggesting the occurrence of these rocks in the basement (; (B) sketch of the stratigraphic relationships within the Tuscan Nappe in the Monte Amiata area: t₁ - late Triassic evaporite: Norian-Rhaetian gypsum and dolostone (Burano-Calcare Cavernoso Fm); t₂ - Rhaetian dark limestone and marl (Calcare e Marne a Rhaetavicula contorta Fm); g₁ - early Lias massive limestone (Calcare Massiccio Fm); g₂ - middle Lias red nodular limestone (Rosso Ammonitico Fm); g₃ - late Lias cherty limestone (Calcare Selcifero Fm); g₄ - Dogger marl and marly limestone (Marne a Posidonia Fm); g₅ – Malm radiolarite (Diaspi Fm); mc – Cretaceous cherty limestone (Maiolica Fm) ce - Cretaceous-Oligocene shale, marl and calcarenite (Scaglia Toscana Fm); late Oligocene-early Miocene sandstone and shale (Macigno Fm) (After Brogi et al., 2015).

The tectonic units were piled up and deformed by compressional structures during the collisional event of the Northern Apennines (Late Oligocene-Early Miocene) and by normal, strike-slip and oblique-slip faults during the Neogene-Quaternary post-collisional extensional tectonics. This latter process gave rise to superposed extensional fault systems and associated transfer zones, mainly active during the Miocene-Quaternary period.

The first extensional event formed normal faults which produced the boudinage of the Tuscan Nappe carbonate and evaporite successions (TN1 and TN2 in Fig. 3.6.8) which resulted in laterally discontinuous bodies separated by areas where the impervious sedimentary cover of the Ligurian Units directly overlies the Late Triassic evaporite and/or metamorphic units: Verrucano Group or Palaeozoic phyllites (Figure 43).

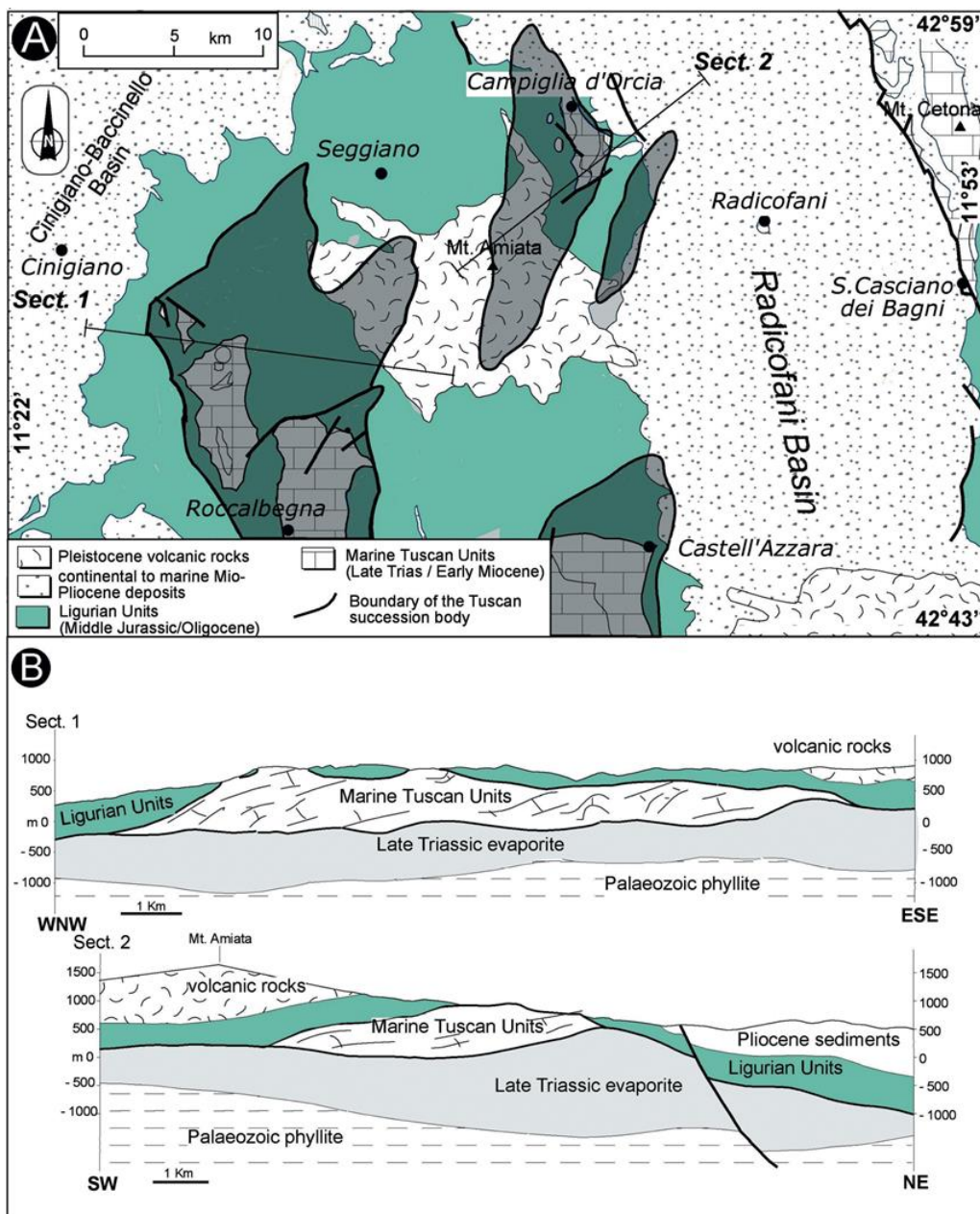


Figure 43: (A) Geological sketch map of the Mt. Amiata volcanic complex and its surroundings highlighting the location of the laterally segmented Tuscan Nappe carbonate succession. The bulk of the Pliocene faults affecting the Ligurides and Tuscan

succession have been omitted for sake of clarity. The buried boundaries of the Tuscan Nappe boudins (in dark gray) were reconstructed by integrating geothermal boreholes and reflection seismic lines; (B) Geological cross-sections through the Mt Amiata area (after Brogi et alii, 2010, modified).

The thinned tectonic pile was later affected by NW-striking high-angle normal faults delimiting the Neogene sedimentary infills of the peripheral structural depressions and by NE- striking strike- to oblique-slip faults which controlled both the volcanism and the geothermal fluid flow. Geothermal activity in the Piancastagnaio and Bagnore areas exploits two main geothermal reservoirs, located at different depths: The shallowest (500-1000 m below sea level), hosted in Mesozoic carbonate and evaporite rocks which exploit fluids at $T = 150 - 200$ °C and $P = 30$ bar. The Deepest (2500-4000 m below sea level), hosted in Paleozoic metamorphic rocks (mainly phyllite) exploits fluids at $T= 300-350$ °C and $P = 200-250$ bar. Mining and geothermal exploration allowed the reconstruction of a local peak in the heat flow and temperature at 1000 m depth below sea level as indicated in Figure 44.

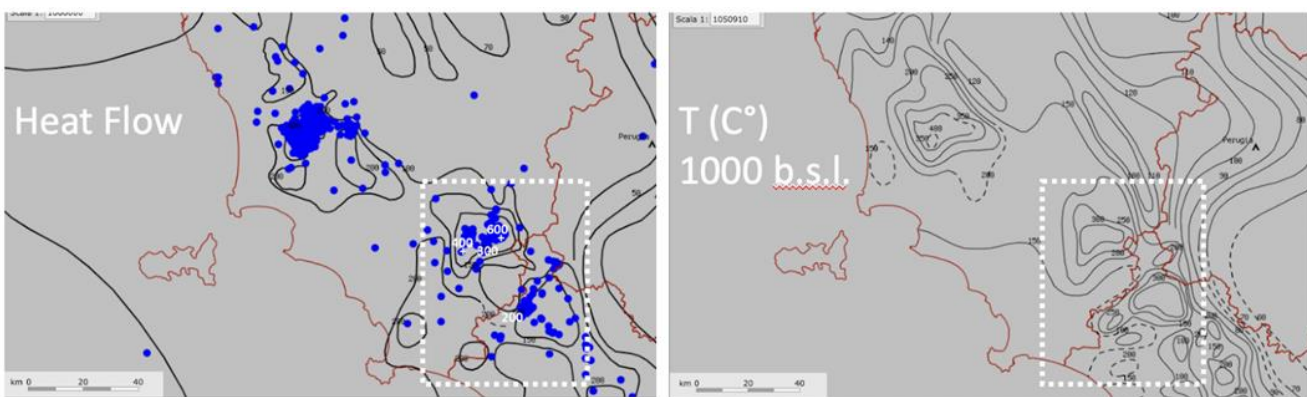


Figure 44: Left: heat flow map (contour lines in mW/m^2) in the south-western part of Tuscany, where the Monte Amiata study area is located (dashed square); right: estimated temperature at 1 km below sea level in the Gavorrano area (dashed square). Data from <http://geothopica.igg.cnr.it/>.

Geothermal fluids flowing at the surface from the thermal springs localized in restricted areas have the following features: $T = 52$ °C; $\text{pH}= 6.50$; $\text{TDS} = 4128 \text{ mg/l}$; $\text{Ca} = 798 \text{ mg/l}$; $\text{Mg} = 182 \text{ mg/l}$; $\text{Na} = 28 \text{ mg/l}$.

Considering borehole Poggio Nibbio 8 as a potential pilot site (Figure 45), the thermal conductivity of the different lithologies is given in

, following Bellani et al. (2005) and Della Vedova et al. (2008). Temperature at 1 km b.s.l is estimated to be around 200°C.

Table 20: Thickness, thermal conductivity, and heat capacity of the lithologies both encountered in the abandoned Poggio Nibbio borehole.

Lithology	Thickness (m)	Thermal conductivity (W/mK)	Heat Capacity (MJ/m³K)
Ophiolitic Units	600	2.1	2.18
Evaporite	300	4.18	2.18
Quartzite	350	2.7	2.18
Phyllite	1500	2.7 - 3	2.18



Figure 45: Simplified stratigraphic logs of the indicated geothermal boreholes drilled for geothermal purposes. Some of these are feeding the geothermal power plants of ENEL GreenPower (BG20, BG25, BG3bis, and BG13) whereas the Poggio Nibbio borehole (PN8) is not currently used (from Brogi, 2008).

Gargano site

The Gargano area is located in the Apulia region (southern Italy), which is part of the present foreland of both the NE-vergent southern Apennines and the SW-vergent Dinarides, both tectonically active during the Neogene. It is dominantly characterized by the almost 6 km thick Mesozoic platform belonging to the Adria microplate (Figure 25 and Figure 46).

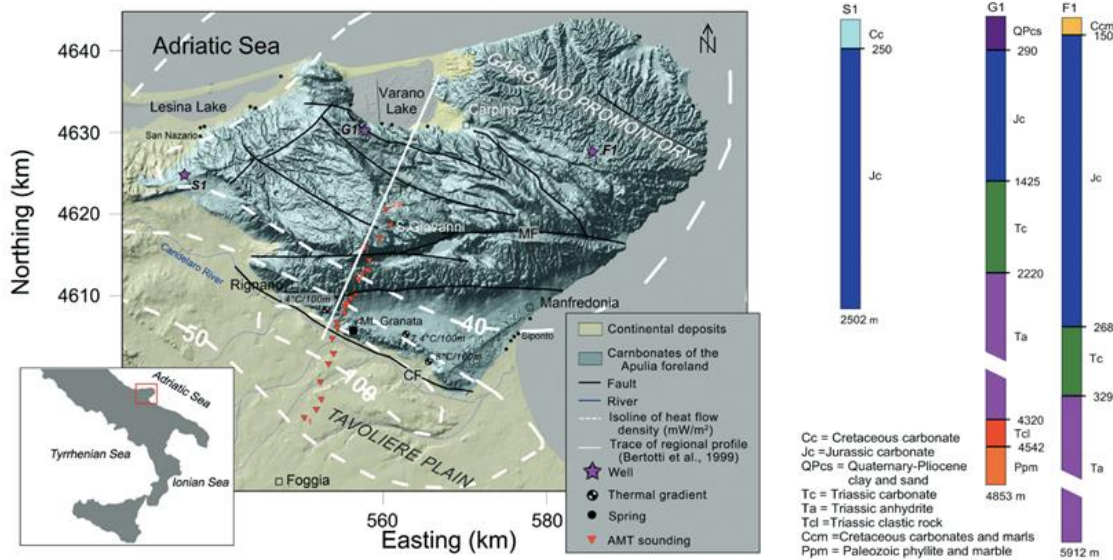


Figure 46: Left: schematic structural map of the Gargano area, indicating the location of the measured geothermal gradients and (right:) of the main boreholes drilled in the area (after Tripaldi, 2020).

The Late Triassic – Cretaceous carbonate succession is deformed by W-E and NW-SE striking normal and strike-to oblique-slip faults, some of which are characterized by off-sets exceeding several hundred meters. The Gargano promontory and the surroundings were explored for oil and gas during the 70s and 80s. Deep boreholes down to 5000 m, as well as shallower wells drilled for water supply, allowed to reconstruct of the heat flow and temperature distribution at 1000 m depth below sea level, as indicated in Figure 47.

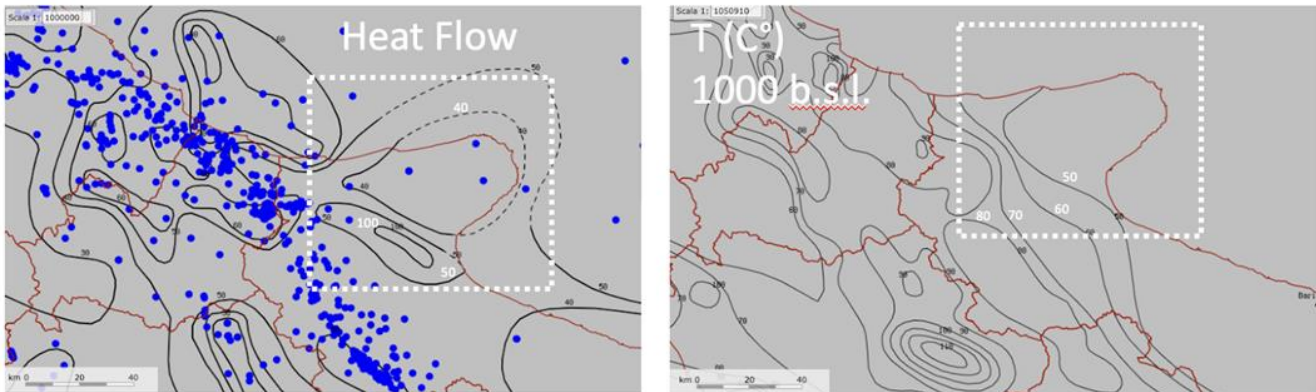


Figure 47: Left: heat flow map (contour lines in mW/m^2) in the Italian south-eastern coast. The study area is indicated by the dashed square; right: estimated temperature at 1 km below sea level in the Gargano area (dashed square). Data from <http://geothopica.igg.cnr.it/>.

Faults are affected by a significant damage zone (Larsen et al., 2010), favoring permeability and circulation of fluids. This results in localized modest thermal springs where temperatures are in the range 22-27°C although surficial (< 200m) boreholes locally encounter fluids at about 40°C (Pagliarulo, 1996). The area is seismically active (Filippucci et al., 2019). Parameters related to rock thermal properties are here below summarized (**Error! Reference source not found.**), down to 1000 m b.s.l., where the expected temperature is about 40-50°C.

Table 21: Thickness and thermal conductivity of the lithologies characterizing the Gargano area (after Filippucci et al., 2019)

Lithology	Thickness (m)	Thermal conductivity (W/m°K)
Alluvial sediments	100	1.8
Limestone and dolostone	1000	2

Past/Current/future above ground energy system

Gavorrano site

The Gavorrano geothermal area is located on the hills close to Follonica, a small town on the Tuscan coast. Between the geothermal area and the coast, there are multiple locations, shown in Figure 48, characterized by a substantial heat demand.

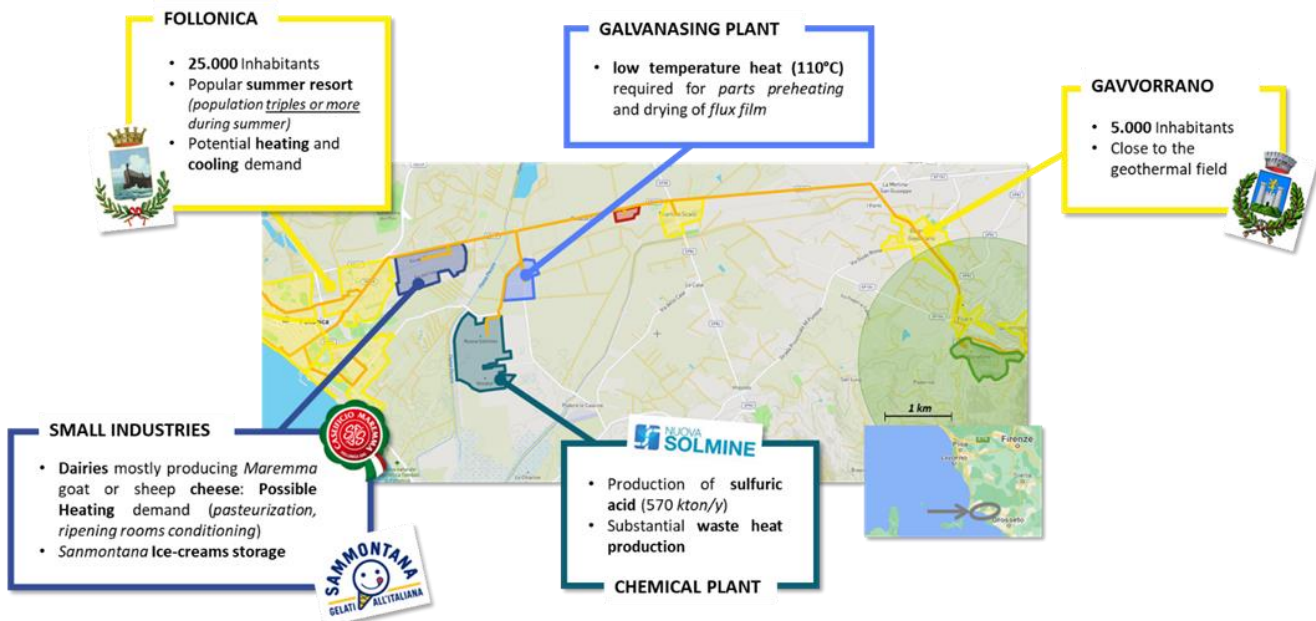


Figure 48: Possible DH network connecting the Gavorrano geothermal area with Follonica. Highlighted in the map are: the geothermal field (in green – in dark green are the abandoned mines that originated the geological study (Brogi et al., 2021)), residential areas (in yellow), a shopping center (in red), industrial areas (in different blue scales): small business including some dairies (Violet), galvanizing plant and other manufactories (Light Blue), a chemical hub containing the Nuova Solmine Plant (Dark Blue). In orange, a possible DH network fueled both by the geothermal wells and by the chemical plant waste heat

Alternative Heat Sources - Nuova Solmine Chemical Plant

An important industrial area is located 8 km away from the geothermal area containing the Nuova Solmine chemical plant. According to a company report (Gruppo Sol.mar, 2020), in 2020 the plant has produced 500 kton of sulphuric acid and 70 kton of oleum (fuming sulphuric acid) starting from 180 kton of sulfur. The sulphuric acid production process generates a large amount of heat, mainly during the initial combustion of the sulfur to produce sulfur dioxide.

The company is already utilizing this heat for power generation through a steam turbine and is planning to install an ORC and a district heating network to serve the surrounding residential areas (Gruppo Sol.mar, 2020). The net electric power production in 2020 was 93.6 GWh.

Given the fact that the heat produced by the plant will not be sufficient to cover the overall demand in the area, integration with the geothermal resource can be an interesting solution, especially considering the possible installation of a district heating network in the next future.

Possible Heat Uses - Residential Heating Demands

Between the geothermal area and Follonica there are different small villages, highlighted in yellow in the map in Figure 48, the heating demand of each area has been estimated considering the population and the heating degree-days of the site. In the table below are reported the estimated heating request.

Table 22: Estimated overall residential heating consumption - Gavorrano area.

Village	Distance [km]	HDD [°C/day]	Population [-]	Consumption [GWh/y]	Power [MW]
Gavorrano	1	1748	1,000	2.82	1.49
Bagni di Gavorrano	1.7	1748	3,000	8.47	4.46
Scarlino Scalo	5.2	1840	1,230	3.61	1.90
Follonica	12.1	1527	20,000	50.88	26.78
<i>Total</i>	12.1	1577.3	25230	65.79	34.62

The heating demand has been estimated considering the limited energy performance index of the building (EP_{li} as defined by the Italian legislation (D.M. 26.6.2009, n. 158)). This value represents the maximum annual consumption allowed per square meter of residential buildings by the Italian legislation and is a function of the heating degree-days (HDD) and of the shape factor (S_f) of the building. The annual consumption has been then estimated from the population of the area using the following formula:

$$Q_{tot} = 1.5 EP_{li}(HDD, S_f) Pop \frac{m^2}{ab}. \quad (3.6.1)$$

For S_f and $m^2/ab.$ standard Italian values have been considered ($s_f = 0.6$, $m^2/ab. = 33$). A 1.5 correction factor has been used as unfortunately many Italian buildings still do not comply with the legislation because they have been built before the law came into force in 2010.

The presented results are in line with the consumption of the existing DH network in Tuscany (Ungar et al., 2022) in terms of MWh/y per housing unit. The network power has been estimated rescaling the data presented in Ungar et al., (2022).

Possible Heat Uses – Summer Cooling demand

The population of the Follonica area increases significantly in summer as it is a typical summer holiday destination. For this reason, an important cold request is expected in the area. The estimation has been performed considering the same assumption used for the heating case but considering a tripled population to account for the summer tourist flux.

Table 23: Estimated overall residential cooling consumption - Gavorrano area

Village	Distance [km]	Population [-]	Consumption [GWh/y]	Power [MW]
Gavorrano	1	3,000	3.00	6.00
Bagni di Gavorrano	1.7	9,000	9.00	18.00
Scarlino Scalo	5.2	3,690	3.69	7.38
Follonica	12.1	60,000	60.00	120.00
Total	12.1	75690	75.69	151.38

Possible Heat Uses – Supermarkets

In the area, there are 11 main supermarkets for a total floor area of 17000 m², roughly evaluated using google maps. The consumptions have been estimated using some data presented in literature for which the annual power consumption of a supermarket is roughly 600 kWh/(m²y) (Kolokotroni et al., 2019).

Of the overall power consumption, around 50% is used for refrigeration while 30% is for space heating (Kolokotroni et al., 2019). A COP of 2 has been considered for the estimation of the thermal needs for cooling (Ghanbarpour et al., 2021).

Table 24: Estimated overall supermarkets consumption - Gavorrano area

Village	Supermarket	Surface	Consumption	
	Number	[m ²]	Heating [GWh/t]	Cooling [GWh/y]
Gavorrano	1	100	0.01	0.03
Bagni di Gavorrano	1	2,000	0.36	1.2
Scarlino Scalo	1	900	0.16	0.54
Follonica	8	14,150	2.55	8.49
Total	11	17100	3.08	10.26

Possible Heat Uses - Industrial Activities

Multiple industrial activities in the area have heating requirements. In an industrial area 3 km from the Follonica city center (violet in figure x) there are three dairies, mostly producing Maremma goat or sheep cheese.

According to literature (Chinese et al. (2022)) a comparable Sardinian cheese factory requires 0.28 kWh of heat per kg of processed milk. The heat is required in the form of hot water with temperature ranging between 70°C and 95°C for pasteurization, cleaning, ricotta production, and for maintaining ripening rooms conditions after maintenance or cheese replacement (Chinese et al., 2022).

The amount of milk processed is still unknown but, as a reference, the Sardinian case study, which seems comparable in size with the biggest dairies in the industrial area, requires 3.77 GWh/y of heat with an average power of 327.8 kWt (Chinese et al., 2022).

A branch of the Sammontana group (Italian ice cream producer) is present in the same industrial hub, for which significant refrigeration needs are expected in summer.

A further heat-demanding activity is a galvanizing plant located close to the chemical factory (Light Blue in Figure 48) which requires low-temperature heat (110°C) for parts preheating and for drying the film of flux needed for the galvanization process. High-temperature heat (450°C), which cannot be easily provided through geothermal wells, is also required for melting the zinc.

Monte Amiata site

The Monte Amiata site is located close to an important geothermal field which has been exploited in the past decades and yet currently for power production purposes. Excluding the geothermal power plant, the surrounding area is sparsely populated, with a reduced number of industrial activities.

As shown on Figure 49, the only relevant industry nearby is *Floramiata*, an agricultural company specialized in the production of indoor plants, which manages 200,000 m² of greenhouses heated up with the waste heat from a nearby geothermal power plant. *Floramiata* average heat consumption is 114 GWh per year. Because of previous research committed, UNIFI has got the *Floramiata* consumption data for the period 2017 – 2020 on a 10-mins basis.

Considering the lack of other interesting heat-demanding activities and the availability of the consumption data, it can be interesting to analyze the behavior of the alternative HOCLOOP system in this specific context, by comparing the techno economic results with those of the existing flash geothermal powerplants, which currently deliver the required heat to *Floramiata* company.

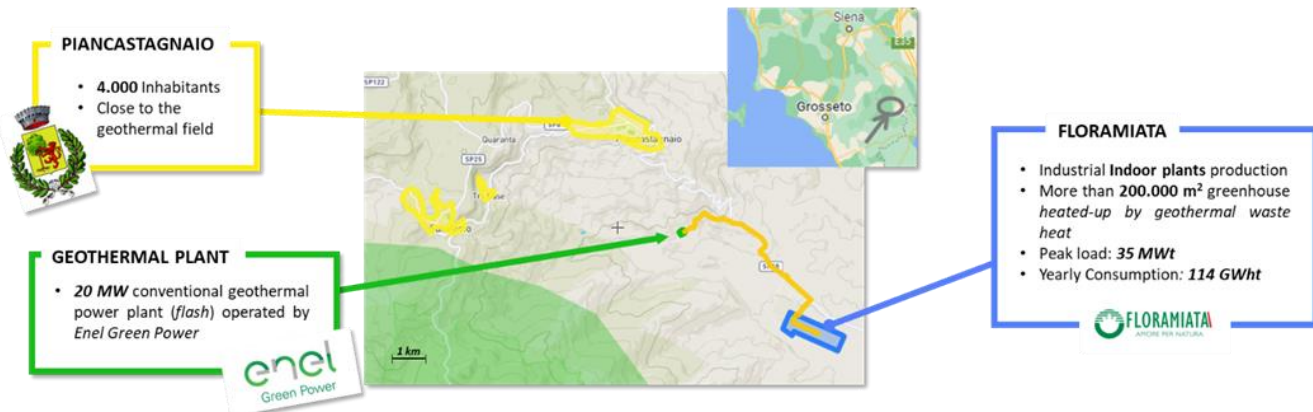


Figure 49: Existing activities in the monte Amiata Area. Highlighted in the map are: the targeted geothermal field (in green), residential areas (in yellow), Floramiata industrial area (in blue), and Conventional geothermal power plant (in dark green). In orange is an existing DH network that provides residual heat from the geothermal power plant to Floramiata.

Gargano site

In the Gargano site, the targeted geothermal reservoir is located close to Manfredonia, a city in northern Puglia. The city has 50,000 inhabitants, hence, despite the required heating demand is generally lower due to the higher temperatures in southern Italy, about 130 GWh are needed for residential heating purposes. Moreover, a relevant cooling demand is expected in the summer period. The heat demand assessment has been done, following the same methodology described for the Gavorrano case.



Figure 50: Existing activities in the monte Gargano Area. Highlighted in the map are: the targeted geothermal field (in green), residential areas (in yellow), Flat glass production plant (in blue), and Industrial fish market (in violet).

As shown in Figure 50, the main industrial activities in the area are a flat glass production plant, which potentially produces a significant amount of waste heat, and the industrial fish market where the catch unloaded by the fishing vessels of the area is sold. The fish market is of special interest, because of its peculiarity and the amount of power needed for refrigeration.

Final Remarks on the HOCLOOP Proposal in the Italian case studies DH Networks

For both the Gavorrano and Gargano cases, the use of HOCLOOP technology is expected for heating and cooling applications. For this reason, the simulation process requires knowledge of the heat demand of the foreseen district heating network fueled by the geothermal well.

To provide such data, UNIFI will rescale the heating and cooling demand profile of a real district heating network settled in Calenzano, a small city near Florence, to match the predicted yearly thermal energy consumption of the selected area. The heat provided or required by the industrial district will be then added to the estimated demand, to identify the overall heat load of the well.

In this regard, although not directly related to the scope of the project, it is important to remark that different designs and working fluids of the district heating network considered in the area may result in different heat demand profiles.

Thanks to ongoing studies in this field (Ungar et al., 2022), UNIFI can provide rescaled heat demand profiles for both standard water-based high-temperature DH network that uses heat absorbers for summer operation (Figure 51.a) and low-temperature CO₂-based temperature that uses heat pumps for both summer and winter operations (Figure 51.b).

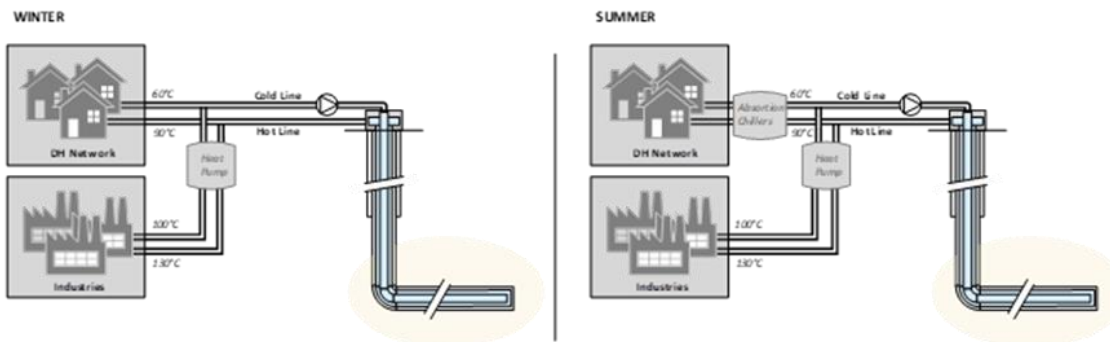
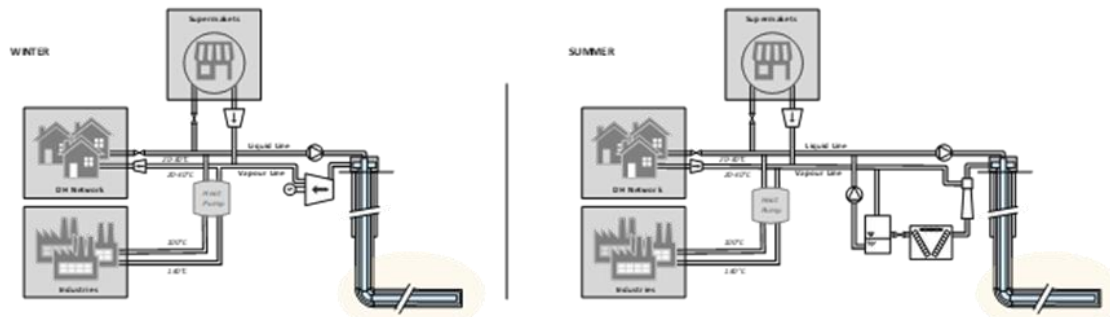
a)

b)


Figure 51: a) water-based DH network installed in Calenzano (Florence) b) Possible CO₂-based DH network as proposed for Calenzano (Florence) in (Ungar et al., 2022).

Summary table

Parameter	Value			Unit			
	Gavorrano	Amiata	Gargano				
Geological information							
Targeted rocks depth *	<i>To be optimized</i>			m			
Temperature at the top of the reservoir *	<i>To be optimized</i>			°C			
Type of reservoir	Fractured						
If fractured, fracture distribution type	Localized shear zones						
Hydraulic properties							
Permeability of the reservoir	1E-14 – 1E-15			m ²			
Regional flow	<i>To be determined</i>						
Thermal properties							
Thermal conductivity (in reservoir)	1.8-3			W/m.K			
Geothermal gradient	70	100	35	°C/km			
Thermal Capacity (reservoir rock)	0.83			J/g/K			
Geothermal loop *							
Heat transportation network							
Supply temperature (water-based network)	70 – 90			°C			
Supply temperature (CO ₂ -based network)	30 (saturated liquid – saturated vapor)			°C			
Heat Demand	TBD**	35	TBD**	MWt			

* Parameters and geometry to be identified and optimized during the project.

5. Conclusions

5.1 Challenges

The data availability varies from case study to case study. Data availability, either of the subsurface properties or of the surface demand, is one of the challenges faced while collecting information on the different pilot sites. In addition, the degree of uncertainty in the data varies largely from one site to another. This will have an impact on the uncertainty of outcomes of the modelling that is foreseen in following tasks.

The Balmatt site has the largest dataset on subsurface properties. This is the result of geophysical logs run in the three deep boreholes that have been drilled at this location, analyses on cuttings, scales and water samples, and to the knowledge that has been acquired over the last years of its development. For this site, all necessary data of the underground is available for a conceptual design of a HOCLOOP installation and for the simulation of the thermal power and output temperature of system.

At the Darmstadt site, 3 wells have been drilled into the geothermal target recently. Further characterization of the target is ongoing. Therefore, some data is not yet available, but further tests are planned. For examples, the thermal properties will be determined by an enhanced thermal response test that will be performed in the coming months. The geological model at this location will also be finalized in the coming months and the groundwater model will be updated. Petrophysical parameters for units without sufficient sample coverage (Permian basalts) will be measured.

For the Paris basin, data about the target formation is available from 49 existing geothermal projects and advanced basin modelling. The site of Fresnes has been selected as a case study because of presence of the different aquifers, the availability of the data, and the large need for renewable heat and cold at the surface. Information about the thermal conductivity of the different lithologies is limited and comes with a large uncertainty because no direct data is available. The values proposed in this report result from modelling exercises. In the absence of data, no calibration on existing data has been carried out.

In Italy, 3 case studies have been selected: The first case study, Gargano, is situated in southeastern Italy, and is characterized of low heat flux of about 40 mW/m². The area is rich in geophysical and boreholes information, permitting integration with data collected at the surface (fracture distribution and lithology) and providing the dataset for evaluating the potential location of the HOCLOOP technology through modeling. The second and third case, Gavorrano and Monte Amiata, are situated in west-central Italy, in areas with a high heat flux of about 70 mW/m² and higher. The Gavorrano is located to an old mining site, providing essential geological data for the evaluation of a HOCLOOP system. Monte Amiata is an active geothermal field.

For the two pilot sites, where geothermal plants are in place (Balmatt case in Belgium) or under the last phase of development (Darmstadt case in Germany), a description of the existing plant, peripherals and district heating grid as it is currently or as it will be constructed is available. At Balmatt, the main future challenges are the optimal integration of the HOCLOOP technology with the existing geothermal loop, the control of both sources for combined heat and power delivery, and the impact of the HOCLOOP solution on the stress conditions within the targeted limestones. For Darmstadt integration of HOCLOOP with within the district heating system or with a single building is judged to be relatively easy. Here, the main technical challenges will be related to the complex geology.

5.2 Recommendations

For the modelling exercise that will be performed in T4.2, if site data is not available, literature data presented in this deliverable can be used. This deliverable highlights the site-specific data that is still missing at the start of the project and that should be acquired to enable the realistic design of the HOCLOOP concept. The summary table that is presented for the different sites should be updated during the course of the project when additional data becomes available.

6. References

- Agostinetti, N.P., Licciardi, A., Piccinini, D., Mazzarini, F., Musumeci, G., Saccorotti, G., Chiarabba, C., 2017. Discovering geothermal supercritical fluids: a new frontier for seismic exploration. *Sci. Rep.* 7, 1–9.
- Al-Malabeh A, Kempe S. Petrolithology of the Permian melaphyre lavas, Darmstadt. Germany Njgpa. 2009;252(2):129–43. <https://doi.org/10.1127/0077-7749/2009/0252-0129>.
- Aretz A, Bär K, Götz AE, Sass I. Outcrop analogue study of Permocarboniferous geothermal sandstone reservoir formations (northern Upper Rhine Graben, Germany): impact of mineral content, depositional environment and diagenesis on petrophysical properties. *Geol Rundsch.* 2016;105(5):1431–52. <https://doi.org/10.1007/s00531-015-1263-2>.
- Backhaus E. Die randliche “Rotliegend”-Fazies und die Paläogeographie des Zechsteins im Bereich des nördlichen Odenwalds. Notizblatt Des Hessischen Landesamts Für Bodenforschung. 1965;93:112–40.
- Bär K, Rühaak W, Welsch B, Schulte D, Homuth S, Sass I. Seasonal High Temperature Heat Storage with Medium Deep Borehole Heat Exchangers. *Energy Procedia.* 2015;76:351–60. <https://doi.org/10.1016/j.egypro.2015.07.841>.
- Bartole, R., 1995. The North-Tyrrhenian–northern Apennines post-collisional system: constraints for a geodynamic model. *Terranova* 1, 7–30.
- Batini, F., Brogi, A., Lazzarotto, A., Liotta, D., Pandeli, E., 2003. Geological features of Larderello-Travale and Mt. Amiata geothermal areas (southern Tuscany, Italy), *Episodes*, Vol. 26, no. 3.
- Beccaletto, L.; Hanot, F.; Serrano, O.; Marc, S. 2011. Overview of the subsurface structural pattern of the Paris Basin (France): Insights from the reprocessing and interpretation of regional seismic lines. In *Marine and Petroleum Geology* 28, pp. 861–879.
- Beier M. Urbane Beeinflussung des Grundwassers: Urbane Beeinflussung des Gundwassers: Stoffemissionen und –immissionen am Beispiel Darmstadts [Dissertation]. Darmstadt: Technische Universität Darmstadt; 2008.
- Bianco, C., Godard, G., Halton, A., Brogi, A., Liotta, D., Caggianelli, A., 2019. The lawsonite-glaucophane blueschists of Elba Island (Italy). *Lithos* 348, 105198. <https://doi.org/10.1016/j.lithos.2019.105198>
- Boissavy, C., Henry, L., Genter, A., Pomart, A., Rocher, P. and Schmidlé-Bloch, V., 2019. Geothermal Energy Use, Country Update for France. European geothermal congress 2019.
- Bos., S., Laenen, B., 2017. Development of the first deep geothermal doublet in the Campine Basin of Belgium. *European Geologist Journal* 43 ([Development of the first deep geothermal doublet in the Campine Basin of Belgium - Eurogeologists](#)).
- Brogi, A. 2008 - The structure of the Monte Amiata volcano-geothermal area (Northern Apennines, Italy): Neogene-Quaternary compression versus extension. *Int. J. Earth Sci.*, 97, 677-703.
- Brogi, A. 2008. The Triassic and Palaeozoic successions drilled in the Bagnore geothermal field and Poggio Nibbio area (Monte Amiata, Northern Apennines, Italy). *Boll. Soc. Geol. It.*, 127, 599–613.

- Brogi, A., 2004. Miocene low-angle detachments and upper crustal megaboudinage in the Monte Amiata geothermal area (Northern Apennines, Italy). *Geodin. Acta* 17, 375–387.
- Brogi, A., Caggianelli, A., Liotta, D., Zucchi, M., Spina, A., Capezzuoli, E., Casini, A., Buracchi, E., 2021. The Gavorrano Monzogranite (Northern Apennines): An Updated Review of Host Rock Protoliths, Thermal Metamorphism and Tectonic Setting. *Geosciences*, 11, 124. <https://doi.org/10.3390/geosciences11030124>
- Brogi, A., Capezzuoli, E., Liotta, D., Meccheri, M. 2015. The Tuscan Nappe structures in the Monte Amiata geothermal area (central Italy): a review. *Italian Journal of Geosciences*, Vo. 134/2, 219-236.
- Brogi, A., Giorgetti, G., 2012. Tectono-metamorphic evolution of the siliciclastic units in the Middle Tuscan Range (inner Northern Apennines): Mg-capholite bearing quartz veins related to syn-metamorphic syn-orogenic foliation. *Tectonophysics* 526–529, 167–184.
- Brogi, A., Lazzarotto, A., Liotta, D., Ranalli, G., 2005. Crustal structures in the geothermal areas of southern Tuscany (Italy): insights from the CROP 18 deep seismic reflection lines. *J. Volcanol. Geotherm. Res.* 148, 60–80.
- Brogi, A., Liotta, D., 2008. Highly extended terrains, lateral segmentation of the substratum, and basin development: the middle-late Miocene Radicondoli Basin (inner northern Apennines, Italy). *Tectonics* 27, 1–20.
- Brogi, A., Liotta, D., Meccheri, M., Fabbrini, L., 2010. Transtensional shear zones controlling volcanic eruptions: the Middle Pleistocene Monte Amiata volcano (inner Northern Apennines, Italy). *Terra Nova* 22, 137–146.
- Broothaers M., Bos, S., Lagrou D., Harcouët-Menou V., Laenen B., 2019. Lower Carboniferous limestone reservoir in northern Belgium: structural insights from the Balmatt project in Mol. Conference proceedings, European Geothermal Congress 2019, Den Haag, 11 – 14 June.
- Broothaers M., De Koninck R., Laenen B., Matthijs J. & Dirix K. (2020). Compilatie en duiding van warmtedata in de diepe ondergrond van Vlaanderen en opmaak van een warmtefluxkaart. 2020/RMA/R/2127 - Rapport in opdracht van de Vlaamse Overheid. Departement Omgeving.
- Broothaers M., Lagrou D., Laenen B., Harcouët-Menou V., Vos D., 2021. Deep geothermal energy in the Lower Carboniferous carbonates of the Campine Basin, northern Belgium: An overview from the 1950's to 2020. *Z. Dt. Ges. Geowiss. (J. Appl. Reg. Geol.)*, 172 (3), p. 211–225; <https://doi.org/10.1127/zdgg/2021/0285>
- Bruscoli, L., Fiaschi, D., Manfrida G., Tempesti, D., 2015 - Improving the Environmental Sustainability of Flash Geothermal Power Plants—A Case Study, *Sustainability*, 7, 15262-15283; doi:10.3390/su71115262
- Cadoux, A., Pinti, D.L., 2009. Hybrid character and pre-eruptive events of Monte Amiata volcano (Italy) inferred from geochronological, petro-geochemical and isotopic data. *J. Volc. Geoth. Res.* 179, 169–190.
- Calamai A., Castaldi R., Squarci, R., Taffi, L., 1970 - Geology, geophysics and hydrogeology of the Monte Amiata geothermal fields. I. Maps and comments. *Geothermics*, special issue, 1, 1-9
- Carmignani, L., Decandia, F.A., Disperati, L., Fantozzi, P.L., Lazzarotto, A., Liotta, D., Meccheri, M., 1994. Tertiary extensional tectonics in Tuscany (Northern Apennines, Italy). *Tectonophysics* 238, 295–315.
- Cavelier, C.; Pomerol, Ch. 1979. Chronologie et interprétation des événements tectoniques cénozoïques dans le bassin de Paris. In *Bulletin de la Société Géologique de France* 7 (21), pp. 33–48.
- Chinese, D., Orrù, P. F., Meneghetti, A., Cortella, G., Giordano, L., Benedetti, M., 2022 - Symbiotic and optimized energy supply for decarbonizing cheese production: An Italian case study. *Energy*, 257. <https://doi.org/10.1016/j.energy.2022.124785>
- Clauer, Ch., Ernst Huenges, E., 1995. Thermal Conductivity of Rocks and Minerals. In *Rock Physics & Phase Relations: A Handbook of Physical Constants*, Volume 3, edited by Thomas J. Ahrens, pp. 105-126 First published: 01 January 1995.
- Curnelle, R., Dubois, P. 1986. Evolution des grands bassins sédimentaires français : bassins de Paris, d'Aquitaine et du Sud-Est. In *Bulletin de la Société Géologique de France* 8, pp. 526–546.

D.M. 26.6.2009, n. 158, "Linee guida nazionali per la certificazione energetica degli edifici." (Italian)

Della Vedova, B., Vecellio, C., Bellani, S., Tinivella, U., 2008. Thermal modelling of the Larderello geothermal field (Tuscany, Italy). *Int J Earth Sci (Geol Rundsch)* 97, 317–332. <https://doi.org/10.1007/s00531-007-0249-0>

Derer CE, Schumacher ME, Schäfer A. The northern Upper Rhine Graben: basin geometry and early syn-rift tectono-sedimentary evolution. *Int J Earth Sci (geol Rundsch)*. 2005;94(4):640–56. <https://doi.org/10.1007/s00531-005-0515-y>.

Di Stefano, R., Bianchi, I., Ciaccio, M.G., Carrara, G., Kissling, E., 2011. Three-dimensional Moho topography in Italy: New constraints from receiver functions and controlled source seismology. *Geochem Geophys Geosystems* 12, n/a-n/a. <https://doi.org/10.1029/2011gc003649>

Dini, A., Gianelli, G., Puxeddu, M., Ruggieri, G., 2005. Origin and evolution of Pliocene–Pleistocene granites from the Larderello geothermal field (Tuscan Magmatic Province, Italy). *Lithos* 81, 1–31.

Dini, A., Westerman, D.S., Innocenti, F., Rocchi, S., 2008. Magma Emplacement in a Transfer Zone: the Miocene Mafic Orano Dyke Swarm of Elba Island 302. *Geological Society London Special Publications*, Tuscany, Italy, pp. 131–148.

Dörr W, Stein E. Precambrian basement in the Rheic suture zone of the Central European Variscides (Odenwald). *Int J Earth Sci (geol Rundsch)*. 2019;108(6):1937–57. <https://doi.org/10.1007/s00531-019-01741-7>.

Elter, P., Giglia, G., Tongiorgi, M., Trevisan, L., 1975. Tensional and compressional areas in the recent (Tortonian to Present) evolution on northern Apennines. *Boll. Geofis. Teor. Appl.* 65, 3–18.

Fahlbusch K. Die geologischen Grundlagen der alten Wasserversorgung Darmstadts. *Notizblatt Des Hessischen Landesamts Für Bodenforschung*. 1980;108:223–40.

Fahlbusch K. Störungszonen an den Rheingraben-Schultern (Hardt, Darmstadt) mit Hinweisen auf junge Bewegungen. *Notizblatt Des Hessischen Landesamts Für Bodenforschung*. 1975;103:315–26.

Filippucci, M., Tallarico, A., Dragoni, M., Lorenzo, S. de, 2019. Relationship Between Depth of Seismicity and Heat Flow: The Case of the Gargano Area (Italy). *Pure Appl. Geophys.* 176, 2383–2394.

Formhals, J., Feike, F., Hemmatabady, H., Welsch, B. and Sass, I., 2021. Strategies for a transition towards a solar district heating grid with integrated seasonal geothermal energy storage. *Energy*, 228, p.120662.

Garzonio, C.A., Affuso, A.M.G., 2004. Hydrogeological problems for the rehabilitation and re-utilisation of the water resources of the mining area of Gavorrano (Italy). *Geo* 46, 286–294. <https://doi.org/10.1007/s00254-004-0976-5>

Gely, J. P. 1996. Le Lutétien du Bassin parisien : de l'analyse séquentielle haute-résolution à la reconstitution paléogéographique. In *Bull. Inf. Géol. Bass. Paris* 34, pp. 3–27.

Ghanbarpour, M., Mota-Babiloni, A., Makhnatch, P., Badran, B. E., Rogstam, J., Khodabandeh, R. (2021). ANN modeling to analyze the R404A replacement with the low GWP alternative R449A in an indirect supermarket refrigeration system. *Applied Sciences* (Switzerland), 11(23). <https://doi.org/10.3390/app112311333>

Gola, G., Bertini, G., Bonini, M., Botteghi, S., Brogi, A., De Franco, R., Dini, A., Donato, A., Gianelli, G., Liotta, D., Manzella, A., Montanari, D., Montegrossi, G., Petracchini, L., Ruggieri, G., Santilano, A., Scrocca, D., Trumpy, E., 2017. Data integration and conceptual modelling of the Larderello geothermal area. *Italy. Energy Procedia* 125, 300–309.

Greifenhagen G. Untersuchungen zur Hydrogeologie des Stadtgebietes Darmstadt mit Hilfe eines Grundwasserinformationssystems unter Verwendung von einer Datenbank, Datenmodellierung und ausgewählten statistischen Methoden [Dissertation]. Darmstadt: Technische Universität Darmstadt; 2000.

Gruppo SOL.MAR. (2020). Connecting future - Report di Sostenibilità 2020. (Italian)

Guilhaumou, N. 1993. Paleotemperatures inferred from fluid inclusions in diagenetic cements: implications for the thermal history of the Paris basin. In *Eur. J. Mineral* 5, pp. 1217–1226.

Haeusler, L., Gié, G., Moreira, D., Badouard, T. and Crenes, M., 2020. Coût des énergies renouvelables et de recuperation en France, données 2019. ADEME, 100 p.

HLNUG. Geologische Übersichtskarte von Hessen 1:300000. Wiesbaden: Hessisches Landesamt für Naturschutz, Umwelt und Geologie; 2007.

Kempe S, Strassenburg J, Belzer S, Henschel H-V, Fahlbusch K. Der Darmstädter Granodiorit im Stollen in der der Dieburger Straße, Mathildenhöhe, Darmstadt. Jahresberichte Und Mitteilungen Des Oberrheinischen Geologischen Vereins. 2001;17:51–63.

Kinscher, J.L., Broothaers, M., Schmittbuhl, J., de Santis, F., Laenen, B., Klein, E., 2023. First insights to the seismic response of the fractured Carboniferous limestone reservoir at the Balmatt geothermal doublet (Belgium). *Geothermics* 107 102585, <https://doi.org/10.1016/j.geothermics.2022.102585>

Klemm G. Erläuterungen zur Geologischen Karte Blatt 6118 Darmstadt-Ost (ehem. Blatt Roßdorf). 3rd ed.; 1938.

Klemm G. Geologische Karte von Hessen 1:25000, Blatt 6118 Darmstadt Ost, 4. Auflage; 1911.

Kolokotroni, M., Mylona, Z., Evans, J., Foster, A., Liddiard, R. (2019). Supermarket energy use in the UK. *Energy Procedia*, 161, 325–332. <https://doi.org/10.1016/j.egypro.2019.02.108>

Kombrinck, H., 2008. The Carboniferous of the Netherlands and surrounding areas; a basin analysis. Dissertation, Geologica Ultraiectina (294), Utrecht University Repository, ISBN: 978-90-5744-160-8

Laenen, B., 2002. Lithostratigrafie van het pre-Tertiair in Vlaanderen Deel I: post-Dinantiaan. Studie uitgevoerd in opdracht van ANRE. VITO-rapport 2002/ETE/R/063, <https://publicaties.vlaanderen.be/view-file/2483>

Laenen, B., 2003. Lithostratigrafie van het pre-Tertiair in Vlaanderen II: Dinantiaan & Devoon. Studie uitgevoerd in opdracht van ANRE. VITO-rapport 2003/ETE/095, <https://publicaties.vlaanderen.be/view-file/24843>

Lang S, Hornung J, Krötschek M, Ruckwied K, Hoppe A. Tektonik und Sedimentation am Rand des Oberrheingrabens in Darmstadt im Mittel- und Oberpleistozän. *Geologisches Jahrbuch Hessen*. 2011;137:19–53.

Langenaeker, V.: The Campine Basin: stratigraphy, structural geology, coalification and hydrocarbon potential of the Devonian to Jurassic, *Aardkundige Mededelingen*, 10, (2000), 1-142.

Larsen, B., Grunnalite, I., Gudmundsson, A., 2010. How fracture systems affect permeability development in shallow-water carbonate rocks: An example from the Gargano Peninsula, Italy. *Journal of Structural Geology* 32, 1212–1230. <https://doi.org/10.1016/j.jsg.2009.05.009>

Liotta, D., 1991. The Arbia-Val Marecchia Line, Northern Apennines. *Eclogae Geol. Helv.* 84, 413–430.

Liotta, D., Brogi, A., 2020. Pliocene-Quaternary fault kinematics in the Larderello geothermal area (Italy): Insights for the interpretation of the present stress field. *Geothermics* 83, 101714. <https://doi.org/10.1016/j.geothermics.2019.101714>

Liotta, D., Ranalli, G., 1999. Correlation between seismic reflectivity and rheology in extended lithosphere: southern Tuscany, Inner Northern Apennines. Italy. *Tectonophysics* 315, 109–122.

Martini, I.P., Sagri, M., 1993. Tectono-sedimentary characteristics and the genesis of the recent magmatism of Southern Tuscany and Northern Latium. *Per. Mineral.* 56, 157–172.

Mezger JE, Felder M, Harms F-J. Crystalline rocks in the maar deposits of Messel: key to understand the geometries of the Messel Fault Zone and diatreme and the post-eruptional development of the basin fill. *zdgg*. 2013;164(4):639–62. <https://doi.org/10.1127/1860-1804/2013/0034>.

Minissale, A., 2004. Origin, transport and discharge of CO₂ in central Italy. *Earth-sci Rev* 66, 89–141. <https://doi.org/10.1016/j.earscirev.2003.09.001>

- Moeller, S., Grevenmeyer, I., Ranero, C.R., Berndt, C., Klaeschen, D., Sallares, V., Zitellini, N., Franco, R.D., 2013. Early-stage rifting of the northern Tyrrhenian Sea Basin: Results from a combined wide-angle and multichannel seismic study. *Geochem. Geophys. Geosyst.* 14, 3032–3052. <https://doi.org/10.1002/ggge.20180>
- Molli, G., 2008. Northern Apennine-Corsica orogenic system: An updated overview. In: Siegesmund, S., Fügenschuh, B., Froitzheim, N. (Eds.), *Tectonic Aspects of the Alpine-Dinaride-Carpathian System*. vol. 298. Geological Society, London, Special Publication, pp. 413–442.
- Oltmanns J. Analysis and Improvement of an existing university district energy system. Technical University of Darmstadt; 2021. <https://doi.org/10.26083/tuprints-00017367>.
- Pagliarulo, P., 1996. Migrazione di fluidi profondi nel substrato prepliocenico dell'avanfossa appenninica (bacino pugliese e lucano). *Mem.Soc.Geo.It.* 51, 659–668.
- Panorama de la chaleur renouvelable et de récupération – Edition 2019. CIBE, Fedene, SER, Uniclima, ADEME, 56.
- Patijn, R.J.H. and Kimpe, W.F.M.: De kaart van het Carboonoppervlak, de profielen en de kaart van het dekterrein van het zuid-Limburgse mijngebied en Staatsmijn Beatrix en omgeving, Mededelingen Geologische Stichting, 44, (1961), 5-12.
- Pauselli, C., Gola, G., Mancinelli, P., Trumpy, E., Saccone, M., Manzella, A., Ranalli, G., 2019. A new surface heat flow map of the Northern Apennines between latitudes 42.5 and 44.5 N. *Geothermics* 81, 39–52. <https://doi.org/10.1016/j.geothermics.2019.04.002>
- Pauwels, J., 2021. Chemical and radiological assessment of deep brine-type geothermal groundwaters. Dissertation presented in partial fulfilment of the requirements for the degree of Doctor of Science (PhD): Geology, KU Leuven.
- Pauwels, J., Salah, S., Vasile, M., Laenen, B., Cappuyns, V., 2021. Characterization of scaling material obtained from the geothermal power plant of the Balmatt site, Mol. *Geothermics*, (2021), 102090, 94.
- Perrodon, A.; Zabek, J., 1990. Paris Basin. In Morris W. Leighton (Ed.): *Interior cratonic basins*, vol. 51. Tulsa, Okla.: American Association of Petroleum Geologists (AAPG memoir, 51), pp. 633–679. Available online at <https://pubs.geoscienceworld.org/books/book/1351/chapter/107171714/Paris-Basin>, checked on 4/3/2020.
- Purser, B. H., 1975. *Sedimentation et diagenèse précoce des séries du Jurassique moyen de Bourgogne*. Univ. Paris sud Orsay.
- Robertson, E.C., 1988. Thermal Properties of Rocks. USGS Open-File Report 88-441.
- Robie, R.A., Hemingway, B.S., 1995. Thermodynamic Properties of Minerals and Related Substances at 298.15 K and 1 Bar (10^5 Pascals) Pressure and at Higher Temperatures. U.S. Geological Survey Bulletin 2131.
- Rochira, F., Caggianelli, A., de Lorenzo, S., 2018. Regional thermo-rheological field related to granite emplacement in the upper crust: implications for the Larderello area (Tuscany, Italy). *Geodin. Acta* 30, 225–240.
- Romagnoli, P., Arias, A., Barelli, A., Cei, M., Casini, M., 2010. An updated numerical model of the Larderello-Travale geothermal system. Italy. *Geothermics* 39, 292–313.
- Rossetti, F., Faccenna, C., Jolivet, L., Goffé, B., Funiciello, R., 2002. Structural signature and exhumation P-T-t paths of the blueschist units exposed in the interior of the North- ern Apennine chain, tectonic implications. *Boll. Soc. Geol. Ital.* 1, 829–842.
- Rybäck, L., 1988. Determination of heat production rate. In: Haenel, R., Rybach, L., Stegenga, L. (Eds.), *Handbook of Terrestrial Heat-flow Density Determination*. Kluwer Academic Press, pp. 125–142.
- Sass, J. H., Lachenbruch, A.H, and Moses, T.H. Jr., 1992. Heat flow from a scientific research well at Cajon Pass, California. *J. Geophys. Res.*, 97(B4), 5017–5030, 1992.

- Schumacher ME. Upper Rhine Graben: Role of preexisting structures during rift evolution. *Tectonics*. 2002;21(1):6–17. <https://doi.org/10.1029/2001TC900022>.
- Seib, L., Welsch, B., Bossennec, C., Frey, M. and Sass, I., 2022. Finite element simulation of permeable fault influence on a medium deep borehole thermal energy storage system. *Geothermal Energy*, 10(1), pp.1-21.
- Serri, G., Innocenti, F., Manetti, P., 1993. Geochemical and petrological evidence of the subduction of delaminated Adriatic continental lithosphere in the genesis of the Neogene–Quaternary magmatism of central Italy. *Tectonophysics* 223, 117–147.
- Spiess, R., Langone, A., Caggianelli, A., Stuart, F.M., Zucchi, M., Bianco, C., Brogi, A., Liotta, D., 2021. Unveiling ductile deformation during fast exhumation of a granitic pluton in a transfer zone. *J Struct Geol* 147, 104326. <https://doi.org/10.1016/j.jsg.2021.104326>
- Stein E. The geology of the Odenwald Crystalline Complex. *Mineral Petrol.* 2001;72:7–28. <https://doi.org/10.1007/s007100170024>.
- Stober I, Bucher K. Hydraulic properties of the crystalline basement. *Hydrogeol J.* 2007;15(2):213–24. <https://doi.org/10.1007/s10040-006-0094-4>.
- Torelli, M., Traby, R., Teles, V. and Ducros, M., 2020. Thermal evolution of the intracratonic Paris Basin: Insights from 3D basin modelling. *Marine and Petroleum Geology*, 119, 1004487.
- Tripaldi, S. 2020. Electrical signatures of a permeable zone in carbonates hosting local geothermal manifestations: insights for the deep fluid flow in the Gargano area (south-eastern Italy). *Bollettino di Geofisica Teorica ed Applicata*. <https://doi.org/10.4430/bgta0312>
- Ungar, P., Milli, L., Manfrida, G., Fiaschi, D., Talluri, L. (2022). Re-designing district heating networks through innovative CO₂ solutions. *Journal of Physics: Conference Series*, 2385(1), 012125. <https://doi.org/10.1088/1742-6596/2385/1/012125>
- van der Voet E., Laenen B., Rombaut B., Kourta M., Swennen R., 2020. Fracture characteristics of Lower Carboniferous carbonates in northern Belgium based on FMI log analyses. *Netherlands Journal of Geosciences*, Volume 99, 2020 e8. <https://doi.org/10.1017/njg.2020.6>
- van der Voet, E., 2021. Fracture properties within a Lower Carboniferous carbonate geothermal reservoir in the Campine-Brabant Basin. A study based on boreholes (northern Belgium) and outcrop analogues (southern Belgium). Dissertation presented in partial fulfilment of the requirements for the degree of Doctor of Science (PhD): Geology, KU Leuven.
- Vandenberghé, N., Dusar, M., Boonen, P., Fan, L.S., Voets, R., Bouckaert, J. 2000. The Merksplas-Beerse geothermal well (17W265) and the Dinantian reservoir. *Geologica Belgica*, 3/3-4. 349 – 367.
- Vasile, M., Bruggeman, M., Van Meensel, S., Bos, S., Laenen, B., 2017. Applied Radiation and Isotopes, (2017), 126 Characterization of the natural radioactivity of the first deep geothermal doublet in Flanders, Belgium. Characterization of the natural radioactivity of the first deep geothermal doublet in Flanders, Belgium. *Applied Radiation and Isotopes*, (2017), 300-303, 126.
- Wassing, B., Broothaers, M., Candela, T., Cremer, H., ter Heege, J., Laenen, B., Pogacnik, J., Soustelle, V., Tsopela, A., 2022. Seismicity Potential Dinantian geothermal reservoirs – implications of case study Balmatt for projects in the Netherlands – SeiMoD. TKI Project SeiMoD (TKI2021-02-GE). Public results report | August 23, 2022
- Weinert S, Bär K, Sass I. Petrophysical Properties of the Mid-German Crystalline High: A Database 1 for Bavarian, Hessian, Rhineland-Palatinate and Thuringian Outcrops. Institut für Angewandte Geowissenschaften, Darmstadt; 2020.
- Zoth, G., and Hfinel, R., 1988. Appendix, in *Handbook of Terrestrial Heat Flow Density Determination*, edited by R. Hänel, L. Rybach and L. Stegenga, pp 449-446, Kluwer, Dordrecht.

Annex 1: Case study: Template

General description of the pilot site

Geological conditions

Used data

- Give an overview of the observations (e.g., offset well, seismic campaigns, MT and gravimetric surveys, surface manifestations), data sets and geological models that are used for the evaluation.

Geological setting

- Describe the geological conditions that are relevant for the project, covering:
 - Regional setting
 - The local structural setting
 - The lithostratigraphic framework

Description of the geothermal target

- Describe the target formation for the HOCLOOP system. Provide information about essential thermal and mechanical properties (see list below). Evaluate the uncertainty and identify knowledge gaps.
 - Depth and thickness
 - Lithology
 - Thermal properties (e.g., heat capacity, thermal conductivity, heat generation)
 - Mechanical properties (e.g., density, Poisson's ratio, strength)
 - Flow properties (e.g., porosity, permeability)
 - Formation fluid (e.g., composition, specific heat capacity)
 - Temperature model

Knowledge gaps

- Summarize gaps in available data/knowledge about the geothermal target
- Describe the work program to fill in crucial knowledge gaps and to (further) explore the geothermal potential

Past/Current/future above ground energy system

- Provide a simplified schematic of the geothermal installation
- General overview of the future plans (excl HOCLOOP concept)
- Describe foreseen future plans for the existing or under development plant will be described in the section, including surface and subsurface changes of the current installation
- Describe plant restrictions and operational conditions

Description and Schematic overview on different integration options of the HOCLOOP concept

- Propose different integration options for the HOCLOOP solution
- Also include the pros and cons of each of the potential options

Technical challenges

- Describe the geological risks that are associated with the development and exploitation of the geothermal potential and define mitigation measures. A bow-tie analysis can be used for a project specific risk assessment and to define mitigating measures¹.
- Describe the current technical challenges such as:
 - Seismicity
 - Scaling...

Economic aspects

- Current and future heat prices
- ...

Summary table

Parameter	Value	Unit
Geological information		
Top reservoir Depth		m
Thickness of the reservoir		m
Temperature at the top of the reservoir		°C
Type of reservoir (homogeneous, fractured/fissured)		
If fractured, fracture distribution type		
Hydraulic properties		
Permeability of the reservoir		m ²
Matrix porosity		%
Regional flow		
Thermal properties		
Thermal conductivity (in reservoir)		m
Thermal conductivity(ies) above		m
Geothermal gradient(s) up to the top reservoir		°C/km
Thermal Capacity (reservoir rock)		
Geothermal loop		
Extraction well depth		m
Injection well depth		m
[Add additional wells if needed]		
Brine extraction temperature*		°C
Brine extraction flow		m ³ /h
Brine reinjection temperature		°C
Brine reinjection max temperature		°C
Hot water loop		

¹ The bowtie method - CGE Barrier Based Risk Management Knowledge base (cgerisk.com)

Supply collector water temperature		°C
Return collector water temperature		°C
Supply and return collectors pipe size		-
Heat transportation network		
Supply temperature*		°C
return temperature*		°C
distribution pump flow rate		m ³ /h
distribution pump delivery pressure		barg
distribution pump discharge head		m
distribution pump NSPHa		m
pipe length to VITO boiler house		km
pipe diameter to VITO boiler house		-
Boiler house		
Gas boiler capacity*		MW _{th}
Gas boiler quantity		-
HTR/DHG heat exchanger capacity*		MW _{th}
HTR/DHG heat exchanger quantity		-
Emergency cooler		
Cold side inlet temperature*		°C
Cold side outlet temperature*		°C
Hot side inlet temperature		°C
Hot side outlet temperature *		°C
Maximum cooling power*		MW _{th}